

AD-A232 758

DUPLICATE FILE COPY

①

REPORT DOCUMENTATION PAGE			FORM 298 (Rev. 2-89)	
<small>1. REPORT NUMBER, 2. AUTHOR, 3. TITLE, 4. SUBTITLE, 5. FUNDING NUMBERS, 6. PERFORMING ORGANIZATION NAME(S) AND ADDRESS(ES), 7. PERFORMING ORGANIZATION REPORT NUMBER, 8. SPONSORING/MONITORING AGENCY NAME(S) AND ADDRESS(ES), 9. SPONSORING/MONITORING AGENCY REPORT NUMBER, 10. SUPPLEMENTARY NOTES, 11. DISTRIBUTION AVAILABILITY STATEMENT, 12. DISTRIBUTION CODE, 13. ABSTRACT (Maximum 200 words), 14. SUBJECT TERMS, 15. NUMBER OF PAGES, 16. PRICE CODE, 17. SECURITY CLASSIFICATION OF REPORT, 18. SECURITY CLASSIFICATION OF THIS PAGE, 19. SECURITY CLASSIFICATION OF ABSTRACT, 20. LIMITATION OF ABSTRACT</small>				
1. AGENCY USE ONLY (leave blank)		2. REPORT DATE	3. REPORT TYPE AND DATES COVERED	
		1990	THESIS/DISSERTATION	
4. TITLE AND SUBTITLE Linear Stability of Wavy Baroclinic Flow Over Topography			5. FUNDING NUMBERS	
6. AUTHOR(S) Thomas F. Simeone				
7. PERFORMING ORGANIZATION NAME(S) AND ADDRESS(ES) AFIT Student Attending: Florida State University			8. PERFORMING ORGANIZATION REPORT NUMBER AFIT/CI/CIA- 90-144	
9. SPONSORING/MONITORING AGENCY NAME(S) AND ADDRESS(ES) AFIT/CI Wright-Patterson AFB OH 45433-6583			10. SPONSORING/MONITORING AGENCY REPORT NUMBER	
11. SUPPLEMENTARY NOTES				
12a. DISTRIBUTION AVAILABILITY STATEMENT Approved for Public Release IAW 190-1 Distributed Unlimited ERNEST A. HAYGOOD, 1st Lt, USAF Executive Officer			12b. DISTRIBUTION CODE	
13. ABSTRACT (Maximum 200 words)				
DTIC ELECTE FEB 07 1991 S B D				
14. SUBJECT TERMS			15. NUMBER OF PAGES 115	
			16. PRICE CODE	
17. SECURITY CLASSIFICATION OF REPORT		18. SECURITY CLASSIFICATION OF THIS PAGE	19. SECURITY CLASSIFICATION OF ABSTRACT	20. LIMITATION OF ABSTRACT

GENERAL INSTRUCTIONS FOR COMPLETING SF 298

The Report Documentation Page (RDP) is used in announcing and cataloging reports. It is important that this information be consistent with the rest of the report, particularly the cover and title page. Instructions for filling in each block of the form follow. It is important to **stay within the lines to meet optical scanning requirements.**

Block 1. Agency Use Only (Leave Blank)

Block 2. Report Date. Full publication date including day, month, and year, if available (e.g. 1 Jan 88). Must cite at least the year.

Block 3. Type of Report and Dates Covered. State whether report is interim, final, etc. If applicable, enter inclusive report dates (e.g. 10 Jun 87 - 30 Jun 88).

Block 4. Title and Subtitle. A title is taken from the part of the report that provides the most meaningful and complete information. When a report is prepared in more than one volume, repeat the primary title, add volume number, and include subtitle for the specific volume. On classified documents enter the title classification in parentheses.

Block 5. Funding Numbers. To include contract and grant numbers; may include program element number(s), project number(s), task number(s), and work unit number(s). Use the following labels:

C - Contract	PR - Project
G - Grant	TA - Task
PE - Program Element	WU - Work Unit Accession No.

Block 6. Author(s). Name(s) of person(s) responsible for writing the report, performing the research, or credited with the content of the report. If editor or compiler, this should follow the name(s).

Block 7. Performing Organization Name(s) and Address(es). Self-explanatory.

Block 8. Performing Organization Report Number. Enter the unique alphanumeric report number(s) assigned by the organization performing the report.

Block 9. Sponsoring/Monitoring Agency Name(s) and Address(es). Self-explanatory.

Block 10. Sponsoring/Monitoring Agency Report Number. (If known)

Block 11. Supplementary Notes. Enter information not included elsewhere such as: Prepared in cooperation with...; Trans. of ..., To be published in When a report is revised, include a statement whether the new report supersedes or supplements the older report.

Block 12a. Distribution/Availability Statement.

Denote public availability or limitation. Cite any availability to the public. Enter additional limitations or special markings in all capitals (e.g. NOFORN, REL, ITAR)

DOD - See DoDD 5230.24, "Distribution Statements on Technical Documents."

DOE - See authorities

NASA - See Handbook NHB 2200.2.

NTIS - Leave blank.

Block 12b. Distribution Code.

DOD - DOD - Leave blank

DOE - DOE - Enter DOE distribution categories from the Standard Distribution for Unclassified Scientific and Technical Reports

NASA - NASA - Leave blank

NTIS - NTIS - Leave blank.

Block 13. Abstract. Include a brief (Maximum 200 words) factual summary of the most significant information contained in the report.

Block 14. Subject Terms. Keywords or phrases identifying major subjects in the report.

Block 15. Number of Pages. Enter the total number of pages.

Block 16. Price Code. Enter appropriate price code (NTIS only).

Blocks 17. - 19. Security Classifications. Self-explanatory. Enter U.S. Security Classification in accordance with U.S. Security Regulations (i.e., UNCLASSIFIED). If form contains classified information, stamp classification on the top and bottom of the page.

Block 20. Limitation of Abstract. This block must be completed to assign a limitation to the abstract. Enter either UL (unlimited) or SAR (same as report). An entry in this block is necessary if the abstract is to be limited. If blank, the abstract is assumed to be unlimited.

1991

THE FLORIDA STATE UNIVERSITY
COLLEGE OF ARTS AND SCIENCES

**LINEAR STABILITY OF WAVY,
BAROCLINIC FLOW OVER TOPOGRAPHY**

By

THOMAS F. SIMEONE

A Thesis submitted to the
Department of Meteorology
in partial fulfillment of the requirements
for the degree of Master of Science

Degree Awarded:
Fall Semester, 1990

91 2 06 108

The members of the Committee approve the thesis of Thomas F. Simeone defended
on 15 November 1990.

Albert I. Barcion

Albert I. Barcion
Professor Directing Thesis

Richard L. Pfeffer

Richard L. Pfeffer
Committee Member

Steven A. Stage

Steven A. Stage
Committee Member

Paul H. Ruscher

Paul H. Ruscher
Committee Member

Accession For		
NTIS GRA&I	<input checked="checked" type="checkbox"/>	
DTIC TAB	<input type="checkbox"/>	
Unannounced	<input type="checkbox"/>	
Justification		
By		
Distribution/		
Availability Codes		
Dist	Avail and/or Special	
A-1		

ACKNOWLEDGEMENTS

I would like to express my extreme gratitude to my major professor, Dr. Albert I. Barcion, who spent countless hours working with me on this problem. Without his help and motivation, I would not have completed such a thorough thesis. I would also like to thank Dr. Richard L. Pfeffer for his discussions and inputs to this work. I would like to express my gratitude to Dr. Jeffrey Whitaker for all of his help on the computer. Also, I would like to thank the members of my committee, Drs. Steven A. Stage and Paul H. Ruscher, for their comments as well as the members of GFDI for their inputs to this work. Finally, I would like to thank the United States Air Force for giving me the opportunity to earn my master's degree and the members of AFIT/CIR for their support on this work.

TABLE OF CONTENTS

ACKNOWLEDGEMENTS	iii
LIST OF FIGURES	vi
LIST OF SYMBOLS	x
ABSTRACT	xiii
CHAPTER 1. INTRODUCTION	1
CHAPTER 2. ATMOSPHERIC AND ANNULUS OBSERVATIONS	6
2.1 Atmospheric Observations	6
2.1.1 Geographical Distribution of Low Frequency Variability	6
2.1.2 High Frequency Variability	9
2.1.3 Climatology of Northern Hemisphere Wintertime Stationary Waves	15
2.2 Annulus Observations	17
CHAPTER 3. MODEL FORMULATION	21
3.1 Governing Equations	21
3.2 Transformation of Equations To Sigma Coordinates	24
3.3 Scaling	27
3.4 Quasi-Geostrophic Model	36
3.5 Linearized Quasi-Geostrophic Model	38
3.6 Wavy Basic State	40
3.7 Topographic Instability and Form Drag	45
CHAPTER 4. ANALYTICAL AND NUMERICAL SOLUTIONS	49

4.1 Eady Model	50
4.2 Analytical Solutions and Results	54
4.2.1 Problem Formulation	55
4.2.2 Asymptotic Expansion In Orders of v	56
4.3 Numerical Solution	62
4.4 Topographic Instability	82
CHAPTER 5. DISCUSSION AND CONCLUSIONS	86
APPENDIX A. SCALING OF CURVATURE TERMS AND THE BETA EFFECT	92
A.1 Curvature Terms	94
A.2 Beta Effect	
APPENDIX B. COEFFICIENTS FOR THE NUMERICAL SOLUTION AND TOPOGRAPHIC INSTABILITY PROBLEM	96
B.1 Numerical Solution	96
B.2 Coefficients For Topographic Instability	97
REFERENCES	99
BIOGRAPHICAL SKETCH	102

LIST OF FIGURES

- Figure 2.1** Map of low pass filtered rms geopotential at 500 mb for nine winters. Emphasizes fluctuations in periods longer than 10 days. The contribution from the mean annual cycle has been removed. Contour interval is 10 m. From Blackmon (1976). 8
- Figure 2.2** Climatological mean 500 mb height field for winter. Contour interval is 50 m. From Blackmon (1976). 8
- Figure 2.3** Composite geopotential height patterns for 24-day period beginning 31 December 1980, based upon daily analyses made at ECMWF. (a) 500 mb height, contour interval is 60 m and (b) 1000 mb height, contour interval 30 m. From Blackmon, Lee, and Wallace (1984). 10
- Figure 2.4** Composite geopotential height patterns for the 22 days 1-9 and 18-24 December 1980 and 5-10 February 1981, inclusive. Based on daily analyses made at ECMWF. From Blackmon, Lee, and Wallace (1984). 10
- Figure 2.5** Climatology of the 850 and 500 mb levels for the area of the Rocky Mountains. (a) 850 mb mean geopotential height and (b) standard deviation of the high pass filtered geopotential height divided by the sine of the latitude. (c) 500 mb mean geopotential and (d) is the standard deviation. From Buzzi and Tosi (1989). 13
- Figure 2.6** Maps of lagged correlation coefficients between the high-pass filtered 850mb level at 54°N , 129°W and the high pass filtered 850 mb level at every other grid point. The black dot show this location. Each plot shows this location. Each plot shows a different lag time. (a) -24 hr, (b) -12 hr, (c) zero lag, (d) +12 hr, (e) +24 hr, (f) +36 hr. Contour interval is 0.05 and negative values are dashed. From Buzzi and Tosi (1989). 14
- Figure 2.7** Correlation values between high-pass filtered 850 mb level and high pass filtered 500 mb level at every grid point. Area includes the Rocky Mountains. From Buzzi and Tosi (1989). 14
- Figure 2.8** Longitude-height cross sections of departure from zonal symmetry of the time-averaged geopotential height taken along (a) 60°N , (b) 45°N , and (c) 25°N latitude circle. Contour interval is 50 m. The local orography is depicted at the bottom of the figure. From Lau (1979). 16
- Figure 2.9** Zonal wavenumber spectra of ψ at mid-radius for seven different rotation rates. (a) Time averages of the sequence of individual spectra of ψ and (b) spectra of the time-averaged (or climatological) ψ

field representing the standing waves. From Pfeffer *et al.* (1989). 18

Figure 2.10 Velocity data based on measurements taken at a depth of 5.7 cm in seven experiments at different rotation rates. (a) Time- and zonally -averaged velocity profile (U). Here, y is the distance from the outer toward the inner wall and Y is the gap width of the annulus. (b) Time-averaged streamfunction, ψ . Contour interval is $0.1 \text{ cm}^2 \text{ s}^{-1}$. (c) Time-averaged wavenumber 2 component of the stream function, determined by Fourier analyses of ψ . Units of U are cm s^{-1} . Contour interval is $0.02 \text{ cm}^2 \text{ s}^{-1}$. Arrows indicate locations of topographic ridges. From Pfeffer *et al.* (1989). 20

Figure 3.1 Cross section showing the relationship between the σ -coordinate and the z -coordinate. The shaded region indicates the topography. The surface $\sigma = 0$ is coincident with the topography. The surface $z = 0$ is at the mid-depth of the mountain. D is the average fluid depth. 25

Figure 3.2 (a) Top view of the annulus where b is the outer radius and a is the inner radius, and (b) side view of the annulus dimensions where D is measured from the surface $z = 0$. 33

Figure 3.3 Basic state streamfunction where (a) is an x - y cross section at the top, (b) is an x - y cross section at the bottom, (c) is an x - σ cross at mid-radius, and (d) is an x - σ cross section of the wavy part of the basic state at mid-radius. Mountain ridges are at 0 and π rad. $S = 0.25$, $U_0 = 0.1$, $\delta = 0.1$, and $\lambda = 1$. 44

Figure 3.4 (a) Magnitude of the basic state coefficient A_B and (b) magnitude of the basic state coefficient B_B as a function of U_0 . $\lambda = 1$, and $S = 0.25$. 46

Figure 4.1 (a) Growth rate as a function of wavenumber for the Eady model. S ranges from 0.1 - 0.4 . $S = 0.25$ is labeled. (b) Frequency for the positive root in (4.1.10) and (c) for the negative root in (4.1.10) as a function of wavenumber for the same range of S . Arrows indicate the direction of increasing stratification. 53

Figure 4.2 Plot of (4.2.16) where (a) is the real and (b) is the imaginary contribution to the term G^T , (c) is the real and (d) is the imaginary contribution to G^T from $F_B(\partial F_B/\partial \sigma)$, and (e) is the real and (f) is the imaginary contribution to G^T from $F_O(\partial F_B/\partial \sigma)$ as a function of wavenumber. The solid line is for $U_0 = -0.5$, long dashed is for $U_0 = 0.1$, and the short dashed is for $U_0 = 0.5$. 58

Figure 4.3 Plot of (4.2.17) where (a) is the real and (b) is the imaginary contribution to the term G^B , (c) is the real and (d) is the imaginary contribution to G^B from $F_B(\partial F_B/\partial \sigma)$, (e) is the real and (f) is the imaginary contribution to G^B from $F_O(\partial F_B/\partial \sigma)$, and (g) is the real and (h) is the imaginary contribution to G^B from F_O as a function of wavenumber.

The solid line is for $U_0 = -0.5$, long dashed is for $U_0 = 0.1$, and the short dashed is for $U_0 = 0.1$. 59

Figure 4.4 The magnitude of the coefficients in (4.2.14) and (4.2.18) for (a) the lower and (b) the upper boundary for the case of $n = 6$, $n + 2 = 8$, and $n - 2 = 4$. Here, $U_0 = 0.1$, $\epsilon = 0.1$, and $\lambda = 1.0$. 63

Figure 4.5 $X-\sigma$ cross sections at mid-radius for the perturbation streamfunction for (a) the sum of the most unstable mode from the Eady model, wavenumber 6, plus corrections due to topography from wavenumbers 4 and 8. (b) Most unstable Eady mode, wavenumber six, (c) wavenumber 8, and (d) wavenumber 4. $S = 0.25$, $U_0 = 0.0$, and $\lambda = 1.0$. Topographic ridges at 0.0 and π rad. 64

Figure 4.6 Contours of (a) growth rate and (b) frequency for the most unstable mode as a function of stratification, S , and mountain height, δ . Arrows indicate the direction of increasing values of growth rate or frequency. $U_0 = 0.1$, $\lambda = 1.0$, and $\epsilon = 0.1$. 70

Figure 4.7 Contours of (a) growth rate and (b) frequency for the most unstable mode as a function of S and U_0 . Arrow indicates the direction of increasing values. $\delta = 0.1$, $\lambda = 1.0$, and $\epsilon = 0.1$. 72

Figure 4.8 Basic state and perturbation streamfunction for very small mountain height, $h = 0.01$. (a) $x-y$ cross section of basic state streamfunction at top and (b) bottom. (c) $x-\sigma$ cross section of basic state streamfunction at mid-radius and (d) wavy part of basic state streamfunction. (e) $x-y$ cross section of perturbation streamfunction at top and (b) bottom. (g) $x-\sigma$ cross section perturbation at mid-radius. Topographic ridge at 0.0 and π rad. $U_0 = 0.1$, $\lambda = 1.0$, and $\epsilon = 0.1$. 73

Figure 4.9 Perturbation streamfunction for a mountain height, $h = 0.1$. (a) $x-y$ cross section at top and (b) bottom. (c) $x-\sigma$ cross section at mid-radius. Topographic ridge at 0.0 and π rad. $S = 0.25$, $U_0 = 0.1$, $\epsilon = 0.1$, and $\lambda = 1.0$. 76

Figure 4.10 Magnitude of the coefficients of (4.3.2) as a function of wavenumber for (a) the lower and (b) the upper boundary. Here, $S = 0.25$, $U_0 = 0.1$, $\delta = 0.1$, $\epsilon = 0.1$, and $\lambda = 1.0$. 77

Figure 4.11 Perturbation streamfunction when the basic flow is zero so that there is no wavy basic state but the mountain height is $\delta = 0.1$. (a) $x-y$ cross section at top and (b) bottom. (c) $x-\sigma$ cross section at mid-radius. Topographic ridge at 0.0 and π rad. $S = 0.25$, $U_0 = 0.0$, $\epsilon = 0.1$, and $\lambda = 1.0$. 79

Figure 4.12 Perturbation streamfunction as a function of non-dimensional time with no wavy basic state. (a) - (d) $x-\sigma$ cross sections and (e) - (f) $x-y$ cross sections. Topographic ridge at 0.0 and π rad. $S = 0.25$, $U_0 = 0.0$, $\epsilon = 0.1$, and $\lambda = 1.0$. 81

Figure 4.13 Contours of (a) growth rate and (b) frequency for the

topographic instability problem as a function of S and U_0 . Region of zero frequency is in the lower right hand corner. $\delta = 0.1$, $\lambda = 1.0$ and $\epsilon = 0.1$. 84

Figure 4.14 Contours of (a) growth rate and (b) frequency for the topographic instability problem as a function of S and h . Region of zero frequency is for low values of S . $U_0 = 0.1$, $\lambda = 1.0$ and $\epsilon = 0.1$. 85

LIST OF SYMBOLS

α	Coefficient of volumetric expansion
A_B, B_B	Amplitudes for basic state $F_B(\sigma)$
A_n, B_n	Arbitrary complex amplitude coefficients
β_0	Beta effect
D	Average depth of fluid
$\delta = h/D$	Non-dimensional mountain height
$\epsilon = U/fL$	Rossby number
f, f_0	Coriolis parameter - constant
$h(x)$	Mountain height
$g(z)$	Gravity
K	Fundamental non-dimensional zonal wavenumber
L	Horizontal length scale
l	Fundamental non-dimensional meridional wavenumber
λ	Non-dimensional vertical shear
Λ	Dimensional wavelength
$\eta(x)$	Non-dimensional mountain
N	Brunt Väissälä frequency - constant
n, q	zonal wave number
m, r	meridional wavenumber
$v = S\delta/\epsilon$	

Ω	Rotation rate
ω	Frequency
$p(x,y,z,t)$	Pressure
$p_s(z)$	Static pressure
$p'(x,y,z,t)$	Perturbation pressure
$\Pi(x,y,\sigma)$	Basic state potential vorticity
$\Pi_B(x,y,\sigma)$	Wavy basic state potential vorticity
$\phi(x,\sigma)$	X-dependent part of wavy basic state
$\psi(x,y,\sigma,t)$	Streamfunction
$\Psi(x,y,\sigma,t)$	Basic state streamfunction
$\phi(x,y,\sigma,t)$	Perturbation streamfunction
$Q(x,y,\sigma,t)$	Potential vorticity
$q(x,y,\sigma,t)$	Perturbation potential vorticity
$q_B(x,y,\sigma)$	Basic state potential vorticity
ρ_0	Constant density
r_0	Earth's radius
$S = (ND/fL)^2$	Burger number
σ	Vertical coordinate
$T(x,y,z,t)$	Temperature
T_0	Reference temperature
$T_s(z)$	Static temperature
$T'(x,y,z,t)$	Perturbation temperature
ΔT_H	Scale for horizontal temperature perturbation
ΔT_V	Scale for vertical temperature
\vec{V}	Velocity vector, (u,v)

$u, v(x, y, z, t)$	Zonal and meridional components of velocity
U	Scale for zonal velocity
$\bar{U}(y, \sigma)$	Mean part of basic state, Eady
U_0	Constant zonal velocity
$U^{T, B}$	Zonal velocity at the top and bottom
$w(x, y, z, t)$	Vertical velocity
x, y, z	Distance in Cartesian coordinate
ζ	Relative vorticity

LINEAR STABILITY OF WAVY, BAROCLINIC FLOW OVER TOPOGRAPHY

Thomas F. Simeone, Master of Science
Florida State University, 1990
Albert I. Barcilon, Ph. D

It is observed that topography plays an important role in forcing planetary scale stationary waves as well as influencing synoptic scale disturbances. The purpose of this study is to investigate topographic influences on planetary and synoptic scale waves in a baroclinic fluid using the quasi-geostrophic potential vorticity equation with wavenumber two bottom topography and a steady, wavy basic state on an f -plane.

The steady basic state is sinusoidal in x with linear vertical shear and represents an exact solution to the quasi-geostrophic potential vorticity equation and thermodynamic equations at the upper and lower boundaries. The amplitude of the wavy basic is highly dependent on forcing by a constant zonal flow, U_0 . U_0 is a parameter used to represent momentum flux convergence into the mid-latitudes.

The results from a linear analytical solution show that any mode with wavenumber n which interacts with the two-wave topography will introduce two additional modes, $n \pm 2$. All three modes will have the same frequency. The results of a linear stability analysis from a numerical model show that the growth rate for the most unstable mode is not highly dependent on the mountain height or zonal flow, U_0 . When there is a wavy basic state forced by U_0 , the perturbations are forced to follow the basic state. When U_0 is zero, there is no wavy basic state; however, the perturbations still are forced to *wave* over the mountain.

CHAPTER 1

INTRODUCTION

During the past decade, there has been considerable research into the role of topography on planetary and synoptic scale flow. The research has been observational, experimental and theoretical. In this thesis, we review some observational and experimental research and present a simple theoretical model of baroclinic flow over topography. We look to the observational evidence for guidance in developing the theoretical model. Wavenumber two dominates the nearly stationary pattern in the atmosphere and the annulus. So, we chose a steady wavy basic state forced by wavenumber two topography. On the smaller scale, baroclinic disturbances tend to follow the storm tracks as the flow over the Rocky Mountains. Therefore, we did a linear stability analysis of the wavenumber two basic state to investigate the relationship between disturbances and the basic state.

Blackmon (1976), Blackmon *et al.* (1977), Blackmon *et al.* (1979), and Wallace (1983), Blackmon *et al.* (1984), and Grose and Hoskins (1979) studied the Northern Hemisphere circulation and focused on traveling waves of various spatial and temporal scales. From their studies of the 500 mb geopotential height field, they found wavenumber two dominates and is nearly stationary with high pressure ridges over the major mountain chains. Lau (1979), Held (1983), and Wallace (1983) studied the climatology of the Northern Hemisphere. Again, the vertical and horizontal cross sections for the winter months showed high pressure ridges over the major terrain features with wavenumber two

dominating. Grose and Hoskins (1979) showed that wavenumber two dominates the Earth's topographic features. Altogether, these studies show that the Northern Hemisphere large scale circulation is strongly influenced by the Earth's orographical features.

Observational studies of synoptic scale transient eddies and the storm tracks in the Northern Hemisphere show that they are influenced by topography. Blackmon (1976), Blackmon *et al.* (1977), Wallace (1983), Blackmon *et al.* (1979), Hsu (1987), and Buzzi and Tosi (1989) completed statistical analyses of high frequency traveling eddies. Hsu and Buzzi and Speranza showed that traveling eddies tend to move north and rotate anticyclonically as they flow over the Rocky Mountains. By using the variance of the data, they showed that the storm track is interrupted by the mountain. There is strong evidence of the storm track over the Pacific Ocean and east of the Rocky Mountains but there is a minimum in activity over the mountains.

Pfeffer *et al.* (1989) and Li *et al.* (1986) conducted experimental studies using a thermally driven, rotating annulus with two wave bottom topography which simulates the behavior of the large scale, atmospheric flow. They also found there is a standing wavenumber two, with high pressure associated with the mountain ridge. They showed that as the rotation rate increases, the high pressure ridge of the standing wave is shifted upstream from the mountain.

Some theoretical work has been done using wavy basic states which may be forced by topography or other atmospheric phenomena. Niehaus (1980) used a wavy basic state that looked like the observed climatology for winter to do a linear stability analysis of a continuous, baroclinic model. She compared wavy basic states and skewed basic states which have zonal as well as meridional structure. She found the skewed basic state to be more favorably configured for unstable waves to grow. Derome (1984) showed how to

find a steady-state, wavy basic state for a baroclinic model that is an exact solution to the nonlinear quasi-geostrophic potential vorticity equation and thermodynamic conditions at the upper and lower boundaries. The wavy basic state indicates the storm track regions and regions of localized growth.

A considerable amount of theoretical work has been done on the subject of topographic instability. Topographic instability may be defined as a process of wave growth without propagation. It is caused by the interaction of the mean zonal flow with topography. The form drag equation couples the acceleration of the mean zonal flow with the drag induced by the topography. Charney and DeVore (1979) used a barotropic model and Charney and Straus (1980) used a baroclinic model to investigate the phenomenon of topographic instability. Revell and Hoskins (1984) argued that topographic instability can occur in Charney and DeVore's barotropic model but probably does not exist in Charney and Straus' baroclinic model since more realistic primitive equation models do not show this form of instability. They suggest that the lack of modes in the meridional direction in Charney and Straus' model was the cause. Källen (1983) showed that topographic instability can occur in a baroclinic model like Charney and Straus' if a source of momentum is included to drive a zonal flow. Buzzi *et al.* (1984) also used a baroclinic model with a barotropic forcing component to show topographic instability of the type found by Charney and DeVore.

In this thesis, we developed a simple mathematical model to describe a planetary scale basic flow and the smaller scale, baroclinic disturbances. We scaled the governing equations so that they would describe these two different scales of motion. Based on the scaling of the governing equations, we found that the flows could be described using the quasi-geostrophic potential vorticity equation and thermodynamic equations at the upper and lower boundaries. The effects of topography enter the problem through the

thermodynamic equation at the lower boundary. The equations are valid for non-dimensional mountain heights on the order of the Rossby number.

We linearized the model about a basic state that was wavenumber two in the x-direction and had linear vertical shear. We took the model to be periodic in x and y with a rigid upper lid and $\cos(2Kx)$ bottom topography. Since the model is periodic in y, side wall boundary conditions are not considered.

To force the x-dependent basic state, we need a constant zonal flow at the surface which interacts with the topography. In the atmosphere, a constant zonal flow results from eddy momentum flux convergence into the mid-latitudes. Since we chose periodic sidewall boundary conditions, the model cannot describe momentum flux convergence. As a result, the constant zonal flow enters this problem as a free parameter.

We solved the linear quasi-geostrophic potential vorticity equation and thermodynamic equations at the upper and lower boundaries by analytical and numerical techniques. The analytical solution uses asymptotic expansions in a small parameter related to the mountain height. The leading order problem is the Eady problem. At the next order enters the correction to the Eady problem due to topography and wavy basic state. We find that the frequency from the leading order problem is also the frequency for the next order where the correction due to topography enters the problem. Thus, all of the modes found in the first two orders of this problem will have the same frequency and growth rate. The numerical solution involves Fourier transforming the equation from grid space to spectral space. This gives a set of amplitude equations which can be solved using an eigenvector, eigenvalue routine to find growth rates, frequencies, and amplitudes of the spectral coefficients. The eigenvectors are used to reconstruct the streamfunction. The results from the analytical model help us to understand the results from the numerical model.

In Chapter 2, we review observational evidence from the atmosphere and the annulus

that suggests the influence of topography on the flow. In Chapter 3, we develop the baroclinic model we will use to investigate flow over topography. In Chapter 4, we solve the model using a numerical and an analytical technique. Finally, in Chapter 5, we discuss results and conclusions.

CHAPTER 2

ATMOSPHERIC AND ANNULUS OBSERVATIONS

Observations from the atmosphere and from annulus experiments with topography show flow patterns that are related to topographic forcing. By studying atmospheric variability we may learn about the geographical distribution of the geopotential height field at different vertical levels for different time scales. Low frequency variability indicates the nearly stationary pattern in the atmosphere. The long wave spectrum of low frequency variability dominates the climatology of the 500 mb geopotential height field. From the climatology we find the relationship between the nearly stationary, planetary scale waves and topographic features. High frequency variability indicates the storm tracks and regions of high eddy activity. Thus, we can learn about the relationship of high frequency eddies to topographic features and to the long wave environment. Laboratory experiments using a rotating annulus with a thermally driven fluid and topography provide another way to understand the interaction of large scale flow with topography. In this chapter, we look at observational evidence of topographic influences on atmospheric and annulus flows.

2.1 Atmospheric Observations

2.1.1 Geographical Distribution of Low Frequency Variability

If topography plays an important role in atmospheric flows, then it should leave a signature that can be identified by observational studies of atmospheric variability of the Northern Hemisphere. There should be a signature due to topography in the nearly

stationary, long wave pattern as well as the higher frequency baroclinic eddies. Blackmon (1976) and Blackmon *et al.* (1977, hereafter BWLM) studied the geographical distribution of low frequency variability on the time scale of greater than 10 days. Low frequency variability indicates the nearly stationary flow pattern. They analyzed data from the 500 mb NMC analysis for 18 winter seasons in the Northern Hemisphere. Based on the time filtering scheme they chose, a low pass filter gathered data with periods greater than 10 days, a medium pass or band pass filter gathered data with periods between 2.5 - 6 days.

Figure 2.1 from Blackmon (1976) shows maps of the 500 mb rms geopotential height surface for the low pass filtered data for all wavelengths. The pattern is almost identical to the unfiltered 500 mb rms geopotential surface (not shown). Thus, the 500 mb climatology shown in Figure 2.2 from Blackmon (1976) is dominated by low-frequency components. The 500 mb climatology shows a high pressure ridge over the Rocky Mountains and the Tibetan Plateau. Wavenumber two dominates the pattern. In a topographical study of the Earth's surface, Grose and Hoskins (1979) used a spectral analysis to show that wavenumber two dominates the surface.

There are many possible mechanisms in addition to topography which could force low frequency variability. One explanation suggests it is due to slowly varying thermal forcing from the oceans. Another explanation uses the index cycle in which there are vacillations from the high index state with strong westerlies and weak eddies to the low index state with weak westerlies and large amplitude waves. A third explanation for low frequency variability is the interaction of orographically forced waves with slow moving transient planetary waves such as Rossby waves which interact and produce long lived, large amplitude waves. A fourth explanation is forcing by high frequency baroclinic eddies which transfer their energy up the scale to the longer waves.

Finally, a fifth explanation suggests that topography forces the low frequency

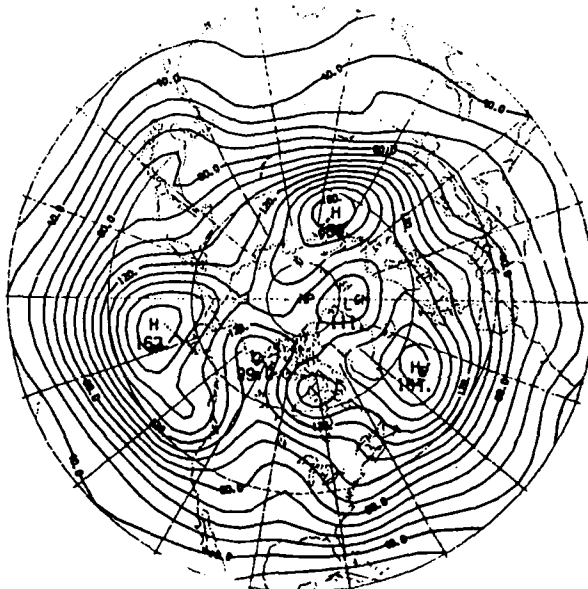


Figure 2.1 Map of low pass filtered rms geopotential at 500 mb for nine winters. Emphasizes fluctuations in periods longer than 10 days. The contribution from the mean annual cycle has been removed. Contour interval is 10 m. From Blackmon (1976).

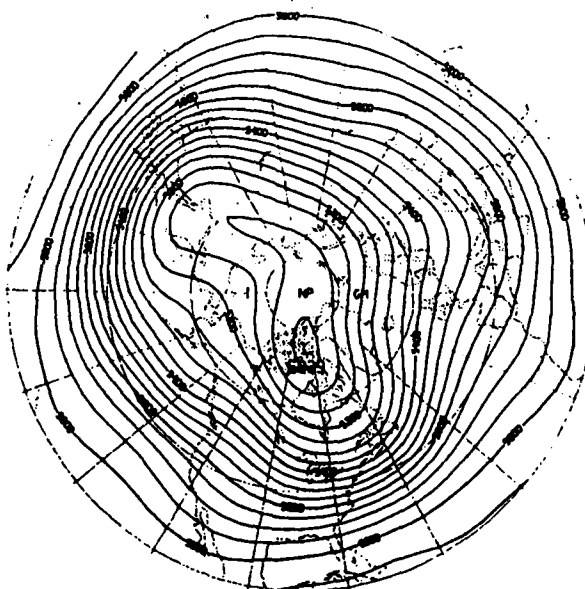


Figure 2.2 Climatological mean 500 mb height field for winter. Contour interval is 50 m. From Blackmon (1976).

variability of the atmosphere. Figure 2.3 taken from Blackmon, Lee, and Wallace (1984, hereafter BLW) shows (a) the 500 mb and (b) the 1000 mb height patterns averaged over 24 days beginning on 31 December 1980. For this 24 day period, a strong ridge is centered over the Rocky Mountains with deep troughs over the Pacific and North America. This pattern has been observed during many winter periods. When the remaining days of that winter were averaged in, the composite map looked very much like the 500 mb climatological map shown in Figure 2.2. Since this pattern has been observed many times, it may be said that this represents one of the atmosphere's preferred responses to the Rocky Mountains.

However, there are other ways the atmosphere could adapt to the Rocky Mountains. Figure 2.4 also taken from BLW shows (a) the 500 mb and (b) the 1000 mb geopotential height patterns for 22 days during the winter of 1980. In this figure, the 500 mb ridge is located over the Gulf of Alaska so that the flow runs parallel to the Rockies. Figure 2.3 showed the flow was nearly perpendicular to the Rocky Mountains. At 1000 mb, the flow shown in Figure 2.4 is easterly over the Rockies whereas it is westerly in Figure 2.3. Also, Figure 2.3 shows the vertical structure is more baroclinic than in Figure 2.3 where the wave is nearly vertically stacked. In Section 3.6, we will consider a baroclinic basic state which is forced by topography. For this basic state, the flow will be similar to the case in Figure 2.3.

2.1.2 High Frequency Variability

Blackmon (1976), BWLM, Wallace and Blackmon (1983), Hsu (1987), and Buzzi and Tosi (1989) studied the geographical distribution of high frequency variability. High frequency variability indicates storm track regions. Hsu (1987) applied statistical analysis on band pass filtered data in the vicinity of mountain ranges. He found that synoptic scale eddies, both cyclones and anticyclones, in the vicinity of large mountain ranges tend to

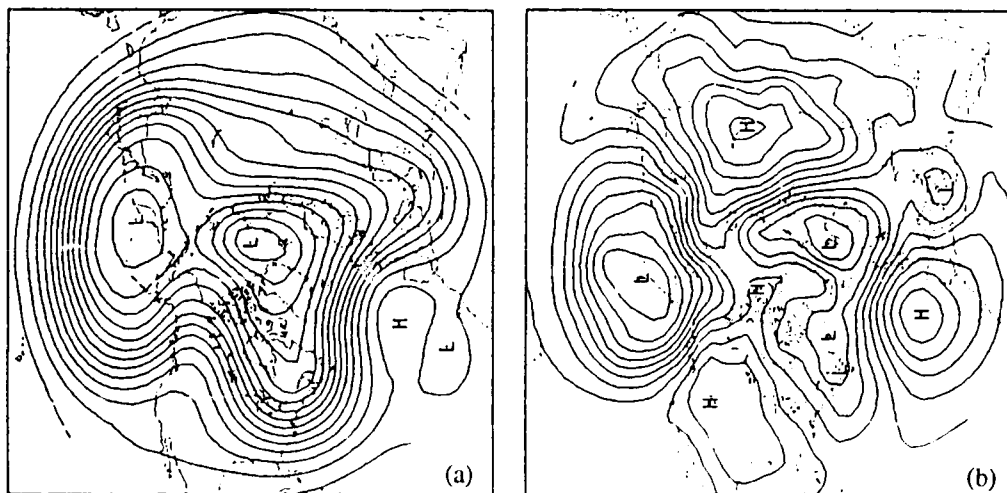


Figure 2.3 Composite geopotential height patterns for 24-day period beginning 31 December 1980, based upon daily analyses made at ECMWF. (a) 500 mb height, contour interval is 60 m and (b) 10 mb height, contour interval 30 m. From Blackmon, Lee, and Wallace (1984).

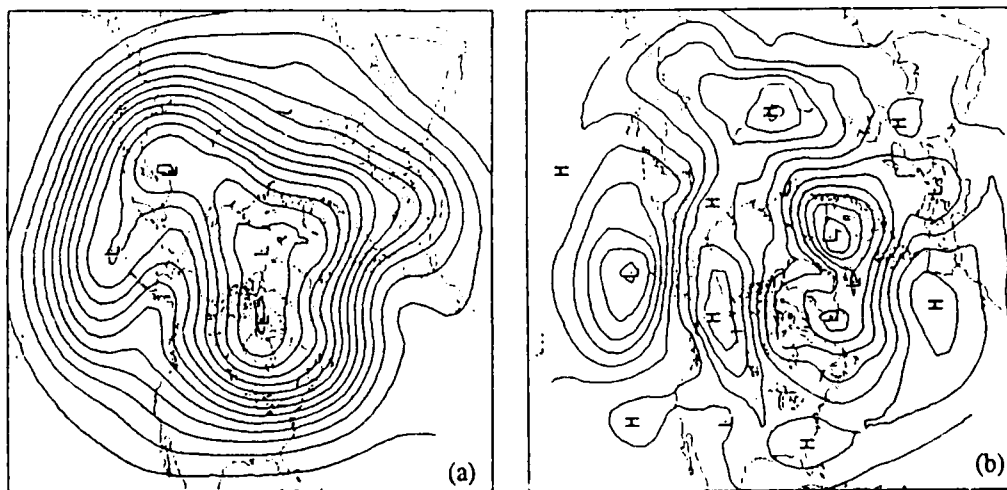


Figure 2.4 Composite geopotential height patterns for the 22 days 1-9 and 18-24 December 1980 and 5-10 February 1981, inclusive. Based on daily analyses made at ECMWF. From Blackmon, Lee, and Wallace (1984).

rotate anticyclonically around the mountain. This may be understood in terms of a barotropic explanation which says that potential vorticity is conserved. The potential vorticity may be expressed as

$$Q = \frac{\zeta + f_0 + \beta_0 y}{D + h},$$

where Q is the potential vorticity, f_0 is the planetary vorticity evaluated at some mid-latitude, β_0 is the beta-effect at that latitude, h is the mountain height, D is the average depth of the fluid, and ζ is the relative vorticity. As the eddy flows up the mountain slope, the depth of the fluid decreases. To conserve absolute vorticity, the relative and/or planetary vorticity also must decrease. Since it is observed that the eddies move to the north as they flow over the mountains, the planetary vorticity also increases. Therefore, the relative vorticity must decrease and the eddy rotates anticyclonically. A baroclinic explanation for the eddies turning north would be in terms of adiabatic warming and cooling of the fluid. The adiabatic, thermodynamic energy equation could be used to show that as the fluid rises, it cools adiabatically. The adiabatic cooling would induce a meridional circulation which advects warm air from the south and also advects the eddy to the north. In the atmosphere, there must be a combination of both the baroclinic and barotropic mechanisms. In Chapter 4 of this thesis, we will use a baroclinic model with a constant zonal flow to show the northward excursion of eddies as they pass over a mountain; in particular we propose to consider the f -plane dynamics.

Buzzi and Tosi (1989, hereafter BT) extended the work of Hsu. They examined the spatial structure of high-frequency variability near mountains including the Rocky Mountains. In particular, they studied the effect of orography on baroclinic eddies that have periods of a week or less. They used time series of geopotential height at 850 and 500 mb derived from 6-hour initialized analyses of ECMWF for the period November

1979 - December 1986. They analyzed the time series with a band pass filter to isolate the baroclinic eddies which have periods less than one week. They included data from all seasons but high-frequency variability is greatest during winter so their results should be more representative of the colder months.

Figure 2.5 from BT shows a map of (a) the 850 mb mean geopotential height, (b) the 850 mb standard deviation of the high-pass filtered geopotential, (c) the 500 mb mean geopotential height, and (d) the 500 mb standard deviation of the high-pass filtered geopotential over the Rocky Mountains. The relative maximum in the standard deviation over the Pacific to the west of the mountains shows the storm tracks at both 850 and 500 mb. The storm track is interrupted over the mountains where the standard deviation shows a minimum at both levels. To the east of the mountains, there is a relative maximum at 850 mb that suggests the storm track migrates to the south at low levels but simply reforms east of the mountains at 500 mb.

In addition to studying the variance of the eddies, BT used an analysis technique based on one-point lag correlation statistics. Their technique was to select a base gridpoint near the mountain range. Then, they computed lag-correlations between the time series at the base gridpoint and the time series at all other gridpoints and at all levels. The lag correlation maps provide information on the spatial structure of the eddies in the region surrounding the base gridpoints. This is possible since eddies preserve spatial structure over a time period greater than its local period and over a distance greater than its mean wavelength. Lag correlation maps may be compared to synoptic maps but heights cannot be interpreted as the geopotential height.

Figure 2.6 from BT shows the one-point lag correlation maps for several lag times of the high-pass filtered data of the sea-level pressure at $(54^{\circ}\text{N}, 129^{\circ}\text{W})$ marked with a dot and the sea-level pressure at all other gridpoints. To produce the maps, they selected data

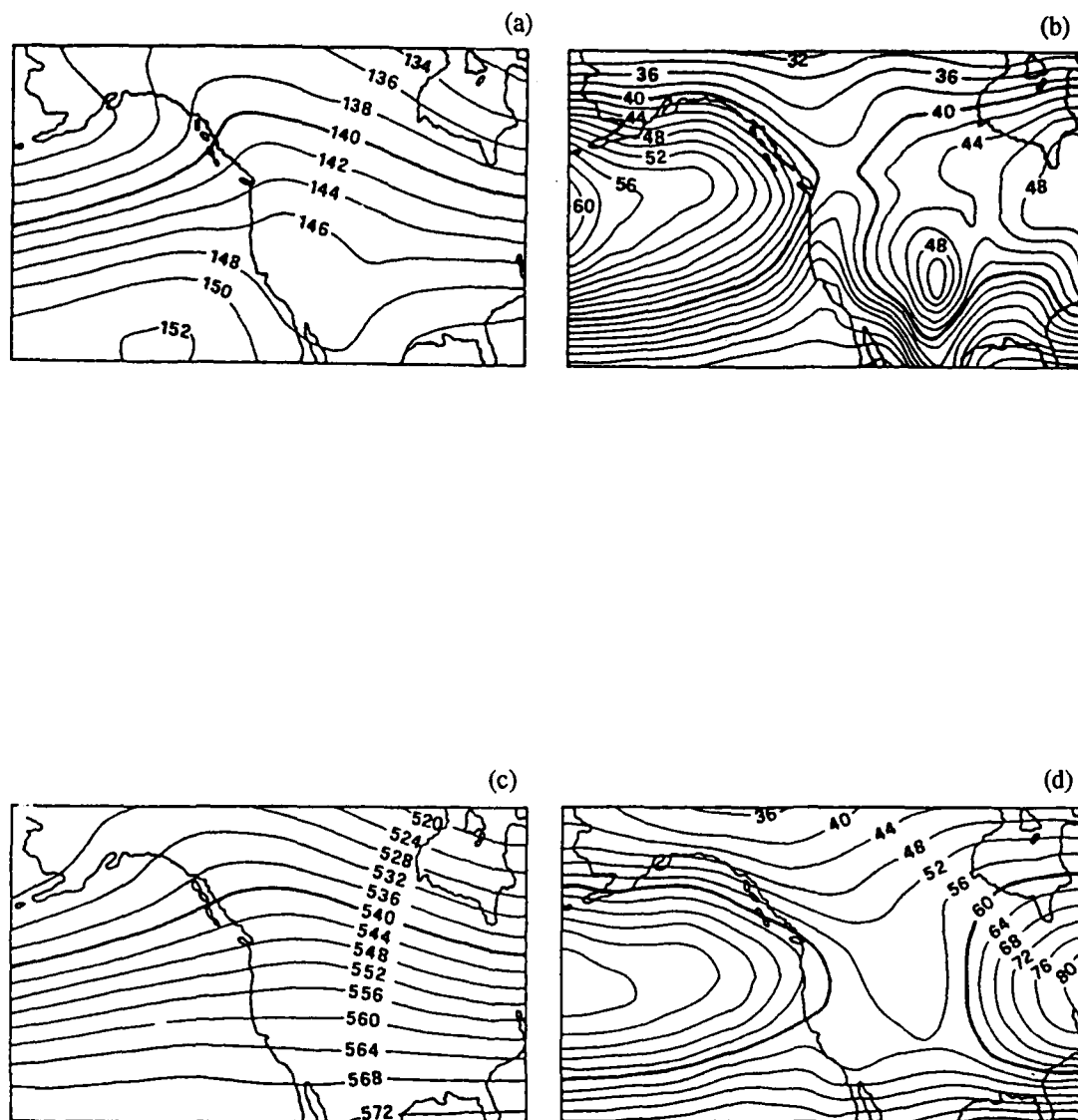


Figure 2.5 Climatology of the 850 and 500 mb levels for the area of the Rocky Mountains. (a) 850 mb mean geopotential height and (b) standard deviation of the high pass filtered geopotential height divided by the sine of the latitude. (c) 500 mb mean geopotential and (d) is the standard deviation. From Buzzi and Tosi (1989).

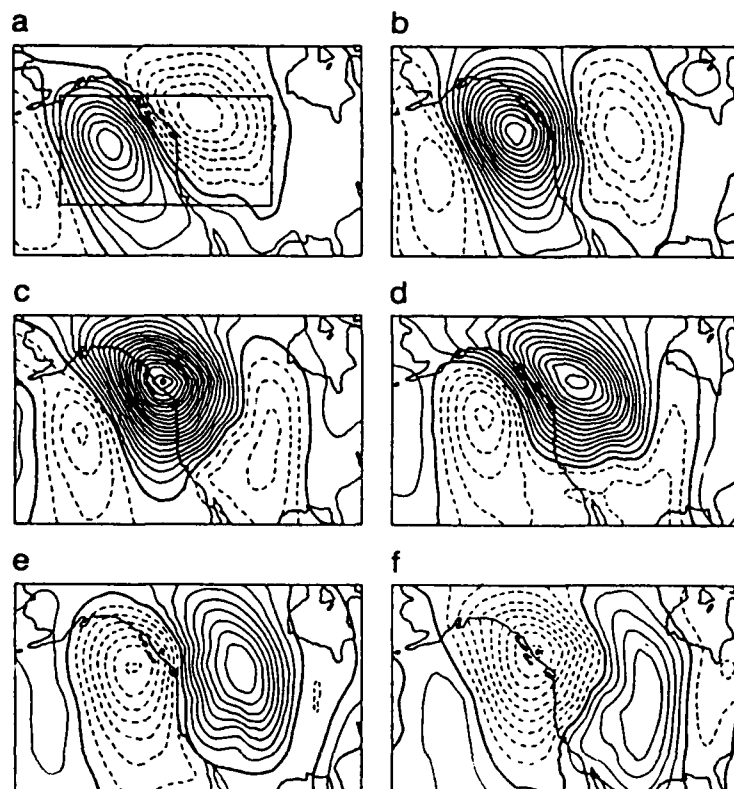


Figure 2.6 Maps of lagged correlation coefficients between the high-pass filtered 850mb level at 54°N , 129°W and the high pass filtered 850 mb level at every other grid point. The black dot show this location. Each plot shows a different lag time. (a) -24 hr, (b) -12 hr, (c) zero lag, (d) +12 hr, (e) +24 hr, (f) +36 hr. Contour interval is 0.05 and negative values are dashed. From Buzzi and Tosi (1989).

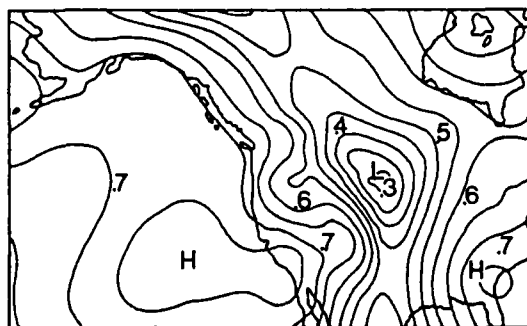


Figure 2.7 Correlation values between high-pass filtered 850 mb level and high pass filtered 500 mb level at every grid point. Area includes the Rocky Mountains. From Buzzi and Tosi (1989).

only if the wind direction was within an angle of $\pm 10^\circ$ of the zonal wind direction. Figure 2.6 shows that the path followed by the eddies is anticyclonically curved around the mountain as noted by Hsu (1987).

Figure 2.7 from BT shows the correlation between the 850 mb and 500 mb levels. The two levels are highly correlated to the west of the Rocky Mountains but there is a minimum to the east of the mountains. This may be interpreted as the local maximum tilt of the vertical eddy structure. The maximum vertical tilt is due to low level temperature anomalies; as the air flows down the mountains slope, it warms adiabatically.

2.1.3 Climatology of Northern Hemisphere Wintertime Stationary Waves

Held (1983) ran a general circulation model with and without topography and showed that topography plays a major role in determining the longitude of the major wintertime troughs and ridges in the Northern Hemisphere 500 mb geopotential height pattern. The climatology for the Northern Hemisphere winter shows a similar longitude dependence. This suggests that topography plays an important role in determining the Northern Hemisphere climatology.

In a climatological study, Lau (1979) showed both horizontal and vertical cross sections of geopotential that appear to be strongly influenced by the topography. Figure 2.8 (a) - (c) from Lau shows a longitude-height section of the stationary wave geopotential height pattern at three different latitudes for the winter season, derived from 11 years of NMC operational analyses. A two wave pattern dominates the cross section at 45°N and 60°N . There are high pressure ridges over the Rocky Mountains ($\sim 110^\circ\text{W}$) and the Tibetan Plateau ($\sim 115^\circ\text{E}$). He showed that these standing features appear in individual years as well as the climatology.

Figure 2.2 shows the climatological mean for the 500 mb geopotential height field for January. Again, wavenumber two dominates the geopotential height pattern and ridges are

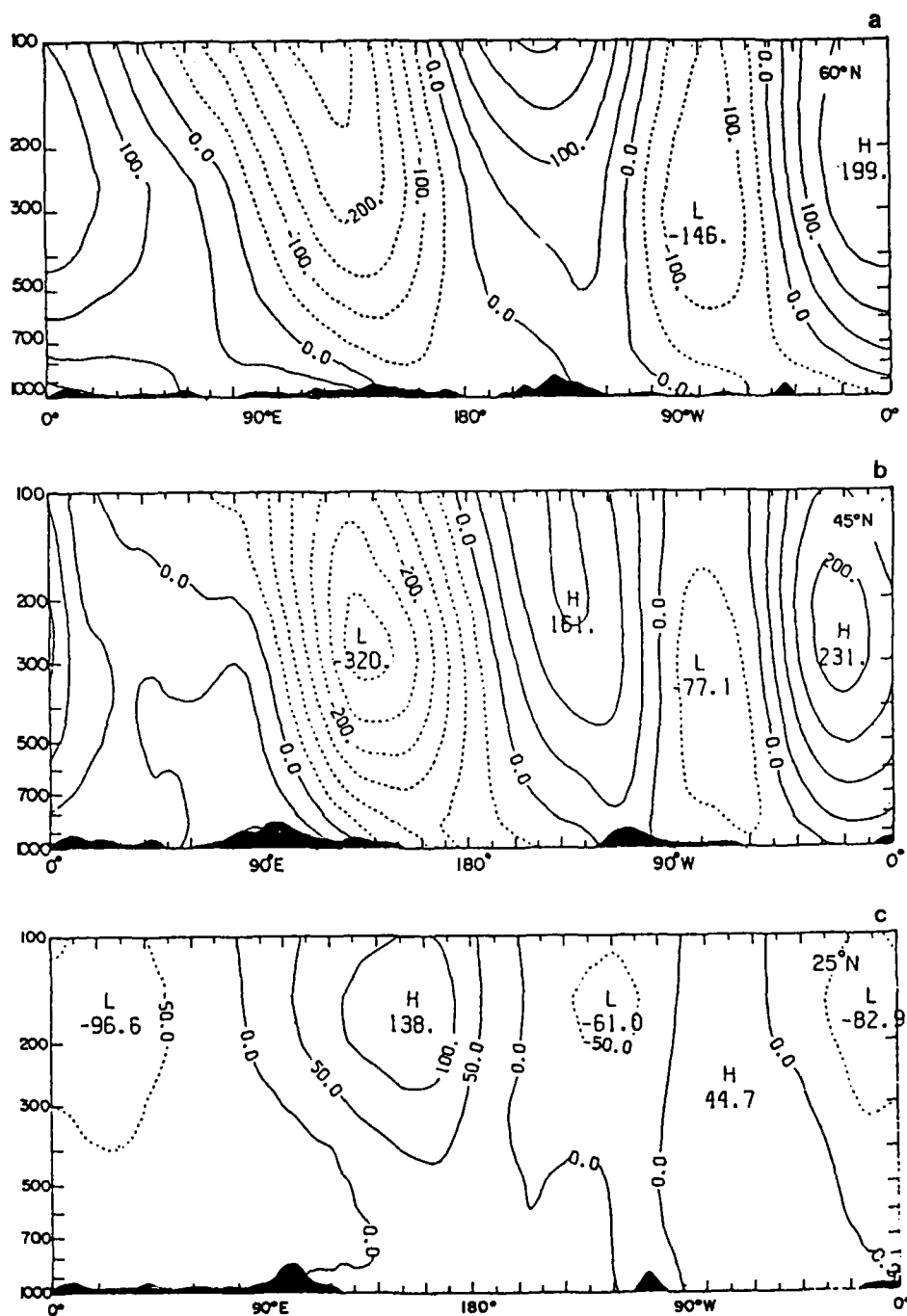


Figure 2.8 Longitude-height cross sections of departure from zonal symmetry of the time-averaged geopotential height taken along (a) 60°N, (b) 45°N, and (c) 25°N latitude circle. Contour interval is 50 m. The local orography is depicted at the bottom of the figure. From Lau (1979).

located over the Rocky Mountains and the Tibetan Plateau. The sea-level pressure field (not shown) does not show a wavenumber two forced by mountains but rather strong thermal influences along the coast. Land-sea temperature differences play a major role in the low level climatology. Held's (1990) numerical model also produces this observed climatological pattern.

2.2 Annulus Observations

To simulate some of the processes of the general circulation of the earth's atmosphere, Pfeffer *et al.* (1989) and Li *et al.* (1986) conducted numerous laboratory experiments in a thermally driven, rotating annulus with flow forced over a two-wave sinusoidal bottom topography. The selection of wavenumber two is motivated by the dominance of the wavenumber two in the earth's topography. Results from annulus experiments may be compared to theoretical models intended to describe flow in the annulus over a broad range of parameters. In Chapter 4 of this thesis, we present more details about the experiment and the parameter ranges studied.

Figure 2.9, taken from Pfeffer *et al.* (1989), shows the zonal wavenumber spectra of streamfunction at mid-radius in the annulus for several rotation rates. Figure 2.9 (a) represents the time average of the sequence of individual spectra of streamfunction which includes traveling and standing waves. At low rotation rates, wavenumbers two and five dominate but as the rotation rate increases, wavenumber four dominates and the even harmonics have the largest amplitudes. Figure 2.9 (b) represents the spectra of the time mean of the streamfunction. This figure shows the climatology or the standing waves. The amplitude of wavenumber two dominates the climatology and the even harmonics have the largest amplitudes. The fact that the even

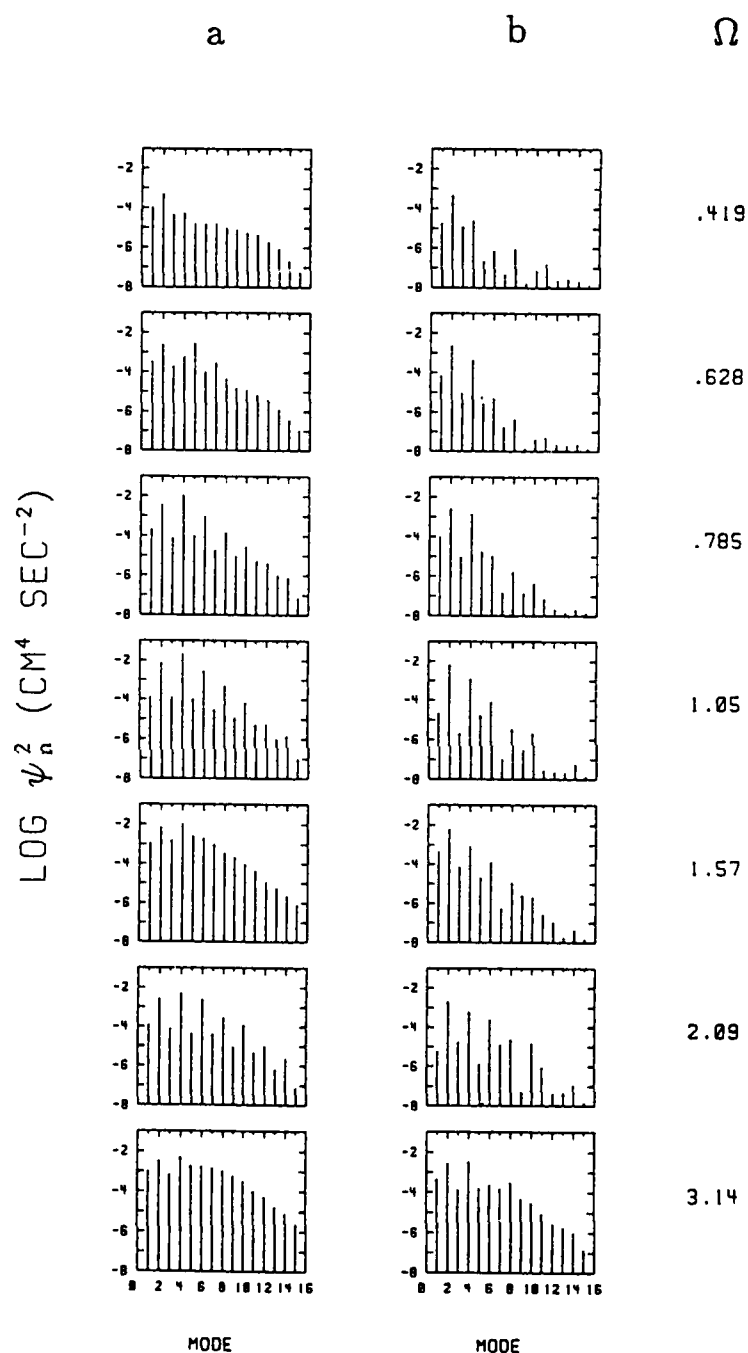


Figure 2.9 Zonal wavenumber spectra of ψ at mid-radius for seven different rotation rates. (a) Time averages of the sequence of individual spectra of ψ and (b) spectra of the time-averaged (or climatological) ψ field representing the standing waves. From Pfeffer *et al.* (1989).

harmonics dominate suggest there are non-linear interactions with wavenumber two forced by topography. Figure 2.10, also taken from Pfeffer *et al.* (1989), shows the climatological time-averaged and zonally-averaged velocity profile, U , as a function of radius, the time-averaged streamfunction, and the time-averaged or standing wavenumber two at various rotation rates. At low rotation rate, the zonal current is strong and the standing wave is weak. At higher rotation rates, the standing wave is stronger and the zonal flow decreases. At low rotation rates, the highs in the wavenumber two pattern are nearly standing on the mountain ridge as is observed in the atmosphere. At higher rotation rates, the high pressure is phase shifted upstream from the ridge of the mountain.

In summary, topography plays an important role in determining the large scale flow as well as the synoptic scale flow as observed in the atmosphere and the annulus. The climatological or nearly stationary pattern appears to be dominated by a standing wave number two in both the atmosphere and the annulus. Also, topography affects the baroclinic eddies as observed in the atmosphere. In the remainder of this thesis, we will use theoretical models to study the standing wavenumber two pattern and the effects of topography and standing waves on the traveling baroclinic eddies.

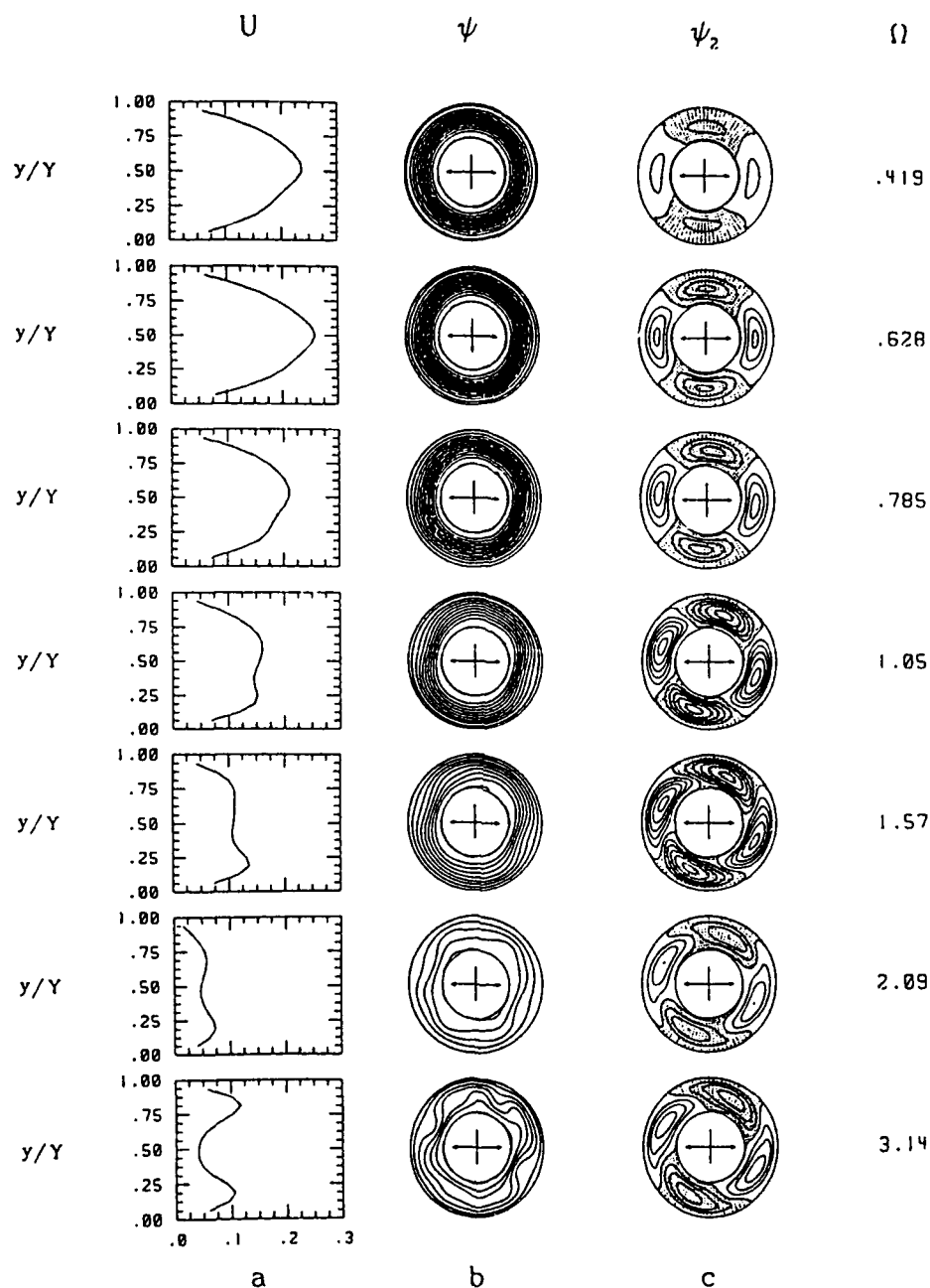


Figure 2.10 Velocity data based on measurements taken at a depth of 5.7 cm in seven experiments at different rotation rates. (a) Time- and zonally -averaged velocity profile (U). Here, y is the distance from the outer toward the inner wall and Y is the gap width of the annulus. (b) Time-averaged streamfunction, ψ . Contour interval is $0.1 \text{ cm}^2 \text{ s}^{-1}$. (c) Time-averaged wavenumber 2 component of the streamfunction, determined by Fourier analyses of ψ . Units of U are cm s^{-1} . Contour interval is $0.02 \text{ cm}^2 \text{ s}^{-1}$. Arrows indicate locations of topographic ridges. From Pfeffer *et al.* (1989).

CHAPTER 3

MODEL FORMULATION

In this chapter, we develop a mathematical model within the quasi-geostrophic framework to describe the interaction of the planetary and synoptic scale baroclinic flows with a two-wave bottom topography. We selected wavenumber two since it dominates the Earth's topography. To gain insight into the physical mechanisms involved in the flow, we use a simple set of governing equations and seek analytical solutions. We transform the equations to sigma coordinates and then to non-dimensional form. After simplifying the equations using order of magnitude arguments, we form the quasi-geostrophic potential vorticity equation. In our model, the effects of topography enter the problem through the lower thermodynamic equation and there is a rigid upper lid. Finally, we consider the form-drag equation.

3.1 Governing Equations

Pedlosky (1987) gives the complete set of governing equations in spherical coordinates for the atmosphere. Bird, Stewart, and Lightfoot (1960) give the governing equations in cylindrical coordinates for the annulus. We can simplify and write the governing equations in Cartesian coordinates if we choose to:

- (1) Neglect curvature effects.
- (2) Approximate the Earth's rotational effect with an f-plane.
- (3) Assume a static state exists in the absence of motion.

- (4) Use the Boussinesq approximation.
- (5) Make the hydrostatic approximation.
- (6) Assume fluid parcel motions are adiabatic.
- (7) Use no heat sources or sinks.
- (8) Neglect Ekman dissipation.
- (9) Neglect internal dissipation.

Using the list of assumptions given, we write the governing equations for the model as follows:

$$\frac{d\vec{V}}{dt} + f \vec{k} \times \vec{V} + \frac{1}{\rho_0} \nabla P = 0, \quad (3.1.1)$$

$$\frac{\partial P}{\partial z} = -g\rho, \quad (3.1.2)$$

$$\vec{\nabla} \cdot \vec{V} + \frac{\partial w}{\partial z} = 0, \quad (3.1.3)$$

$$\rho = \rho_0 (1 - \alpha(T - T_0)), \quad (3.1.4)$$

and

$$\frac{dT}{dt} = 0, \quad (3.1.5)$$

where

$$\frac{d}{dt} = \frac{\partial}{\partial t} + u \frac{\partial}{\partial x} + v \frac{\partial}{\partial y} + w \frac{\partial}{\partial z}.$$

The horizontal momentum equation is given by (3.1.1) where \vec{V} represents the horizontal velocity vector. Equation (3.1.2) is the hydrostatic approximation and (3.1.3) is the continuity equation. Equation (3.1.4) is the equation of state for a liquid where T_0 is a reference temperature and α is the coefficient of volumetric expansion; this equation satisfies the Boussinesq approximation. Equation (3.1.5) is the adiabatic thermodynamic energy equation.

In this problem we consider flows of two different length scales; waves forced by topography which are planetary in scale and growing baroclinic eddies which are synoptic in scale. We expect that the governing equations, (3.1.1) - (3.1.5), can describe both of these scales. Let us consider the scale for the planetary waves and the validity of the assumptions we applied. Namely, how important are the curvature of the Earth and the beta effect for planetary scale waves? In Appendix A we scale the horizontal momentum equations in spherical and cylindrical coordinates to estimate the magnitude of the Earth's curvature compared to advective terms and we consider the beta-plane approximation to estimate the magnitude of the beta effect compared to the constant vorticity taken in the f-plane approximation. We summarize the results here. In Section 3.3, we scale the equations for synoptic scale motions.

To neglect curvature effects in models intended to describe planetary scale flow of the atmosphere or in the annulus, the length scale of the phenomena should be much smaller than the Earth's radius or the annulus radius. If to a first approximation we consider the Earth's surface to be two waves in the zonal direction, then the typical horizontal length scale of a standing wave forced by the topography is approximately one half the magnitude of the Earth's radius. In the annulus experiment, there is a two wave sinusoidal topography which will force a standing wavenumber two. Again, the horizontal length scale is approximately one half the magnitude of the radius of the annulus. Thus, curvature effects are important to describe properly planetary scale flow forced by topography. By including these effects, the analytical solution would be very complicated and a numerical solution would be easier. We expect that the curvature terms will bring some correction to the simple, analytical model we solve. In our model, we chose to neglect curvature effects in favor of the advective terms.

We approximated the Earth's rotational effect with an f-plane rather than using a beta-

plane approximation. In the atmosphere, the standing, planetary scale waves forced by topography will have large north-south excursions and the beta effect would be important. In the rotating annulus, the bottom surface is not radially dependent but there is a sloping upper surface which simulates the beta effect. In either case, a better approximation than the f-plane is the beta-plane. In Appendix A, we compare the f-plane and beta-plane approximations and show the magnitude of the beta effect is of the same order as the Rossby number for planetary scale waves. To describe planetary scale waves we should include the beta effect if we include the advective terms which are of the same order. To describe both planetary scale and synoptic scale motions, we need the beta effect and advective terms. We consider synoptic scales in Section 3.3. In this model, we chose a standing planetary scale wave forced by topography but not by the beta effect. This represents a serious deficiency in the model. However, the stability analysis in Chapter 4 focuses on baroclinic eddies within the long wave environment where the beta effect is not as important for synoptic scale waves as for planetary scale waves.

In (3.1.2) we assume that vertical accelerations are small compared to the rotational effects so the hydrostatic approximation is valid. For this approximation to remain valid in the model with mountains, the height of the mountain should be less than or equal to the magnitude of the Rossby number (Pedlosky, 1987).

3.2 Transformation of Equations To Sigma Coordinates

One way to solve this problem would be to assume that the mountain height is small compared to a characteristic vertical scale. Then, we could linearize the lower boundary condition and apply it on the $z = 0$ surface as shown by Phillips (1963). This approximation is invalid if the mountain height is much larger than the Rossby number.

Another possible way to solve this problem would be to transform the equations to a terrain following coordinate system. Malguzzi (1987) showed that if the topography is steep, they had to abandon the z -coordinate system in favor of a sigma coordinate system. To solve this problem, we transform our equations to a terrain following or sigma coordinate system.

We define a new vertical coordinate such that

$$\sigma(x,z) = \frac{D(z - h(x))}{(D - h(x))}, \quad (3.2.1)$$

where D is the average depth of the fluid, h is the height of the mountain, z is the height above the average mountain depth, and sigma is the new vertical coordinate as shown in Figure 3.1. In this coordinate system, when $z = h(x)$, $\sigma = 0.0$ and when $z = D$, $\sigma = D$. For this problem, we took the mountain to be x -dependent only. The Rocky Mountains extend for thousands of kilometers in the north-south direction and a good approximation for the model is to take a mountain that is infinite in y . In the annulus, the topography does not have any y -structure.

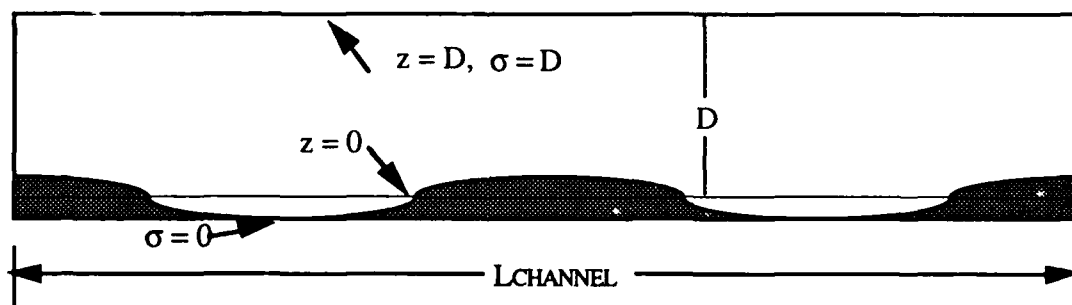


Figure 3.1 Cross section showing the relationship between the σ -coordinate and the z -coordinate. The shaded region indicates the topography. The surface $\sigma = 0$ is coincident with the topography. The surface $z = 0$ is at the midpoint between the trough and ridge. D is the average fluid depth.

To transform (3.1.1) - (3.1.5) from the Cartesian coordinate system to the sigma

coordinate system defined above, we use the following relations

$$\left(\frac{\partial F}{\partial x} \right)_{(z)} = \left(\frac{\partial F}{\partial x} \right)_{(\sigma)} + \frac{\partial F}{\partial \sigma} \left(\frac{\partial \sigma}{\partial x} \right)_{(z)}, \quad (3.2.2)$$

and

$$\frac{\partial F}{\partial z} = \frac{\partial F}{\partial \sigma} \left(\frac{\partial \sigma}{\partial z} \right)_{(z)}. \quad (3.2.3)$$

Thus, we have a general transformation from the z -coordinate system to the sigma coordinate system. For steep mountains, the sigma surfaces in the lower levels would be very wavy when viewed in a z -coordinate system. For the case of steep mountains, our transformation as defined here becomes invalid. Pielke (1984) and Dutton (1976) show the appropriate transformation to a generalized non-orthogonal coordinate system in the case of steep mountains. For this problem, we used mountains with gentle slopes.

Using the transformations (3.2.2) and (3.2.3), we find

$$\dot{\sigma} = \frac{d\sigma}{dt} = u \left(\frac{\sigma - D}{D - h} \right) \left(\frac{\partial h}{\partial x} \right) + w \left(\frac{D}{D - h} \right) \quad (3.2.4)$$

and

$$w = \dot{\sigma} \left(\frac{D - h}{D} \right) - u \left(\frac{\sigma - D}{D} \right) \left(\frac{\partial h}{\partial x} \right), \quad (3.2.5)$$

Also, we find the following operators apply in the sigma-coordinate system

$$\frac{d}{dt}(\sigma) = \left[\frac{\partial}{\partial t} + \vec{V} \cdot \nabla \vec{V} \right]_{(\sigma)} + \dot{\sigma} \frac{\partial}{\partial \sigma} \quad (3.2.6)$$

and

$$\nabla(z) = \nabla(\sigma) + \left(\frac{\sigma - D}{D - h} \right) \left(\frac{\partial h}{\partial x} \right) \frac{\partial}{\partial \sigma}. \quad (3.2.7)$$

Pedlosky (1987) argued that in the absence of rotation, we expect there is some "standard" atmosphere that is only a function of the vertical coordinate. If we form a global average of the pressure, P , and temperature, T , and assume we can write the average as the

static pressure, $P_s(z)$, and temperature, $T_s(z)$, then we can write the total pressure and temperature as

$$P(x,y,z,t) = P_s(z) + P'(x,y,z,t), \quad (3.2.9)$$

and

$$T(x,y,z,t) - T_0 = T_s(z) + T'(x,y,z,t), \quad (3.2.10)$$

where $P'(x,y,z,t)$ and $T'(x,y,z,t)$ represent spatial and temporal perturbations to the static state P_s and T_s . When we transform the equations to the sigma coordinate system, we will keep $P_s(z)$ and $T_s(z)$ as functions of z .

Using these operators and definitions, we may write the governing equations in sigma coordinates as follows

$$\frac{d\vec{V}}{dt} + f\vec{k} \times \vec{V} + \frac{1}{\rho_0} \nabla P' + \left(\frac{\sigma - D}{D} \right) \left(\frac{\partial h}{\partial x} \right) g T' \alpha = 0, \quad (3.2.11)$$

$$\frac{\partial P'}{\partial \sigma} = g \rho \alpha \left(\frac{D - h}{D} \right), \quad (3.2.12)$$

$$(D - h) \left(\vec{\nabla} \cdot \vec{V} + \frac{\partial \dot{\sigma}}{\partial \sigma} \right) - u \frac{\partial h}{\partial x} = 0, \quad (3.2.13)$$

and

$$\frac{dT'}{dt} + \left[\dot{\sigma} \left(\frac{D - h}{D} \right) + u \left(\frac{\sigma - D}{D} \right) \left(\frac{\partial h}{\partial x} \right) \right] \left(\frac{dT_s}{dz} \right) = 0. \quad (3.2.14)$$

At the upper and lower rigid boundaries, we require that $\dot{\sigma} = 0$ at $\sigma = 0, 1$ which simplifies the thermodynamic equation, (3.2.14).

3.3 Scaling

In Section 3.1, we considered the effects of curvature and beta effect on the planetary scale flows and found that the beta effect is important. Now we consider the scale for synoptic flow within the long wave environment. We anticipate that the beta effect is not as

important for this scale of flow. Here, we examine typical synoptic scales for the atmosphere and the annulus following Charney (1948). By comparing the magnitudes of various terms in the equations, we eliminate terms based on scaling arguments. Also, we present a more detailed description of the annulus experiment.

We choose the following scales for the atmosphere or the annulus:

- (1) $(x,y)* [=] L(x,y)$, horizontal length scale,
- (2) $\sigma_* [=] D \sigma$, vertical length scale, average depth of the fluid,
- (3) $(u,v)* [=] U(u,v)$, horizontal motion,
- (4) $w_* [=] Uh/L(w)$, vertical motion, from scaling the continuity equation,
- (5) $T'_* [=] \Delta T_H(T')$, scale for temperature perturbations,
- (6) $T_{S*} [=] \Delta T_V(T_S)$ - scale for the imposed temperature gradient,

where * represents dimensional quantities. By including the scale in these equations, all of the dependent and independent variables are dimensionless. If we combine these scales into the governing equations in place of the corresponding variables, we can non-dimensionalize the equations by dividing through by the scales on one term. Following this procedure, we find the non-dimensional governing equations are

$$\epsilon \frac{du}{dt} - v + \frac{\partial p'}{\partial x} + \delta (\sigma - 1) T' \frac{\partial \eta}{\partial x} = 0, \quad (3.3.1)$$

$$\epsilon \frac{dv}{dt} + u + \frac{\partial p'}{\partial y} = 0, \quad (3.3.2)$$

$$\frac{\partial p'}{\partial \sigma} = T'(1 - \delta \eta), \quad (3.3.3)$$

$$\vec{\nabla} \cdot \vec{V} + \delta \frac{\partial \sigma}{\partial t} - \frac{\delta}{(1 - \delta \eta)} u \frac{\partial \eta}{\partial x} = 0, \quad (3.3.4)$$

and

$$\frac{dT'}{dt} + v(1 - \delta\eta) \left[\dot{\sigma} - u \frac{\partial \eta}{\partial x} (\sigma - 1) \right] \frac{dT_s}{dz} = 0, \quad (3.3.5)$$

where

$$\frac{d}{dt} = \frac{\partial}{\partial t} + \vec{V} \cdot \nabla + \delta \dot{\sigma} \frac{\partial}{\partial \sigma},$$

$$\epsilon = \frac{U}{fL} = \text{Rossby number},$$

$$v = \frac{S\delta}{\epsilon},$$

$$\delta = \frac{h}{D},$$

$$S = \left(\frac{ND}{Lf} \right)^2 = \text{Burger number},$$

and $\eta = \cos(2Kx)$ which represents the topography. δ is a non-dimensional mountain height. The Burger number may be thought of as a measure of the stratification or a measure of the Rossby radius of deformation to the horizontal length scale. In the remainder of this work, we will assume that N^2 is not a function of z . The Rossby radius of deformation gives the scale for which we expect baroclinic instability to occur.

The non-dimensional parameter, v , is a measure of the relative strength of adiabatic cooling versus horizontal temperature advection. When we apply the boundary condition $\dot{\sigma} = 0$ at $\sigma = 0, 1$, (3.3.5) will be applied at the upper and lower boundaries. At the upper boundary, the last term on the left hand side of the equation is zero and there will only be temperature advection. At the lower boundary, v becomes important. For a given stratification and Rossby number, the magnitude of the mountain effect is dominated by the mountain height. The last term in (3.3.5) implies that any zonal flow, u , which flows over the mountain slope, $\partial\eta/\partial x$, will rise and cool adiabatically. This causes an imbalance in (3.3.5). To overcome the imbalance, a southerly flow is induced which advects warm air

from the south.

The mountain in this problem is slowly varying in the x-direction and has a large horizontal length scale compared to the Rossby radius of deformation so that $S < O(1)$. For smaller horizontal length scale mountains, $S \sim O(1)$. Therefore, in this model, baroclinic instability will occur for scale of motions where L is approximately L_D and $S \sim O(1)$. This argument about length scales suggests that the mountain will force planetary scale flows by the adiabatic cooling and southerly advection of temperature but should have less impact on the growth of disturbances. Since baroclinic eddies propagate within the planetary scale flow, the large scale flow will act as a wave guide for the smaller scale eddies.

The magnitude of v will determine how large the mountain appears to the fluid. If v is small, due to any combination of Burger number, Rossby number or mountain height, the mountain effect is small. If v is an $O(1)$ quantity, the mountain effect will become very important.

Typical dimensional and non-dimensional parameters for synoptic scale motions in the atmosphere are

- (1) $U = 10 \text{ m s}^{-1}$
- (2) $W = Uh/L = 10^{-2} \text{ m s}^{-1}$
- (3) $L = 10^6 \text{ m}$
- (4) $D = 10^4 \text{ m}$
- (5) $L/U = 10^5 \text{ s}$
- (6) $h = 10^3 \text{ m}$
- (7) $\delta = h/D = .1$
- (8) $\epsilon = .1$
- (9) $S = .25$

$$(10) L_D = 10^6 \text{ m}$$

$$(11) v = .25$$

$$(12) N = 2.5 \times 10^{-3} \text{ s}^{-1}$$

D is taken as a typical measure of the depth of the troposphere, L is a measure of the horizontal length of the phenomena. It is important to distinguish between the synoptic scale and the planetary scale L . U is an average value of the wind through the troposphere. W can be estimated from the thermodynamic or vorticity equations, but in this problem we find the scale for W from the continuity equation and it is related to the mountain height. When the fluid interacts with the mountain, the magnitude of W will be larger than predicted by the thermodynamic or vorticity equations. We have taken an average value for the mountain height to be 1 km yielding $\delta = 0.1$ which is the same order as the Rossby number for synoptic scale motions. As we will see, this is a requirement for the quasi-geostrophic approximation to be valid. If the depth of the mountain were much larger than the Rossby number, the leading order balance would not be geostrophic. We have assumed the stratification is a linear function of z only and is not affected by the mountain. A value of $S = 0.25$ means that the length scale of the baroclinic disturbances is about one fourth the length scale of observed atmospheric phenomena.

Before listing parameter values for the annulus, we discuss the annulus experiments in more detail. The interested reader should refer to Pfeffer *et al.* (1989) or Li *et al.* (1986) for a complete discussion of the annulus, experimental procedures, and results.

To create an environment that simulates the Earth's atmosphere in a controlled way, Pfeffer *et al.* (1989) experiment with a rotating annulus. Briefly, the annulus is a rotating cylinder that is filled with silicone fluid. It is heated on the outer wall and cooled on the inner wall so that a radial temperature gradient develops and a baroclinic flow results. The imposed temperature gradient is maintained at 2°C . A two-wave sinusoidal topography

was placed on the bottom of the cylinder. For the experiments of interest to us, the mountain does not have any radial structure and there is no lid in contact with the fluid. Figure 3.2 (a) shows the top view of the annulus dimensions. The radius to the outer wall, $b = 14.9$ cm and to the inner wall, $a = 7.3$ cm. The circumference at mid-radius is $\pi(a+b)$. An azimuthal view of the annulus is shown in Figure 3.2 (b). For the length of the channel, we take the circumference at mid-radius. Therefore, the length of one mountain is half the channel length. We choose the length scale for the problem to be related to the mountain by

$$L = \frac{L_{\text{MOUNTAIN}}}{2\pi}$$

and the fundamental zonal wavenumber is

$$K = \frac{2\pi L}{L_{\text{CHANNEL}}} = .5,$$

and the fundamental meridional wavenumber is

$$l = \frac{\pi(a+b)}{4(b-a)}.$$

Typical dimensional and non-dimensional parameters for the annulus are given as follows:

- (1) $L = 5.55$ cm.
- (2) $D = 10$ cm.
- (3) $h = 1.75$ cm.
- (4) $\delta = .175$.

Pfeffer *et al.* (1989) and Li *et al.* (1986) ran a series of experiments at various rotation rates. The remainder of the parameters of the problem depend on the rotation rate. Table 3.1 shows the important parameters for the problem. As we will see, for the $O(\delta^1)$ approximation to be valid, the ratio of ϵ/δ must be approximately $O(1)$. Table 3.1 shows this quantity is less than $O(1)$ for all rotation rates. However, we will show in Section 3.4

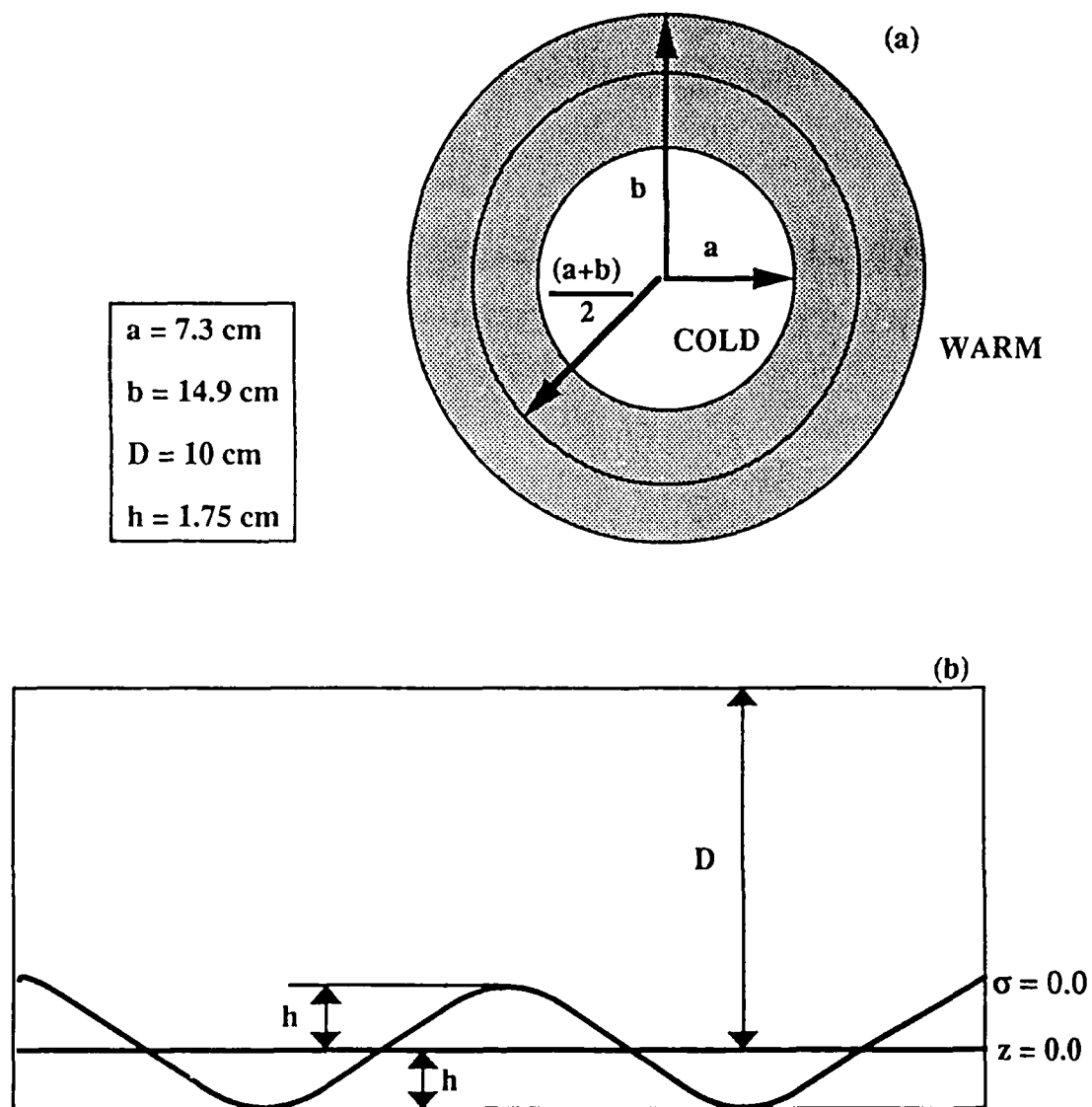


Figure 3.2 (a) Top view of the annulus where b is the outer radius and a is the inner radius, and (b) side view of the annulus dimensions where D is measured from the surface $z=0$.

that the ratio ϵ/δ does not appear in the quasi-geostrophic potential vorticity equation.

Rather, $v = S\delta/\epsilon$ appears in the thermodynamic equation at the lower boundary. This quantity is $O(1)$ for all rotation rates. Therefore, we expect our scaling to be valid for most rotation rates.

Using these scale parameters, we can scale the governing equations. If we assume that $\delta \sim O(\epsilon)$, we can rewrite the problem using an asymptotic expansion in the small parameter δ such that

$$\begin{aligned} P' &= P_0 + \delta P_1 \dots, \\ \text{and} \quad T' &= T_0 + \delta T_1 \dots \\ \text{etc...} \end{aligned} \tag{3.3.6}$$

Table 3.1 Typical scale parameters for the annulus as a function of rotation rate. U is a time averaged value from 6.5 cm at mid-radius are listed. $L = 5.55\text{cm}$. The topography is $\cos(2Kx)$.

Ω (rad s ⁻¹)	0.628	0.785	1.05	1.57	2.09	3.14
U (cm s ⁻¹)	0.32	0.44	0.29	0.15	0.11	0.08
L_D (cm)	3.62	2.89	2.16	1.44	1.09	0.72
ϵ	0.046	0.050	0.024	0.009	0.005	0.002
ϵ/δ	0.262	0.285	0.137	0.051	0.029	0.011
S	0.425	0.271	0.151	0.067	0.039	0.017
v	1.62	0.95	1.10	1.30	1.37	1.49

Collecting terms of the same order, we find the leading order, non-dimensional problem, $O(\delta^0)$, to be

$$-v_0 + \frac{\partial P_0}{\partial x} = 0, \tag{3.3.7}$$

$$u_0 + \frac{\partial P_0}{\partial y} = 0, \quad (3.3.8)$$

$$\frac{\partial P_0}{\partial \sigma} = T_0, \quad (3.3.9)$$

$$\vec{\nabla} \cdot \vec{V}_0 = 0, \quad (3.3.10)$$

and

$$\left(\frac{dT_0}{dt} \right)_0 + v \left(\dot{\sigma}_0 - u_0 \frac{\partial \eta}{\partial x} (\sigma - 1) \right) = 0. \quad (3.3.11)$$

where

$$\left(\frac{d}{dt} \right)_0 = \frac{\partial}{\partial t} + J(P_0, \cdot)$$

and

$$\frac{dT_s}{dz} = 1.$$

To leading order, the flow is geostrophic. The boundary conditions are that $\dot{\sigma} = 0$ at the upper and lower boundaries.

At the next order, $O(\delta^1)$, we find the correction to geostrophy to be

$$\left(\frac{\epsilon}{\delta} \right) \frac{du_0}{dt} - v_1 + \frac{\partial P_1}{\partial x} + (\sigma - 1) \frac{\partial \eta}{\partial x} T_0 = 0, \quad (3.3.12)$$

$$\left(\frac{\epsilon}{\delta} \right) \frac{dv_0}{dt} + u_1 + \frac{\partial P_1}{\partial y} = 0, \quad (3.3.13)$$

and

$$\vec{\nabla} \cdot \vec{V}_1 + \frac{\partial \dot{\sigma}_0}{\partial \sigma} - u_0 \frac{\partial \eta}{\partial x} = 0, \quad (3.3.14)$$

where the ratio ϵ/δ is to be viewed as an $O(1)$ quantity for the atmosphere. However, the magnitude of this ratio is $O(10^{-1})$ for the annulus. We can justify keeping this term in spite of the scaling. The effect of topography is greatest at the lowest levels of the fluid but is smallest at the upper level where advection is most important. In (3.3.12) when $\sigma = 0$ at

the bottom of the fluid, the balance may be between the last three terms on the left hand side of this equation. However, when $\sigma > 0$, the last term on the left hand side of (3.3.12) is small and now the balance must be between the first three terms. For this order, we included only those equations required for the following derivations.

3.4 Quasi-Geostrophic Model

Next, we can form the quasi-geostrophic potential vorticity equation using the $O(\delta^0)$ and $O(\delta^1)$ equations outlined in Section 3.3. The static temperature was taken as a function of the z -coordinate only when we transformed the equations to the sigma coordinate system. Physically, this makes good sense since in the absence of motion, the stratification is a function of z and does not vary along the new vertical coordinate. This assumption simplifies the final form of the equations. If we take the static temperature to be a linear function of the vertical coordinate, the Brunt Väisälä frequency becomes a constant. We can form the vertical vorticity equation by taking $\partial(3.3.12)/\partial y$ minus $\partial(3.3.13)/\partial x$. Next, we can solve for $\dot{\sigma}$ in (3.3.11) and substitute for v_0 using (3.3.7), u_0 using (3.3.8), and T_0 using (3.3.9) and obtain the expression

$$\frac{\partial \dot{\sigma}_0}{\partial \sigma} = -\frac{1}{v} \left[\frac{\partial}{\partial t} + J(P_0, \cdot) \right] \left(\frac{\partial^2 P_0}{\partial \sigma^2} \right) + J \left(\frac{\partial P_0}{\partial \sigma}, \frac{\partial P_0}{\partial \sigma} \right) - (\sigma - 1) \frac{\partial \eta}{\partial x} \left[-\frac{\partial}{\partial \sigma} \left(\frac{\partial P_0}{\partial y} \right) + \frac{\partial}{\partial y} \left(\frac{\partial P_0}{\partial \sigma} \right) \right] \quad (3.4.1)$$

where the last term on the right hand side is the thermal wind balance and cancels. The second term on the right hand side is also zero but this is true only since we took T_s to be a function of z . There is a vertical derivative of the static temperature implied in the second term but we took this term to be one. If we combine the vertical vorticity equation and (3.4.1), the quasi-geostrophic potential vorticity equation can be written as

$$\left[\frac{\partial}{\partial t} + J(P_o, \sigma) \right] \left(\nabla^2 P_o + \frac{1}{S} \frac{\partial^2 P_o}{\partial \sigma^2} \right) = 0. \quad (3.4.2)$$

In the final form of the vorticity equation, only the Burger number appears as a non-dimensional parameter and the ratio of δ/ϵ canceled out of the problem.

The thermodynamic equation with the boundary condition $\dot{\sigma} = 0$ at the upper and lower surfaces may be written as

$$\frac{\partial}{\partial t} \left(\frac{\partial P_o}{\partial \sigma} \right) + J \left(P_o, \frac{\partial P_o}{\partial \sigma} \right) + (\sigma - 1) v \frac{\partial P_o}{\partial y} \frac{\partial \eta}{\partial x} = 0. \quad (3.4.3)$$

The last term on the left hand side of the equation only has a value when $\sigma = 0$, at the lower boundary. It represents the interaction of the low level zonal flow with the mountain. The non-dimensional number $v = (S\delta/\epsilon)$ controls the magnitude of this term which physically describes adiabatic heating and cooling due to the flow over the topography. If the non-dimensional mountain height, δ , is small compared to the Rossby number, ϵ , then the mountain will not play a major role in the problem. If $v \sim O(1)$, then this term is important in balancing the full thermodynamic equation. If the mountain height is very large compared to the Rossby number so that $v > O(1)$, then the approximations used to derive the quasi-geostrophic equations are invalid. Malguzzi (1987) showed that the quasi-geostrophic approximation is invalid for steep mountains. The geostrophic and hydrostatic approximations allow us to write the pressure, P_o , in terms of the streamfunction, $\psi = P_o$, so that (3.4.2) and (3.4.3) become

$$\left[\frac{\partial}{\partial t} + J(\psi, \sigma) \right] \left(\nabla^2 \psi + \frac{1}{S} \frac{\partial^2 \psi}{\partial \sigma^2} \right) = 0, \quad (3.4.4)$$

$$\frac{\partial}{\partial t} \left(\frac{\partial \psi}{\partial \sigma} \right) + J \left(\psi, \frac{\partial \psi}{\partial \sigma} \right) + (\sigma - 1) v \frac{\partial \psi}{\partial y} \frac{\partial \eta}{\partial x} = 0. \quad (3.4.5)$$

Equations (3.4.4) and (3.4.5) constitute the governing equations for the remainder of this work.

3.5 Linearized Quasi-Geostrophic Model

We are primarily interested in testing the stability of basic states representative of flow over topography. To that end, we seek to linearize the equations about a basic state and so we split the total streamfunction into basic state and perturbation components as follows

$$\psi(x,y,\sigma,t) = \Psi(x,y,\sigma) + \phi(x,y,\sigma,t). \quad (3.5.1)$$

Here, Ψ represents the steady basic state which in this problem is a function of the x -coordinate as well as the y - and σ -coordinates. Substituting for ψ in (3.4.4) with (3.5.1), we find

$$\begin{array}{cccccc} \frac{\partial q}{\partial t} & + & J(\Psi, \Pi) & + & J(\Psi, q) & + & J(\phi, \Pi) & + & J(\phi, q) & = & 0, \\ (a) & (b) & (c) & (d) & (e) & & & & & & \end{array} \quad (3.5.2)$$

where the perturbation potential vorticity, q , is defined as

$$q = \nabla^2 \phi + \frac{1}{S} \frac{\partial^2 \phi}{\partial \sigma^2}$$

and the basic state potential vorticity, Π , is defined as

$$\Pi = \nabla^2 \Psi + \frac{1}{S} \frac{\partial^2 \Psi}{\partial \sigma^2}.$$

In (3.5.2), term (a) represents the local rate of change of the perturbation potential vorticity. Term (b) represents the basic state advection of the basic state potential vorticity. Term (c) represents the basic state advection of the perturbation potential vorticity. Term (d) represents the perturbation advection of the basic state potential vorticity. Term (e)

represents the nonlinear perturbation advection of the perturbation potential vorticity.

Substituting for ψ in (3.4.5) with (3.5.1), the thermodynamic boundary conditions may be written as

$$\begin{array}{cccccc} \frac{\partial}{\partial t} \left(\frac{\partial \phi}{\partial \sigma} \right) & + & J \left(\Psi, \frac{\partial \Psi}{\partial \sigma} \right) & + & J \left(\Psi, \frac{\partial \phi}{\partial \sigma} \right) & + & J \left(\phi, \frac{\partial \Psi}{\partial \sigma} \right) & + & J \left(\phi, \frac{\partial \phi}{\partial \sigma} \right) & = & 0 \\ \text{(a)} & & \text{(b)} & & \text{(d)} & & \text{(e)} & & \text{(f)} & & \end{array} \quad (3.5.3)$$

at $\sigma = 1$, and

$$\begin{array}{cccccc} \frac{\partial}{\partial t} \left(\frac{\partial \phi}{\partial \sigma} \right) & + & J \left(\Psi, \frac{\partial \Psi}{\partial \sigma} \right) & + & J(\Psi, v \eta) & + & J \left(\Psi, \frac{\partial \phi}{\partial \sigma} \right) & + & J \left(\phi, \frac{\partial \Psi}{\partial \sigma} + v \eta \right) & + & J \left(\phi, \frac{\partial \phi}{\partial \sigma} \right) & = & 0 \\ \text{(a)} & & \text{(b)} & & \text{(c)} & & \text{(d)} & & \text{(e)} & & \text{(f)} & & \end{array} \quad (3.5.4)$$

at $\sigma = 1$. Equations (3.5.3) and (3.5.4) are the thermodynamic boundary conditions at the upper and lower boundaries. Equation (3.5.4) contains all of the terms that appear in (3.5.3) and the additional mountain terms for the lower boundary. Term (a) represents the local rate of change of the temperature. Term (b) represents basic state advection of the basic state temperature. Term (c) represents advection along the mountain slope. Term (d) represents basic state advection of perturbation temperature. Term (e) represents perturbation advection of the basic state temperature and the flow along the mountain slope. Term (f) represents the nonlinear perturbation advection of the perturbation temperature.

For the remainder of this problem, we select the linearized set of equations *with respect to the perturbation* and neglect the last term in (3.5.2), (3.5.3), and (3.5.4). In Section 3.6, we will find an x -dependent basic state which *exactly* satisfies all of the terms in each of these equations that do not contain the perturbation. In (3.5.2) and (3.5.3), term (b) will be exactly satisfied and equal to zero by our choice of basic state. In (3.5.4), terms (b) and (c) will sum to zero by our choice of basic state.

3.6 Wavy Basic State

In Chapter 2, we discussed the climatological mean and low frequency variability in the Northern Hemisphere winter circulation and the fact that low frequency variability accounts for the majority of the climatological distribution. If we assume these waves are standing, we can find steady state solutions to the quasi-geostrophic potential vorticity and thermodynamic equations at the upper and lower boundaries

The basic state we choose must be an exact solution to the quasi-geostrophic potential vorticity equation as well as the thermodynamic boundary conditions. One choice is to force the flow at the lower boundary to go to zero. This is a poor choice since there would be no interaction of the basic state flow with the mountain slope. Then, the interaction with the mountain must come into the problem at the order of the perturbation. A better choice is to allow for flow at the bottom boundary and let it interact with the mountain but this forces us to choose an x -dependent basic state.

Held and Ting (1990) stress the importance of the low level flow in forcing stationary waves. Using a numerical model with topography, they show that the amplitude of the forced stationary wave grows as the flow at the surface increases. In the atmosphere, the constant flow at the surface results from momentum flux convergence into the mid-latitudes from the tropics and in general the flow is westerly. This analytical model does not have side wall boundary conditions that can transport momentum from the tropics. Therefore, we must parameterize the constant zonal flow.

There have been many studies of the stability properties of zonal basic flows but there are comparatively fewer stability studies using wavy basic states. Grotjahn (1984) wrote a review article on wavy basic states used in linear, theoretical models of baroclinic instability. The majority of the works used two-layer, beta plane models. Niehaus (1980)

used a wavy basic state, and a continuous f-plane to do a linear instability analysis of a baroclinic flow. The choice of basic state was arbitrary. It was not forced by topography or heating but rather, it was chosen to match the observed conditions in the Northern Hemisphere winter. She compared wavy basic states and skewed, wavy basic states and found that the tilt in the basic state allows for a natural interaction between the forced wave and the instabilities. Without the skewness in the basic state, the fastest-growing instabilities had zero meridional wavenumber. For skewed basic states, the fastest growing instabilities were coupled to and modulated by the standing wave. Buzzi *et al.* (1984) studied the stability of a wavy basic state in a two-layer beta-plane model and a continuous f-plane model. In their linear stability analysis, the instability had the same wavenumber as the topography. They found topographic instability occurs for long waves; long waves which are beyond the cutoff for normal, traveling baroclinic waves. They compare the growth rates for wavy and non-wavy basic states in both models and found growth rates are slightly decreased for the case of a wavy basic state.

Derome (1984) shows one procedure to find *finite amplitude*, steady-state, x-dependent basic states which represent exact solutions to the nonlinear vorticity equation and boundary conditions. The importance of his work is that under certain circumstances, rather complex solutions to the linearized potential vorticity equation are also finite-amplitude solutions to the equations. His procedure is limited to inviscid problems.

In this section, we follow Derome's procedure to find an x-dependent, steady-state, baroclinic basic state. We assume the x-dependent basic state can be separated into one part that has linear vertical shear and an x-dependent part such that

$$\Psi(x, y, \sigma) = \bar{\Psi}_B(y, \sigma) + \phi_B(x, \sigma) \quad (3.6.1)$$

where

$$\bar{\Psi}_B(y, \sigma) = -y \left(U_0 + \lambda \left(\sigma + \frac{1}{2} \right) \right).$$

We used the subscript B to denote basic state quantities. Eady (1949) used a basic state with linear vertical shear to show the simplest form of baroclinic instability. Here λ represents the vertical shear and U_0 is a constant zonal flow. For convenience, we redefined the vertical coordinate so that the lower boundary is at $\sigma = -0.5$ and the upper boundary is at $\sigma = +0.5$. If we substitute this basic state into the quasi-geostrophic potential vorticity equation and boundary conditions, we can rewrite the equations as

$$\bar{U} \frac{\partial}{\partial x} \left(q_B + \frac{1}{\bar{U}} \frac{\partial \Pi_B}{\partial y} \phi_B \right) + J(\phi_B, q_B) = 0, \quad (3.6.2)$$

$$\bar{U} \frac{\partial}{\partial x} \left(\frac{\partial \phi_B}{\partial \sigma} - \frac{1}{\bar{U}} \frac{\partial \bar{U}}{\partial \sigma} \phi_B \right) + J \left(\phi_B, \frac{\partial \phi_B}{\partial \sigma} \right) = 0, \quad (3.6.3)$$

$$\bar{U} \frac{\partial}{\partial x} \left(\frac{\partial \phi_B}{\partial \sigma} - \frac{1}{\bar{U}} \frac{\partial \bar{U}}{\partial \sigma} \phi_B + v\eta \right) + J \left(\phi_B, \frac{\partial \phi_B}{\partial \sigma} + v\eta \right) = 0 \quad (3.6.4)$$

where

$$\bar{U} = - \frac{\partial \bar{\Psi}_B}{\partial y} = \left(U_0 + \lambda \left(\sigma + \frac{1}{2} \right) \right),$$

$$q_B = \nabla^2 \phi_B + \frac{1}{S} \frac{\partial^2 \phi_B}{\partial \sigma^2},$$

and

$$\Pi_B = \nabla^2 \bar{\Psi}_B + \frac{1}{S} \frac{\partial^2 \bar{\Psi}_B}{\partial \sigma^2}.$$

Equation (3.6.2) is the potential vorticity equation and (3.6.3) and (3.6.4) are the upper and lower boundary conditions. We note that if the first term on the left hand side of (3.6.2) - (3.6.4) is zero, then the second term also must vanish. This implies that

$$q_B = - \frac{1}{\bar{U}} \frac{\partial \Pi_B}{\partial y} \phi_B \quad (3.6.5)$$

is one of many exact solutions of the basic state potential vorticity equation. To simplify

further, we chose the Eady basic state so that $\Pi_B = 0$. It follows from (3.6.5) that $q_B = 0$. We could have taken q_B to be some other function of the vertical coordinate. A better choice would have included the β effect. A general solution for the streamfunction is

$$\phi_B(x, \sigma) = v F_B(\sigma) \cos(2Kx) \quad (3.6.6)$$

where

$$F_B(\sigma) = A_B \cosh(\gamma(\sigma - \frac{1}{2})) + B_B \sinh(\gamma(\sigma - \frac{1}{2})), \quad (3.6.7)$$

$$\gamma = 2K\sqrt{S},$$

and K is the fundamental wavenumber of the channel. The coefficients A_B and B_B are found to be

$$A_B = \frac{\gamma U_0 (U_0 + \lambda)}{\lambda \Delta} \quad (3.6.8)$$

and

$$B_B = \frac{U_0}{\Delta} \quad (3.6.9)$$

where

$$\Delta = \gamma^2 U_0 \sinh(\gamma) \left(1 + \frac{U_0}{\lambda} \right) + \lambda (\cosh(\gamma) - \sinh(\gamma)).$$

Knowing the vertical structure, we applied the upper and lower boundary conditions. We find the exact solution for this problem to be

$$\Psi = -y \left(U_0 + \lambda \left(\sigma + \frac{1}{2} \right) \right) + v F_B \cos(2Kx) \quad (3.6.10)$$

Figure 3.3 shows horizontal cross sections of the basic state at (a) the upper and (b) the lower boundaries, (c) an x - σ cross section down the center of the channel, and (d) an x - σ cross section of the x -dependent part of the basic state. The mountain ridge is at 0 and π rad. The high pressure is over the mountain ridge. Since the flow is inviscid and steady, there is no tilt of the basic state with height. If the flow were viscous, there would have been a tilt with height because the steady flow would extract energy from the basic state to

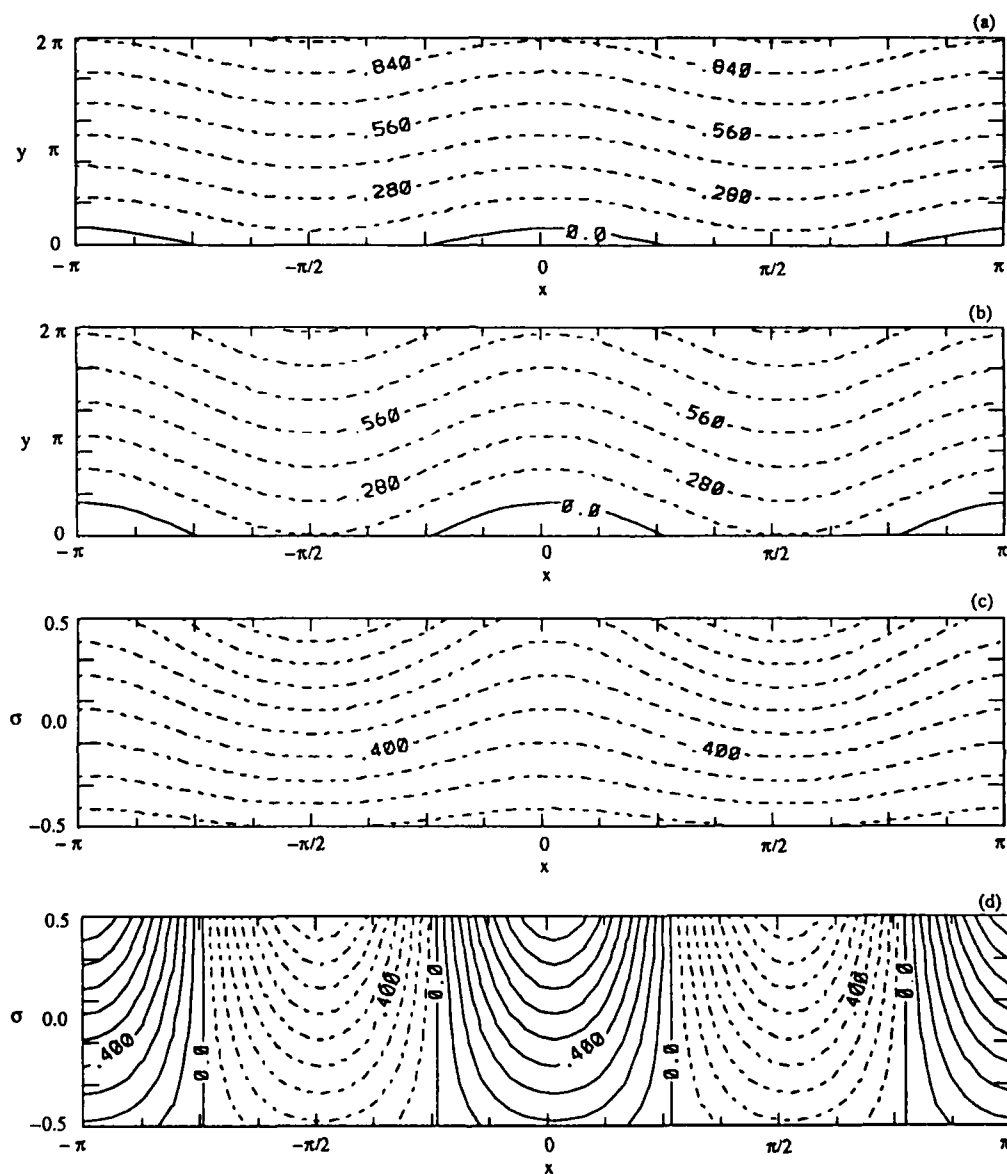


Figure 3.3 Basic state streamfunction where (a) is an x - y cross section at the top, (b) is an x - y cross section at the bottom, (c) is an x - σ cross section at mid-radius, and (d) is an x - σ cross section of the wavy part of the basic state at mid-radius. Mountain ridges are at 0 and π rad. $S = 0.25$, $U_0 = 0.1$, $\delta = 0.1$, and $\lambda = 1$.

overcome dissipation. These figures may be compared to the January climatology in Figures 2.2, 2.5, and 2.8.

Figure 3.4 shows the amplitudes of the coefficients A_B and B_B in (3.6.7) as a function of the basic flow, U_O . For negative values, the basic state is very sensitive to the magnitude of U_O , especially as U_O approaches -0.5. This happens because the denominator of Δ which is proportional to $(U_O + \lambda/2)$ becomes very small. Thus, as U_O approaches -0.5, the denominator gets very small and the amplitude of this term becomes very large. Negative values of U_O have a significant impact on the growth rates and frequencies of instabilities on this basic state as we will show in Chapter 4.

3.7 Topographic Instability and Form Drag

Unlike typical baroclinic and barotropic instability where the unstable waves propagate and grow, topographic instability is characterized by waves which grow but do not propagate. Several papers have been written on topographic instability. Charney and DeVore (1979, hereafter CD) showed topographic instability occurs in a barotropic, beta-plane channel model with dissipation and topography. Charney and Straus (1980, hereafter CS) showed topographic instability occurs in a baroclinic, two-layer, beta-plane channel model with dissipation and topography. Buzzi *et al.* (1984) showed topographic instability occurs in a baroclinic, two-layer, beta-plane channel model with dissipation, zonally symmetric and asymmetric basic states, and topography and also in a continuous, f-plane channel model with dissipation, zonally symmetric and asymmetric basic states, and topography. Yoden and Mukougawa (1983) used a baroclinic two-layer and 20-layer, low-order model to investigate flow over topography.

Källén (1983) found topographic instability in a baroclinic model that included a direct

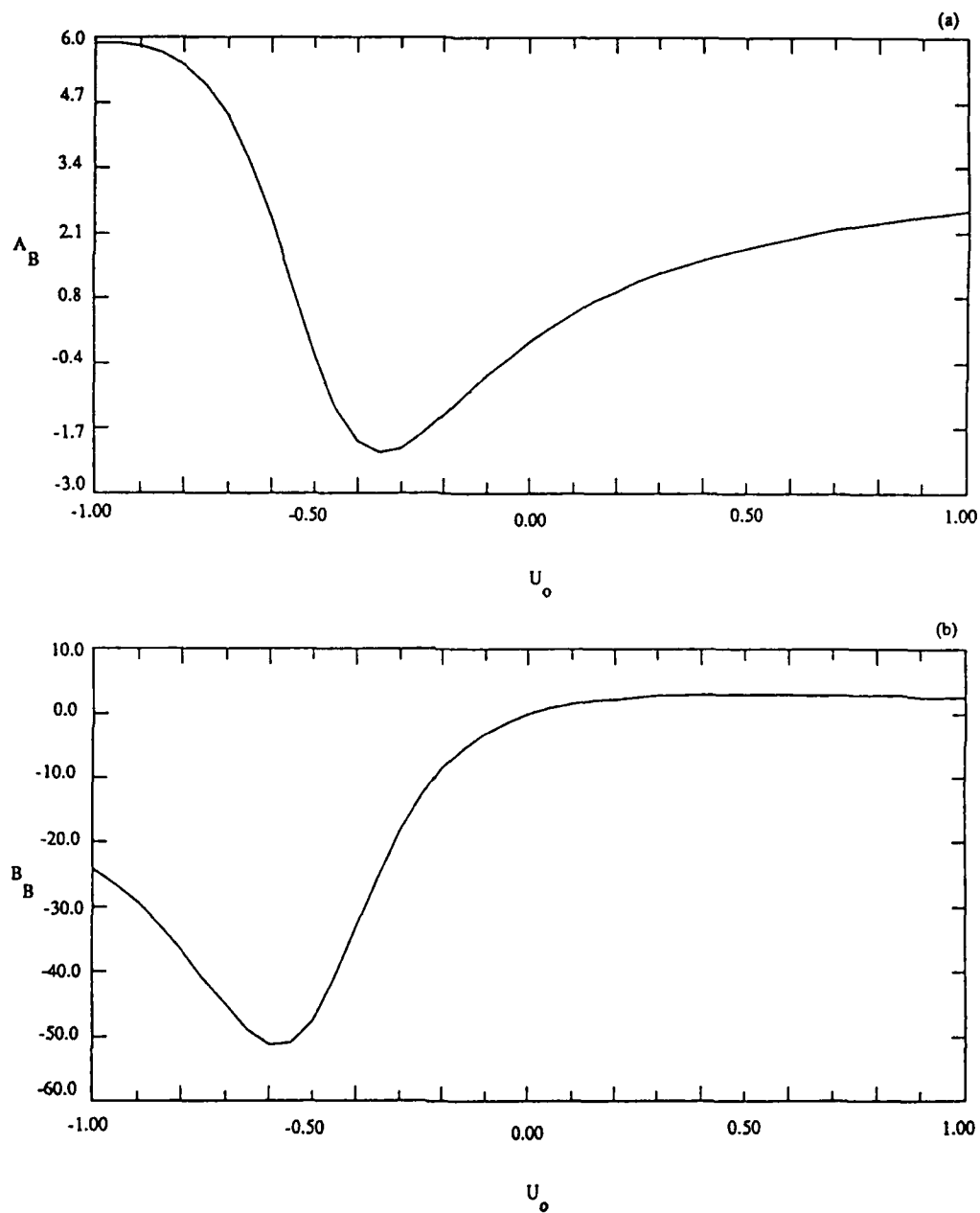


Figure 3.4 (a) Magnitude of the basic state coefficient A_B and (b) magnitude of the basic state coefficient B_B as a function of U_0 . $\lambda=1$, and $S = 0.25$.

momentum forcing in the vorticity equations in the lower level of his two layer model. He showed that topographic instability does not occur in baroclinic models unless a momentum source is included and pointed to some inconsistencies in the work of CS. In our baroclinic model, the momentum source is the constant zonal flow, U_0 .

Revell and Hoskins (1984, hereafter RH) critically reviewed CD's barotropic model and CS's baroclinic model. In their work, RH wanted to verify if topographic instability was different from baroclinic and barotropic instability. They present a thorough review of topographic instability in a barotropic and a baroclinic model. They found that topographic instability does exist in a barotropic model. However, in baroclinic models, the topographic instability appeared in simple, low order models but did not appear in more complete baroclinic models where classical baroclinic instability dominated at all wavenumbers. As RH pointed out, it would be difficult to verify topographic instability using real atmospheric data, however it does appear that the instabilities of the linearized problem play an important role in highly truncated, simple models. In this work, we will place more emphasis on trying to understand how baroclinic instability is modified rather than on topographic instability.

Buzzi *et al.* (1984) outline the process that leads to topographic instability in their models. The physical explanation for the instability starts with the form-drag mechanism. The topography exerts drag on the fluid due to surface pressure components out of phase with the topography. Drag leads to momentum exchanges between the wavy disturbances and the mean zonal flow. This implies there is a form-drag coupling between wavy disturbances and the mean zonal flow caused by topography. Form-drag coupling accelerates the mean zonal flow. We can derive the form-drag equation from the x-component of the momentum equation. Restating the $O(\delta^1)$ x-component of the momentum equation, where sigma now varies from -0.5 to 0.5

$$\left(\frac{\epsilon}{\delta}\right)\left(\frac{du_0}{dt}\right)_0 - v_1 + \frac{\partial P_1}{\partial x} + \left(\sigma - \frac{1}{2}\right)\frac{\partial \eta}{\partial x}T_0 = 0. \quad (3.7.1)$$

We can rewrite this equation in flux form as

$$\left(\frac{\epsilon}{\delta}\right)\left(\frac{\partial u_0}{\partial t} + \vec{\nabla} \cdot (u_0 \vec{V}_0) - (u_0 + v_0)\vec{\nabla} \cdot \vec{V}_0\right) - v_1 + \frac{\partial P_1}{\partial x} + \left(\sigma - \frac{1}{2}\right)\frac{\partial \eta}{\partial x}T_0 = 0. \quad (3.7.2)$$

If we substitute the leading order continuity equation, (3.3.9), and hydrostatic equation, (3.3.8), and integrate over volume, (3.7.2) may be written as

$$\int_{\text{vol}} \left\{ \left(\frac{\epsilon}{\delta}\right)\left(\frac{\partial u_0}{\partial t} + \vec{\nabla} \cdot (u_0 \vec{V}_0)\right) - v_1 + \frac{\partial P_1}{\partial x} + \left(\sigma - \frac{1}{2}\right)\frac{\partial \eta}{\partial x}T_0 \right\} d\text{vol} = 0. \quad (3.7.3)$$

(a) (b) (c)

In our model, we chose the streamfunction to be periodic in x and y . Therefore, terms (a) and (c) are zero. Term (b) is zero since there is no net north-south mass flux. Equation (3.7.3) reduces to the form

$$\int_{\text{vol}} \left\{ -\left(\frac{\epsilon}{\delta}\right)\frac{\partial}{\partial t}\left(\frac{\partial \psi}{\partial y}\right) + \left(\sigma - \frac{1}{2}\right)\frac{\partial \eta}{\partial x}\frac{\partial \psi}{\partial \sigma} \right\} d\text{vol} = 0. \quad (3.7.4)$$

In (3.7.4), the first term on the left hand side represents the acceleration of the zonal flow due and the second term represents a mountain torque. In Chapter 4, we will substitute for ψ using our assumed solutions and complete the integration of (3.7.4). We will use this equation to investigate topographic instability and show that topographic instability exists for perturbations with the same wavenumber as the topography and no y -structure. Based on the work of Revell and Hoskins (1984) and Källén (1983), we do not expect topographic instability unless there is flow at the surface. In Chapter 4 we solve the governing equations and include a constant zonal flow U_0 .

CHAPTER 4

ANALYTICAL AND NUMERICAL SOLUTIONS

In Chapter 3, we developed a mathematical model for large scale and synoptic scale, baroclinic flow over two-wave bottom topography. We chose a very simple model to focus on two important features of the flow; the large scale flow interacting with the mountain to force a wavy basic state and the synoptic scale flow interacting with the mountain and the basic state to form storm track regions and preferred regions for growth. We neglected the beta effect, friction, and curvature that would make our model more correct but also more complicated.

Many researchers have completed linear stability analyses and studied how orography modifies baroclinic instability. Källen (1983), Yoden and Mukougawa (1983), Speranza *et al.* (1985), Buzzi and Speranza (1986), and Buzzi *et al.* (1987), Reinhold (1990) have studied the problem using two-layer, baroclinic, beta-plane models with topography and dissipation. Yoden and Mukougawa (1983) studied baroclinic instability using a 20-layer sigma coordinate, beta-plane model with topography and dissipation. Niehaus (1980) and Speranza *et al.* (1985) studied modified baroclinic instability using a continuous, f-plane model with topography and dissipation. Malguzzi *et al.* (1987) studied the effect of finite height topography on non-geostrophic baroclinic instability and discussed the implications for simple theories of baroclinic instability. DeSzoeko (1983) studied the destabilizing effect topography has on otherwise stable waves. Buzzi *et al.* (1987) examined the interaction of a baroclinic eddy with topography using a linear, two-layer model. They use

only zonal basic flows. Therefore, they are studying how the perturbation interacts with topography. Buzzi *et al.* (1984) studied the effects that topography has on the growth rates of unstable modes. They find that the growth rates are decreased, especially at higher wavenumbers. Most of the other theoretical works focus on this same aspect.

In this chapter, we do a linear stability analysis using an analytical and a numerical technique. The analytical model is an extension of the Eady (1949) model with a correction due to topography. The solution procedure involves an asymptotic expansion in the small parameter $\nu = S\delta/\epsilon$ in the limit as $\nu \rightarrow 0$, and S and ϵ are fixed. The numerical solution also incorporates the Eady model but we solve the problem by transforming the full set of equations to spectral space and then perform an eigenanalysis. Finally, we consider the topographic instability problem where the perturbation grows but does not propagate. We begin by reviewing the Eady model.

4.1 Eady Model

One of the simplest models of baroclinic instability was introduced by Eady (1949). In this model the north-south temperature gradient is simulated by the vertical shear of the horizontal wind through the thermal wind relationship. The vertical shear is taken to be linear. The flow is confined between two rigid boundaries at the top and bottom. The stratification and density are taken as constant. The streamfunction may be written as

$$\psi = -y\sigma\lambda + \varphi(x, y, \sigma, t), \quad (4.1.1)$$

where the first term on the right hand side represents the basic state and the second represents the perturbation. For this choice of basic state, $\Pi = 0$ and (3.5.2) reduces to

$$\left[\frac{\partial}{\partial t} + U^{T,B} \frac{\partial}{\partial x} \right] q = 0, \quad (4.1.2)$$

with boundary conditions

$$\left[\frac{\partial}{\partial t} + U^{T,B} \frac{\partial}{\partial x} \right] \left(\frac{\partial \phi}{\partial \sigma} \right) - \lambda \frac{\partial \phi}{\partial x} = 0, \quad (4.1.3)$$

where

$$U^T = - \frac{\partial \psi}{\partial y} = U_0 + \lambda,$$

$$U^B = - \frac{\partial \psi}{\partial y} = U_0,$$

and the superscript T is for the top boundary and B is for the bottom boundary. Solutions for (4.1.2) are of the form

$$\phi(x, y, \sigma, t) = F_0(\sigma) e^{i(Knx + lmy - \omega t)} + CC, \quad (4.1.4)$$

where CC denotes complex conjugate. Here, $F_0(\sigma)$ represents an undetermined function of the vertical coordinate, K is the fundamental zonal wavenumber, n is the zonal wavenumber, l is the fundamental meridional wavenumber, and m is the meridional wavenumber. We take $m = 1$ for the remainder of this section. Substituting (4.1.4) into (4.1.2), we find

$$(U^{T,B}Kn - \omega) \left[\frac{\partial^2 F_0}{\partial \sigma^2} - 4\mu_H^2 F_0 \right] = 0 \quad (4.1.5)$$

where

$$4\mu_H^2 = (K^2n^2 + l^2).$$

The boundary condition at $\sigma = +0.5$ is

$$(-\omega + KnU^T) \frac{\partial F}{\partial \sigma} - \lambda Kn = 0, \quad (4.1.6)$$

and the boundary condition at $\sigma = -0.5$

$$(-\omega + KnU^B) \frac{\partial F}{\partial \sigma} - \lambda Kn = 0. \quad (4.1.7)$$

A general set of discrete solutions to (4.1.5) is given by

$$F_0(\sigma) = A_n \cosh\left(2\mu_n\left(\sigma - \frac{1}{2}\right)\right) + B_n \sinh\left(2\mu_n\left(\sigma - \frac{1}{2}\right)\right) \quad (4.1.8)$$

Applying the boundary conditions, we obtain the following set of algebraic equations for A_n and B_n

$$\begin{bmatrix} -\lambda K_n & (-\omega + U^T K_n) 2\mu_n \\ (\lambda K_n + (-\omega + U^B K_n) 2\mu_n \tanh(2\mu_n)) & ((-\omega + U^B K_n) 2\mu_n + \lambda K_n \tanh(2\mu_n)) \end{bmatrix} \begin{bmatrix} A_n \\ B_n \end{bmatrix} = 0. \quad (4.1.9)$$

We can find nontrivial solutions for A_n and B_n if the determinant for the coefficients vanishes. Solving the determinant, we find the dispersion relation for the Eady model may be written as

$$\frac{\omega}{K_n} = U_0 + \frac{\lambda}{2} \pm \lambda \left[\frac{1}{4} - \frac{1}{2\mu_n} \left(\coth(2\mu_n) - \frac{1}{2\mu_n} \right) \right]^{\frac{1}{2}} \quad (4.1.10)$$

Figure 4.1 (a) shows a plot of growth rate versus wavenumber for S ranging from 0.1 - 0.4. For $S = 0.25$, the fastest growing mode is wavenumber six. Figure 4.1 (b) shows a plot of frequency versus wavenumber for S ranging from 0.1 - 0.4. As the stratification increases, the growth rate decreases and the frequency increases. For short waves, there are two neutral modes which have different frequencies. For long waves, beyond the shortwave cutoff, there are two roots which are complex conjugates. One of the roots is growing and the other is decaying. Only the growing root is shown in Figure 4.1 (a). These waves propagate with phase speed $(U_0 + \lambda/2)$.

The Burger number, S , relates the Rossby radius of deformation, L_D , to the length scale of the phenomena by

$$S = \left(\frac{L_D}{L} \right)^2. \quad (4.1.11)$$

As discussed by Pedlosky (1987), for $S = 0.25$, the dimensional wavelength is given by

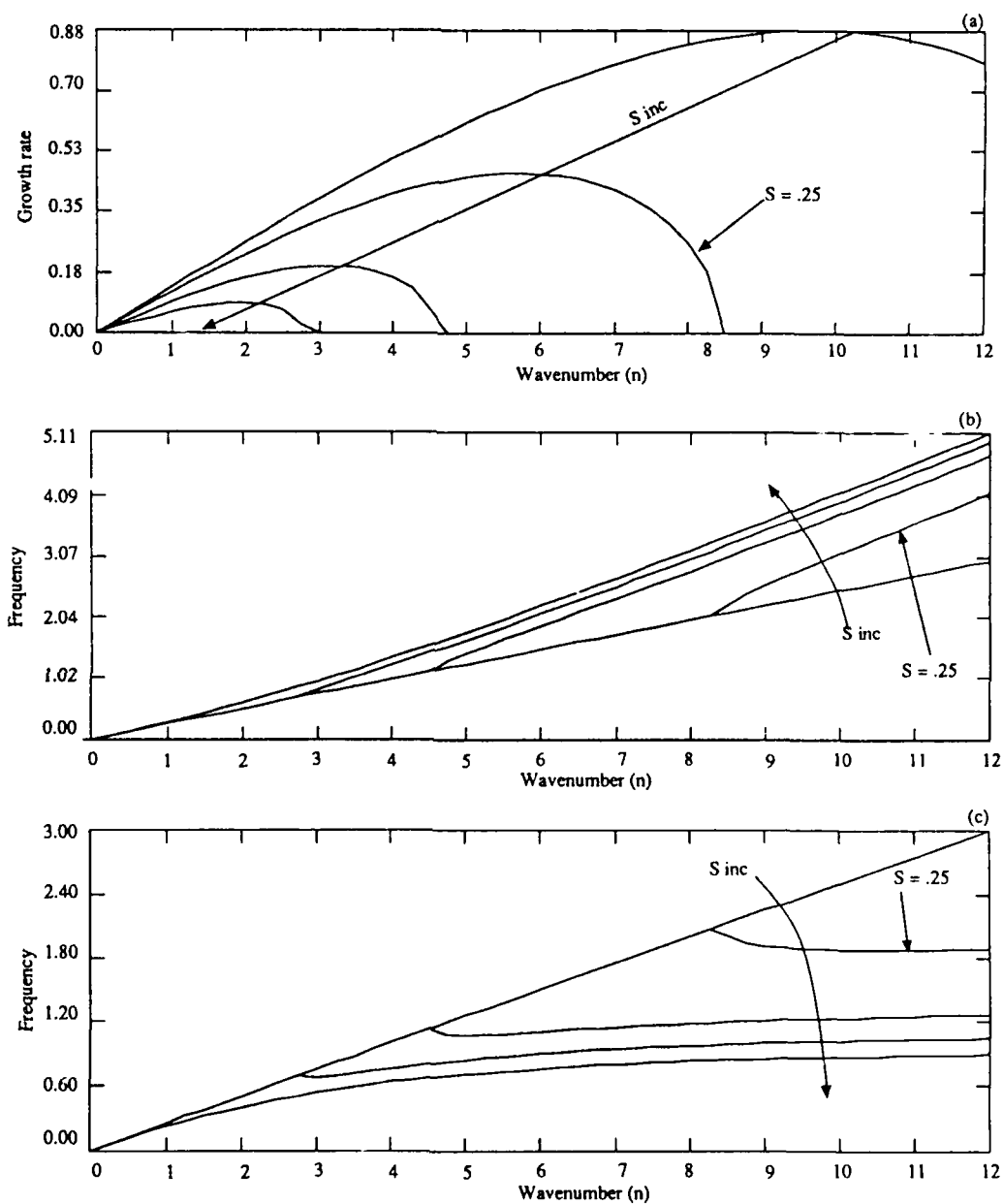


Figure 4.1 (a) Growth rate as a function of wavenumber for the Eady model. S ranges from 0.1 -0.4. $S = 0.25$ is labeled. (b) Frequency for the positive root in (4.1.10) and (c) for the negative root in (4.1.10) as a function of wavenumber for the same range of S . Arrows indicate the direction of increasing stratification.

$$\Lambda_* = \frac{2\pi L}{Kn} = \frac{4\pi L_D}{Kn} . \quad (4.1.12)$$

If we take L_D to be 10^3 km for the atmosphere, then (4.1.12) gives a wavelength of the order of 4000 km that will dominate the fluctuations in the atmosphere. This is in agreement with the observed synoptic scale disturbances.

Certain features of the Eady model are unrealistic and cannot be applied to the atmosphere although the model has been applied successfully to the annulus. The most important feature missing from the model is the planetary vorticity gradient. Charney and Stern (1962) proved there can be no growing disturbances in a basic flow unless the north-south gradient of basic state potential vorticity changes sign somewhere in the fluid. In the Eady model, the potential vorticity is constant throughout the fluid. Therefore, there is no north-south basic state potential vorticity gradient. However, Bretherton (1966) showed that the thermodynamic boundary conditions are equivalent to sheets of potential vorticity just above and below the fluid boundaries. Thus there are two infinitesimally thin sheets of potential vorticity within the fluid and so a basic state potential vorticity gradient exists. The gradients are equal in magnitude but opposite in sign at the top and bottom. Therefore, we need an upper boundary in the Eady model for baroclinic instability to develop.

4.2 Analytical Solutions and Results

In Section 4.1 we reviewed the Eady model. In this section we will use the Eady model to obtain an analytical solution for the problem with topography. We begin by substituting the wavy basic state we derived in Section 3.6 into (3.5.2) - (3.5.4). We find all of the terms involving the mountain are scaled by v . Next, we assume v is small so that we can rewrite the equations using an asymptotic expansion in the small parameter $v =$

($S\delta/\epsilon$). To leading order, $O(v^0)$, we find the problem is the Eady model. At the next order, $O(v^1)$, we bring in the correction due to the mountain. We chose the model to be periodic in x and y . There is a two-wave bottom topography and a rigid upper lid.

4.2.1 Problem Formulation

Substituting the wavy basic state into (3.5.2) gives

$$\frac{\partial q}{\partial t} + J(\Psi, q) = 0. \quad (4.2.1)$$

From (3.5.3), the boundary condition at $\sigma = +0.5$ becomes

$$\frac{\partial}{\partial t} \left(\frac{\partial \phi}{\partial \sigma} \right) + J \left(\Psi, \frac{\partial \phi}{\partial \sigma} \right) + J \left(\phi, \frac{\partial \Psi}{\partial \sigma} \right) = 0, \quad (4.2.2)$$

and from (3.5.4), the boundary condition at $\sigma = -0.5$ becomes

$$\frac{\partial}{\partial t} \left(\frac{\partial \phi}{\partial \sigma} \right) + J \left(\Psi, \frac{\partial \phi}{\partial \sigma} \right) + J \left(\phi, \frac{\partial \Psi}{\partial \sigma} + v\eta \right) = 0. \quad (4.2.3)$$

If for simplicity, we take $q = 0$ at time $t = 0$, then $q = 0$ for all time and (4.2.1) becomes

$$q = \left(\nabla^2 + \frac{1}{S} \frac{\partial^2}{\partial \sigma^2} \right) \phi = 0. \quad (4.2.4)$$

Substituting (3.6.10) into (4.2.2) and (4.2.3), we can rewrite the boundary conditions as

$$\left[\frac{\partial}{\partial t} + U^T, B \frac{\partial}{\partial x} \right] \left(\frac{\partial \phi}{\partial \sigma} \right) - \lambda \frac{\partial \phi}{\partial x} - v(i/2K \sin(2Kx)) \left[\underset{(a)}{F_B} \underset{(b)}{\frac{\partial}{\partial \sigma}} - \underset{(c)}{\frac{\partial F_B}{\partial \sigma}} + \left(\sigma - \frac{1}{2} \right) \right] \phi = 0. \quad (4.2.5)$$

where $U^T = (U_0 + \lambda)$ and $U^B = U_0$. In (4.2.5), (a) is the basic state meridional advection of the meridional perturbation temperature gradient, (b) is the zonal perturbation advection of the zonal basic state temperature gradient, and (c) is the zonal perturbation flowing over the mountain slope. Recall that the expression for F_B is given by

$$F_B(\sigma) = A_B \cosh \left(\gamma \left(\sigma - \frac{1}{2} \right) \right) + B_B \sinh \left(\gamma \left(\sigma - \frac{1}{2} \right) \right) \quad (3.6.7)$$

and A_B and B_B are given by (3.6.8) and (3.6.9). If we assume solutions of the form

$$\varphi(x, y, \sigma, t) = \chi(x, \sigma) e^{i(l y - \omega t)} + CC, \quad (4.2.6)$$

(4.2.4) may be written as

$$\left(\frac{\partial^2}{\partial x^2} - l^2 + \frac{1}{S} \frac{\partial^2}{\partial \sigma^2} \right) \chi = 0, \quad (4.2.7)$$

and (4.2.5) may be written as

$$\left[-i\omega + U^T, B \frac{\partial}{\partial x} \right] \left(\frac{\partial \chi}{\partial \sigma} \right) - \lambda \frac{\partial \chi}{\partial x} - \nu (i/2 K \sin(2Kx)) \left[F_B \frac{\partial}{\partial \sigma} - \frac{\partial F_B}{\partial \sigma} + \left(\sigma - \frac{1}{2} \right) \right] \chi = 0. \quad (4.2.8)$$

4.2.2 Asymptotic Expansions In Orders of ν

We assume that we can rewrite the variables of (4.2.7) and (4.2.8) in terms of the small parameter $\nu = (S\delta/\epsilon)$ such that

$$\chi = \chi_0 + \nu^1 \chi_1 + \dots,$$

and

$$\omega = \omega_0 + \nu^1 \omega_1 + \dots \quad (4.2.9)$$

We can substitute (4.2.9) into (4.2.7) and (4.2.8) and collect terms by order. The $O(\nu^0)$ problem becomes

$$\left(\frac{\partial^2}{\partial x^2} - l^2 \right) \chi_0 + \frac{1}{S} \frac{\partial^2 \chi_0}{\partial \sigma^2} = 0 \quad (4.2.10)$$

and

$$\left[-i\omega_0 + U^T, B \frac{\partial}{\partial x} \right] \left(\frac{\partial \chi_0}{\partial \sigma} \right) - \lambda \frac{\partial \chi_0}{\partial x} = 0. \quad (4.2.11)$$

We find the $O(\nu^1)$ problem to be

$$\left(\frac{\partial^2}{\partial x^2} - l^2 \right) \chi_1 + \frac{1}{S} \frac{\partial^2 \chi_1}{\partial \sigma^2} = 0 \quad (4.2.12)$$

and

$$\left[-i\omega_0 + U^{T,B} \frac{\partial}{\partial x} \right] \left(\frac{\partial \chi_1}{\partial \sigma} \right) - \lambda \frac{\partial \zeta_1}{\partial x} - i\omega_1 \frac{\partial \chi_0}{\partial \sigma} - (i/2K \sin(2Kx)) \left[F_B \frac{\partial}{\partial \sigma} - \frac{\partial F_B}{\partial \sigma} + \left(\sigma - \frac{1}{2} \right) \right] \chi_0 = 0. \quad (4.2.13)$$

The leading order problem is the Eady problem that was solved in Section 4.1. For this problem, we assume solutions of the form

$$\chi_0 = F_0(\sigma) e^{iKnx} + CC \quad (4.2.14)$$

and substitute into (4.2.10) and (4.2.11) to obtain the Eady dispersion relation given by (4.1.10). The growth rates and frequencies are shown in Figure 4.1.

The $O(v^1)$ equations also involve leading order quantities. Therefore, we substitute the leading order solution, (4.2.14) into (4.2.13) and obtain

$$\left[-i\omega_0 + U^{T,B} \frac{\partial}{\partial x} \right] \left(\frac{\partial \chi_1}{\partial \sigma} \right) - \lambda \frac{\partial \chi_1}{\partial x} = i\omega_1 \frac{\partial F_0}{\partial \sigma} e^{iKnx} + (iK) (e^{iK(n+2)x} - e^{iK(n-2)x}) G^{T,B}, \quad (4.2.15)$$

where

$$G^T = \left[F_B \frac{\partial}{\partial \sigma} - \frac{\partial F_B}{\partial \sigma} \right] F_0, \quad (4.2.16)$$

(a) (b) (c)

and

$$G^B = \left[F_B \frac{\partial}{\partial \sigma} - \frac{\partial F_B}{\partial \sigma} - 1 \right] F_0. \quad (4.2.17)$$

(a) (b) (c) (d)

Figure 4.2 and 4.3 show the real and imaginary parts of (4.2.16) and (4.2.17) as a function of wavenumber for $U_0 = -0.5$ (solid), $U_0 = 0.1$ (long dashed), and $U_0 = 0.5$ (short dashed). Figure 4.2 (a) represents G^T , (b) represents term (b), and (c) represents term (c) in (4.2.16). Figure 4.3 (a) represents G^B , (b) represents term (b), (c) is term (c), and (d) is term (d) in (4.2.17). Comparison of Figures 4.2 and 4.3 shows that overall, G^B is larger in magnitude than G^T and the contribution from each of the terms (b), (c), and (d)

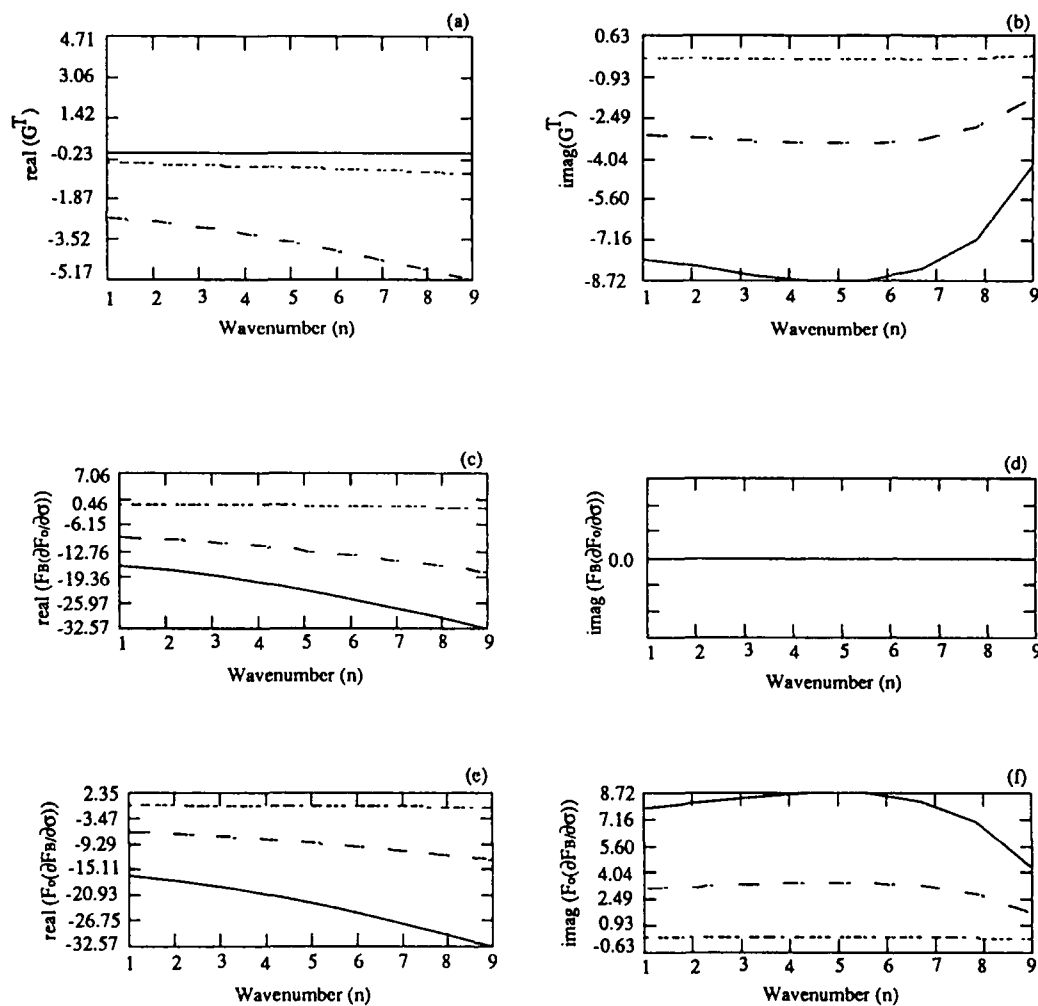


Figure 4.2 Plot of (4.2.16) where (a) is the real and (b) is the imaginary contribution to the term G^T , (c) is the real and (d) is the imaginary contribution to G^T from $F_B(\partial F_B/\partial \sigma)$, and (e) is the real and (f) is the imaginary contribution to G^T from $F_O(\partial F_B/\partial \sigma)$ as a function of wavenumber. The solid line is for $U_0 = -0.5$, long dashed is for $U_0 = 0.1$, and the short dashed is for $U_0 = 0.5$.

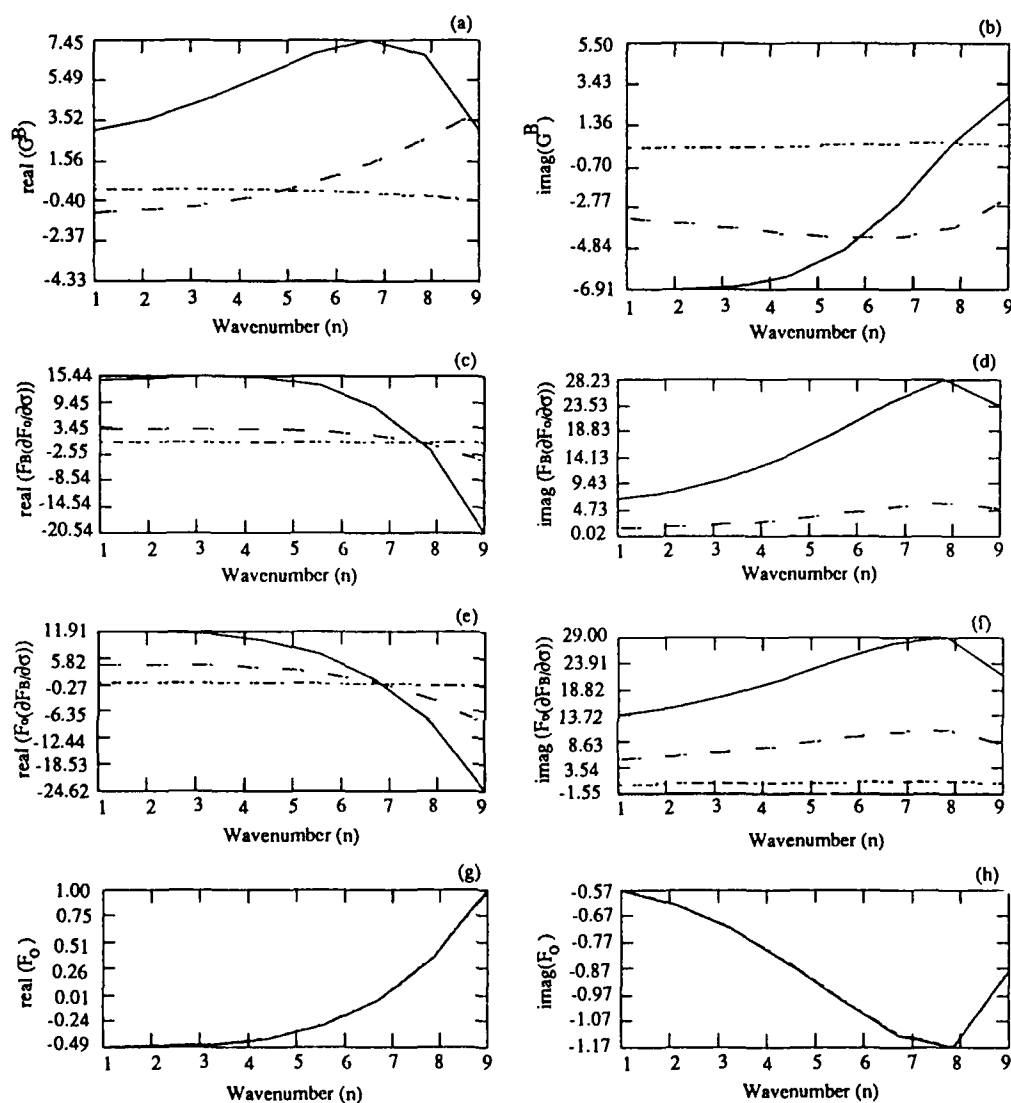


Figure 4.3 Plot of (4.2.17) where (a) is the real and (b) is the imaginary contribution to the term G^B , (c) is the real and (d) is the imaginary contribution to G^B from $F_B(\partial F_O/\partial \sigma)$, (e) is the real and (f) is the imaginary contribution to G^B from $F_O(\partial F_B/\partial \sigma)$, and (g) is the real and (h) is the imaginary contribution to G^B from F_O as a function of wavenumber. The solid line is for $U_0 = -0.5$, long dashed is for $U_0 = 0.1$, and the short dashed is for $U_0 = 0.1$.

is larger at the bottom. Figure 4.3 (g) and (h) shows that the contribution due to the perturbation flowing over the mountain is small compared the contributions from the other terms.

The two terms on the right hand side of (4.2.15) involve the three wavenumbers n , $n+2$, and $n-2$ which represent the forcing of $O(v^1)$ by $O(v^0)$. Therefore, we expect χ_1 to be forced by three terms proportional to these wavenumbers. We will assume solutions for χ_1 of the form

$$\chi_1 = \chi_{1,n} e^{iKn x} + \chi_{1,n+2} e^{iK(n+2)x} + \chi_{1,n-2} e^{iK(n-2)x} + CC. \quad (4.2.18)$$

Substituting (4.2.18) into (4.2.15) and projecting the equation onto the modes n , $n+2$, and $n-2$, we obtain three sets of equations for $O(v^1)$. The equations are for mode n

$$\left[\frac{\partial^2}{\partial \sigma^2} - S((Kn)^2 + l^2) \right] (\chi_{1,n}) = 0, \quad (4.2.19)$$

$$[-\omega_0 + UT, BK_n] \left(\frac{\partial \chi_{1,n}}{\partial \sigma} \right) - Kn \lambda \chi_{1,n} = \omega_1 \frac{\partial F_0}{\partial \sigma}, \quad (4.2.20)$$

and for mode $n+2$

$$\left[\frac{\partial^2}{\partial \sigma^2} - S((K(n+2))^2 + l^2) \right] (\chi_{1,n+2}) = 0, \quad (4.2.21)$$

$$[-\omega_0 + UT, BK(n+2)] \left(\frac{\partial \chi_{1,n+2}}{\partial \sigma} \right) - \lambda K(n+2) \chi_{1,n+2} + i/KG T, B = 0, \quad (4.2.22)$$

and for mode $n-2$

$$\left[\frac{\partial^2}{\partial \sigma^2} - S((K(n-2))^2 + l^2) \right] (\chi_{1,n-2}) = 0, \quad (4.2.23)$$

$$[-\omega_0 + UT, BK(n-2)] \left(\frac{\partial \chi_{1,n-2}}{\partial \sigma} \right) - \lambda K(n-2) \chi_{1,n-2} + i/KGT, B = 0. \quad (4.2.24)$$

At $O(v^1)$, ω_1 enters the problem in (4.2.20) only. To evaluate ω_1 , we combine (4.2.20), (4.2.19) and the $O(v^0)$ thermodynamic boundary condition, (4.2.11) and its solution. We find ω_1 must equal zero which implies that by proper gauging, we can choose $\chi_{1n} = 0$. As a consequence of $\omega_1 = 0$, the $O(v^1)$ problem will result in a correction to the modal structure for the $O(v^0)$ problem. To get a correction to the frequency, ω_0 , we must solve the $O(v^2)$ problem and find ω_2 . Therefore, we cannot infer anything about the group velocity from these two orders of the problem.

We have separated the problem into $O(v^0)$ and $O(v^1)$. After solving the leading order Eady problem, we could choose some wavenumber n . That wavenumber might be in the neutral or unstable region shown in Figure 4.1. If n is in the unstable region, it will have growth rate $\text{imaginary}(\omega_0)$ shown in Figure 4.1 (a) and propagate at frequency $\text{real}(\omega_0)$ shown in Figure 4.1 (b). If n is in the stable region, there will be two waves that move at frequency $\omega_0^{+,-}$ shown in Figure 4.1 (b) and (c) depending on the sign we choose in front of the radical in (4.1.10).

We found that only ω_0 enters the $O(v^1)$ correction to the Eady problem. Therefore, the modes $n+2$ and $n-2$ will propagate and grow as n . If the wavenumber n is in the unstable region shown in Figure 4.1, $n+2$ and $n-2$ will propagate at $\text{real}(\omega_0)$ and have growth rate $\text{imaginary}(\omega_0)$. If the wavenumber n is in the stable region, $n+2$ and $n-2$ will propagate with frequency $\omega_0^{+,-}$ depending on the sign we choose in (4.1.10).

We solved the $O(v^1)$ problem following the same procedure as in Section 4.1 for the Eady model. Equations (4.2.19), (4.2.21), and (4.2.23) have solutions of the form

$$\chi_{n,n\pm 2}(\sigma) = A_{n,n\pm 2} \cosh \left(2\mu_{n,n\pm 2} \left(\sigma - \frac{1}{2} \right) \right) + B_{n,n\pm 2} \sinh \left(2\mu_{n,n\pm 2} \left(\sigma - \frac{1}{2} \right) \right). \quad (4.2.25)$$

The thermodynamic equations at the upper and lower boundaries, (4.2.20), (4.2.22), and (4.2.24) were applied. Since $\omega_1 = 0$, we can solve for the coefficients A_n and B_n immediately because (4.2.19) and (4.2.20) represent the Eady model which we already solved in Section 4.1. Next, we wrote a system of algebraic equations for the unknown coefficients $A_{n\pm 2}$ and $B_{n\pm 2}$ and solved the system using a numerical technique. After we found the coefficients, we reconstructed $\chi_{1,n\pm 2}$ and finally the full streamfunction.

Figure 4.4 shows the amplitudes of the coefficients χ_0 , $\chi_{1,n+2}$, and $\chi_{1,n-2}$, at the (a) lower and (b) upper boundaries. For this case, we chose the Burger number, $S = 0.25$ and the most unstable mode is wavenumber six. At the $O(v^1)$, the modes four and eight enter the problem. The magnitude of the coefficients are larger at the lower boundary. We will compare this figure to results from the numerical solution in Section 4.3.

Figure 4.5 shows x - σ contours of the perturbation streamfunction down the center of the channel. Figure 4.5 (a) shows the full streamfunction which is the same of the leading order streamfunction plus the correction due to topography. Figure 4.5 (b) is the streamfunction for the leading order Eady problem. We chose the stratification, $S = 0.25$ and the fastest growing mode is wavenumber six. To find the correction to the Eady model, we chose $v = 0.25$. Since $S = 0.25$, the ratio of mountain height to Rossby number is one. These are good choices to remain within the quasi-geostrophic approximation. Figure 4.5 (c) and (d) show the correction due to wavenumber eight and wave number four. All three modes have the same growth rate and frequency.

4.3 Numerical Solution

In this section we use a numerical technique to solve the topography problem. First,

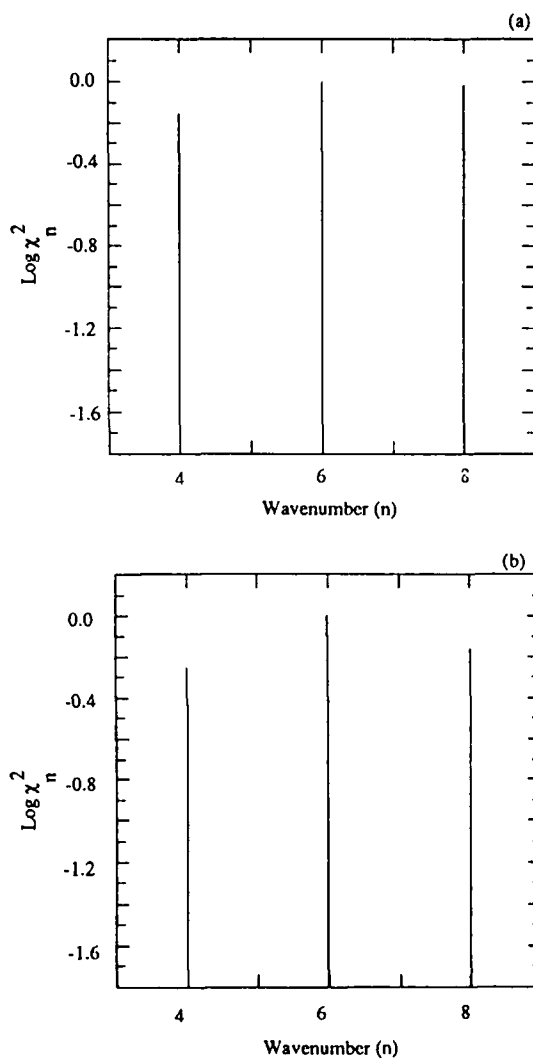


Figure 4.4 The magnitude of the coefficients in (4.2.14) and (4.2.18) for (a) the lower and (b) the upper boundary for the case of $n = 6$, $n + 2 = 8$, and $n - 2 = 4$. Here, $U_0 = 0.1$, $\epsilon = 0.1$, and $\lambda = 1.0$.

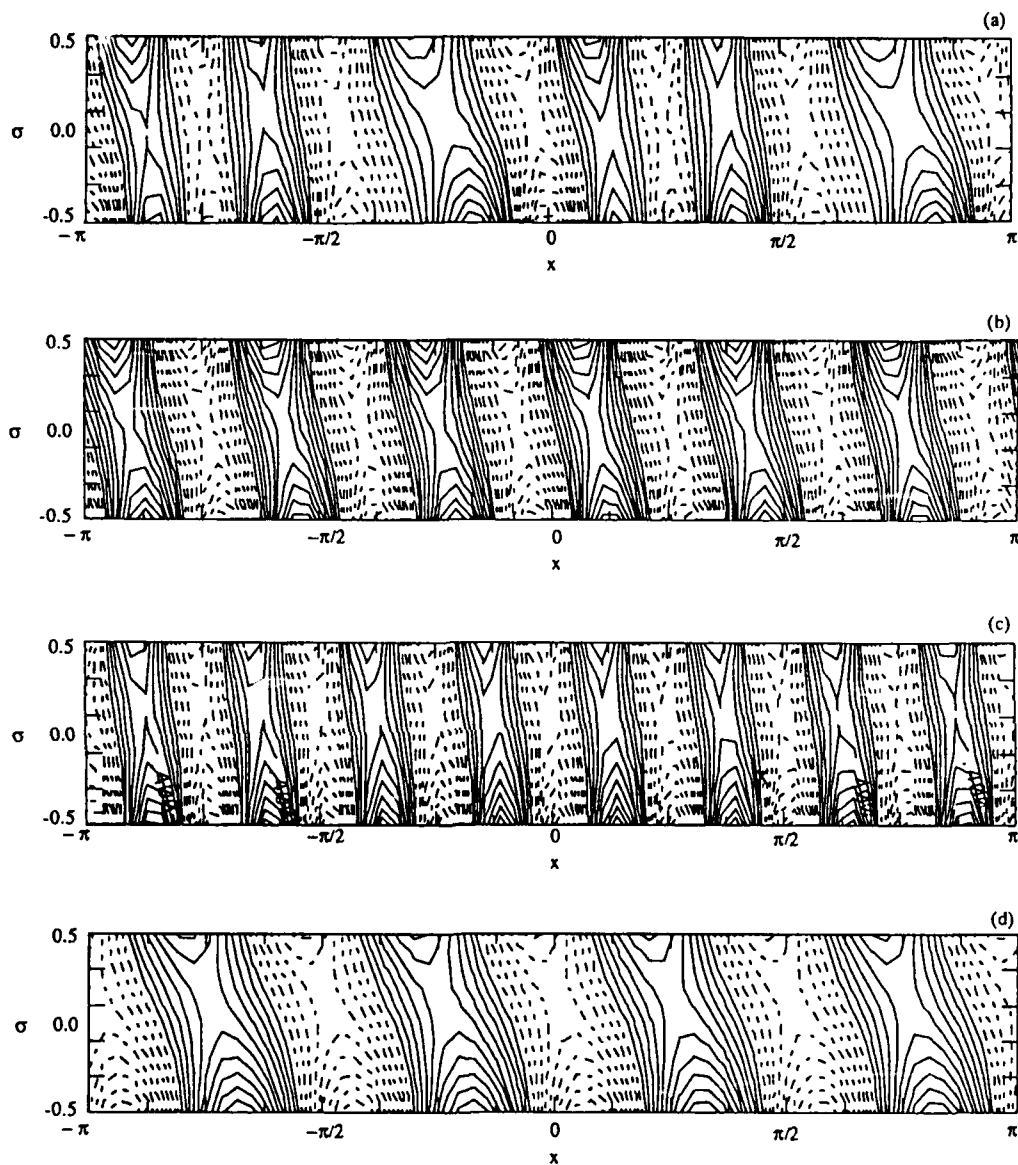


Figure 4.5 X- σ cross sections at mid-radius for the perturbation streamfunction for (a) the sum of the most unstable mode from the Eady model, wavenumber 6, plus corrections due to topography from wavenumbers 4 and 8. (b) Most unstable Eady mode, wavenumber six, (c) wavenumber 8, and (d) wavenumber 4. $S = 0.25$, $U_0 = 0.0$, and $\lambda = 1.0$. Topographic ridges at 0.0 and π rad.

we cast the equations in spectral form. Next, we manipulate the equations to set up an eigenvalue, eigenvector problem and solve the problem using numerical routines. The eigenvalues give us the growth rates and frequencies and the eigenvector will be used to reconstruct the streamfunction. Finally, we consider the topographic instability problem.

In Section 4.2, we showed the quasi-geostrophic potential vorticity equation in sigma coordinates with a wavy basic state to be

$$\frac{\partial q}{\partial t} + J(\Psi, q) = 0, \quad (4.2.1)$$

with the boundary condition at $\sigma = 0.5$

$$\frac{\partial}{\partial t} \left(\frac{\partial \varphi}{\partial \sigma} \right) + J \left(\Psi, \frac{\partial \varphi}{\partial \sigma} \right) + J \left(\varphi, \frac{\partial \Psi}{\partial \sigma} \right) = 0, \quad (4.2.2)$$

and the boundary condition at $\sigma = -0.5$

$$\frac{\partial}{\partial t} \left(\frac{\partial \varphi}{\partial \sigma} \right) + J \left(\Psi, \frac{\partial \varphi}{\partial \sigma} \right) + J \left(\varphi, \frac{\partial \Psi}{\partial \sigma} + v\eta \right) = 0, \quad (4.2.3)$$

where

$$\Psi(x, y, \sigma, t) = -y \left(U_0 + \lambda \left(\sigma + \frac{1}{2} \right) \right) + v F_B(\sigma) \cos(2Kx), \quad (4.3.1)$$

and $v = (S\delta/\epsilon)$. In the model, there is a rigid upper lid and $\cos(2Kx)$ bottom topography. We take the model to be periodic in the x and y directions. We chose y to be periodic to avoid the difficult problem of the intersection of the side wall with the topography. In this problem, we are interested in the phenomena in the center of the channel, far from the walls. We assume solutions to the full equations of the form

$$\begin{aligned} \varphi(x, y, \sigma, t) = -u'(t)y + & \sum_{m=0}^M \sum_{n=0}^N \left[\varphi_{mn}^s(t, \sigma) e^{iKnx} + \varphi_{mn}^{*s}(t, \sigma) e^{-iKnx} \right] \sin(m/y) + \\ & \sum_{m=0}^M \sum_{n=0}^N \left[\varphi_{mn}^c(t, \sigma) e^{iKnx} + \varphi_{mn}^{*c}(t, \sigma) e^{-iKnx} \right] \cos(m/y). \end{aligned} \quad (4.3.2)$$

In (4.3.2), * represents the complex conjugate. $u'(t)$ represents a volumetrically averaged, time dependent, zonal velocity. It becomes important when we consider the interaction of the zonal flow with topography through the form-drag equation. We represent periodicity in y using a $\sin(m/y)$ and $\cos(m/y)$ rather than $\exp(im/y)$ to prevent wave propagation in the north-south direction. In (4.3.2) the amplitudes are functions of time and the vertical coordinate.

As in the Eady model, if we take $q = 0$ at time $t = 0$, then q remains zero for all time and (4.2.1) becomes

$$q = \nabla^2 \phi + \frac{1}{S} \frac{\partial^2 \phi}{\partial \sigma^2} = 0. \quad (4.3.3)$$

Substituting (4.3.2) into (4.3.3), the discrete solutions are of the form

$$\phi_{mn}^s(\sigma) = A_{mn}^s(t) \cosh(2\mu_{mn}\sigma) + B_{mn}^s(t) \sinh(2\mu_{mn}\sigma) + CC \quad (4.3.4)$$

and

$$\phi_{mn}^c(\sigma) = A_{mn}^c(t) \cosh(2\mu_{mn}\sigma) + B_{mn}^c(t) \sinh(2\mu_{mn}\sigma) + CC \quad (4.3.5)$$

where

$$\mu_{mn} = \frac{1}{2} \left(S((Kn)^2 + (lm)^2) \right)^{\frac{1}{2}}. \quad (4.3.6)$$

Next, we substitute the assumed solution, (4.3.2), into the thermodynamic boundary conditions (4.2.2) and (4.2.3) and obtain expressions involving summations of zonal and meridional wavenumbers. To separate the equations into individual zonal and meridional components, we project the equations onto orthogonal basis functions. We take the sine and cosine as the meridional basis functions and project on an arbitrary wavenumber r . We take an exponential function as the zonal basis function and project on an arbitrary wavenumber q . Projecting on the sine and cosine in the meridional direction will produce

two sets of equations. After some algebraic manipulation, the boundary conditions in spectral form for the cosine projection may be written

$$\begin{aligned} & \frac{\partial}{\partial t} \left(\frac{\partial \varphi_{qr}^{c+}}{\partial \sigma} \right) + (ivKrI)(\Psi^+) \frac{\partial}{\partial \sigma} [\varphi_{q-2,r}^{s+} - \varphi_{q+2,r}^{s+} + \varphi_{2-q,r}^{*s+}] + \\ & (U_0 + \lambda)(iKq) \frac{\partial \varphi_{qr}^{c+}}{\partial \sigma} - (\lambda iKq) \varphi_{qr}^{c+} - (ivKrI) \left(\frac{\partial \Psi^+}{\partial \sigma} \right) [\varphi_{q-2,r}^{s+} - \varphi_{q+2,r}^{s+} + \varphi_{2-q,r}^{*s+}] = 0, \end{aligned} \quad (4.3.7)$$

at $\sigma = 0.5$ and

$$\begin{aligned} & \frac{\partial}{\partial t} \left(\frac{\partial \varphi_{qr}^{c-}}{\partial \sigma} \right) + (ivKrI)(\Psi^-) \frac{\partial}{\partial \sigma} [\varphi_{q-2,r}^{s-} - \varphi_{q+2,r}^{s-} + \varphi_{2-q,r}^{*s-}] + \\ & U_0(iKq) \frac{\partial \varphi_{qr}^{c-}}{\partial \sigma} - (\lambda iKq) \varphi_{qr}^{c-} - (ivKrI) \left(\frac{\partial \Psi^-}{\partial \sigma} + 1 \right) [\varphi_{q-2,r}^{s-} - \varphi_{q+2,r}^{s-} + \varphi_{2-q,r}^{*s-}] = 0, \end{aligned} \quad (4.3.8)$$

at $\sigma = -0.5$. A similar set of equations can be written for the sine component. Here, the superscripts + and - indicate the quantities should be evaluated at the upper or lower boundary. There are two complex conjugate pairs with the superscript s in (4.3.7) and (4.3.8). The complex conjugate becomes important when we consider zonal wavenumbers zero, one, and two.

There are many interesting points to be made about these equations and the same things can be said for the sine component. The equations are decoupled in the meridional direction which means an independent set of equations can be written for each meridional wavenumber. The equations are coupled in the zonal direction by $q \pm 2$ due to interaction of the perturbation with the wavenumber two of the topography and the forced basic state.

The equations for the cosine projection involve sine and cosine coefficients. The sine coefficients enter because we took y-derivatives in the original equation. The second and fifth terms in (4.3.7) and (4.3.8) have the sine coefficients. The second term in both equations represents the basic state advection of perturbation temperature with wavenumber $q \pm 2$. The fifth term in both equations represents advection by perturbation wavenumber

$q \pm 2$ of the basic state temperature. Also, the fifth term in the lower boundary condition, (4.3.8), represents perturbation advection of wavenumber $q \pm 2$ along the slope of the topography. The magnitudes of each of these terms is controlled by the ratio $v = (S\delta/\epsilon)$. Thus the stratification, mountain height, and rotational effects will all play a role in determining how important the wavy basic state and the mountain are in this problem. The third and fourth terms in (4.3.7) and (4.3.8) represent the Eady model. In the absence of topography and wavy basic state, this model reduces to the Eady model.

To solve these equations, we substitute for ϕ_{qr} in (4.3.7) and (4.3.8) using (4.3.4) and (4.3.5). Next we add and subtract the upper and lower boundary conditions. This step allows us to solve for the time derivatives in (4.3.7) and (4.3.8). Finally, after considerable algebra, we derive the following dynamical system of equations for the unknown coefficients

$$\begin{aligned}
 \dot{A}_q^s + i \left[ac1(A_{q-2,r}^c + A_{q-2,r}^{*c}) + ac2A_{q+2,r}^c + as5A_{q,r}^s + bs5B_{q,r}^s + bc1(B_{q-2,r}^c + B_{q-2,r}^{*c}) + bc2B_{q+2,r}^c \right] &= 0, \\
 \dot{B}_q^s + i \left[ac3(A_{q-2,r}^c + A_{q-2,r}^{*c}) + ac4A_{q+2,r}^c + as6A_{q,r}^s + bs6B_{q,r}^s + bc3(B_{q-2,r}^c + B_{q-2,r}^{*c}) + bc4B_{q+2,r}^c \right] &= 0, \\
 \dot{A}_q^c + i \left[as1(A_{q-2,r}^s + A_{q-2,r}^{*s}) + as2A_{q+2,r}^s + ac5A_{q,r}^c + bc5B_{q,r}^c + bs1(B_{q-2,r}^s + B_{q-2,r}^{*s}) + bs2B_{q+2,r}^s \right] &= 0, \\
 \dot{B}_q^c + i \left[as3(A_{q-2,r}^s + A_{q-2,r}^{*s}) + as4A_{q+2,r}^s + ac6A_{q,r}^c + bc6B_{q,r}^c + bs3(B_{q-2,r}^s + B_{q-2,r}^{*s}) + bs4B_{q+2,r}^s \right] &= 0.
 \end{aligned}
 \tag{4.3.9}$$

All of the coefficients written in italics are listed in Appendix B.

The system represents a set of complex, linear, ordinary differential equations and can be written as

$$\frac{\partial \vec{\Theta}}{\partial t} = \mathbf{A} \vec{\Theta},
 \tag{4.3.10}$$

where $\vec{\Theta}$ is a vector containing the Fourier coefficients and \mathbf{A} is a square coefficient matrix.

Since this is a linear system, we can assume $\exp(i\omega t)$ time dependence and transform the

system to the eigenvalue, eigenvector problem,

$$\vec{\omega}\vec{\Theta} = \vec{A}\vec{\Theta}. \quad (4.3.11)$$

The eigenvalue, ω , and the eigenvector are computed using IMSL library routines. In this problem, $\text{real}(\omega)$ represents the growth rate and $\text{imaginary}(\omega)$ represents the frequency.

Associated with each eigenvalue is an eigenvector that will be used to reconstruct the streamfunction using an inverse Fourier transform routine.

We truncated the system at zonal wavenumber twelve and took the meridional wavenumber to be one. We expect the largest growth rates at approximately wavenumber six and since wave six interacts with waves eight and four, we should include at least through wavenumber eight. However, Niehaus (1980) showed that growth rates continued to change as the truncation level was increased until twelve or more waves were added to the model. Wavenumbers greater than twelve were neglected. Wavenumbers zero, one, and two were treated as special cases. Wavenumber zero, the zonal mean, and one interact with the complex conjugate of wavenumbers two and one. Wavenumber two interacts with the mean zonal flow.

Figure 4.6 (a) is a plot of contours of growth rate for the fastest growing mode and (b) is a plot of contours of frequency as the stratification and mountain height are varied. When the mountain height is zero, the ordinate gives the growth rates of the Eady model, and Figure 4.6 (a) shows that as the stratification increases, the growth rate decreases. As the mountain height increases, the growth rates decrease slightly for large values of stratification but are nearly constant for small values of stratification. Figure 4.6 (b) shows that the frequency remains nearly constant until larger mountain heights and then the frequency begins to increase. In Figure 4.6, $\epsilon = 0.1$, $U_0 = 0.1$, and $\lambda = 1.0$. When $U_0 = -0.1$, a plot similar to Figure 4.6 shows that the growth rate and frequency remain nearly

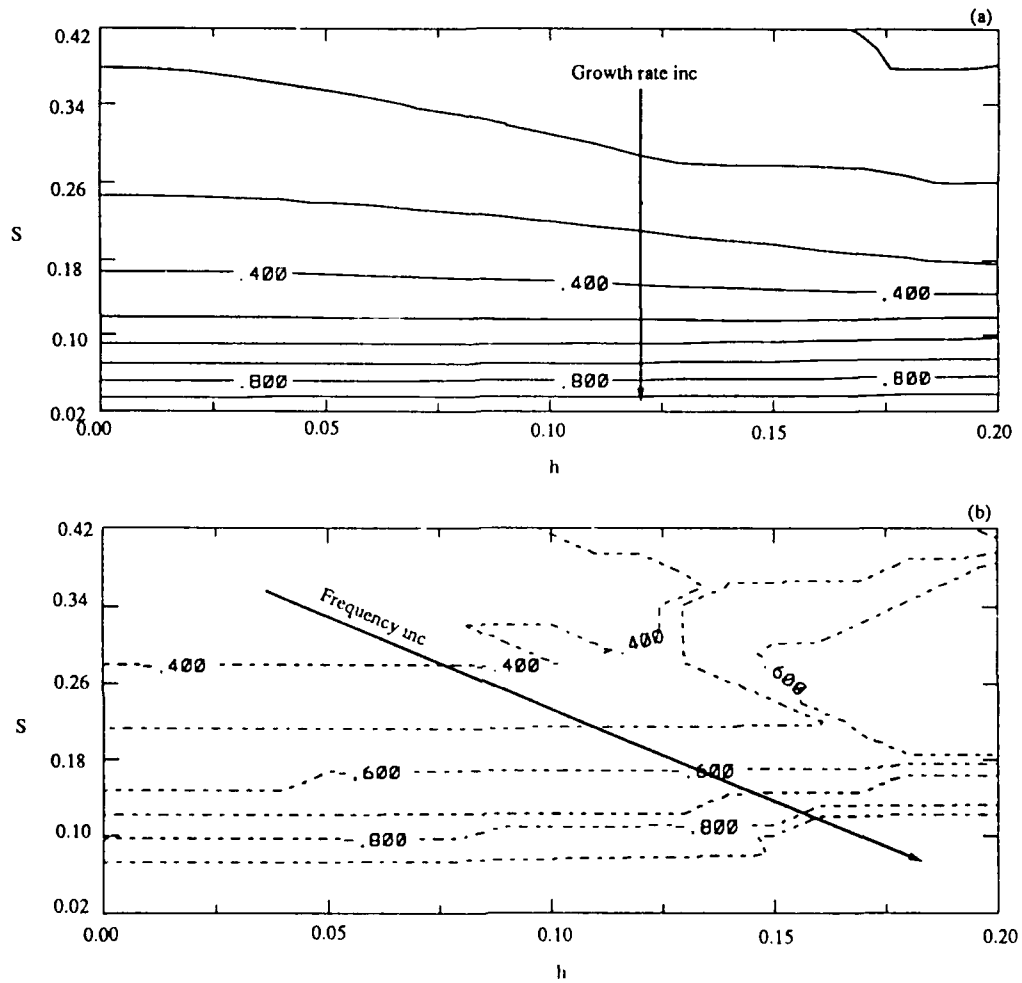


Figure 4.6 Contours of (a) growth rate and (b) frequency for the most unstable mode as a function stratification, S , and mountain height, h . Arrows indicate the direction of increasing values of growth rate or frequency. $U_0 = 0.1$, $\lambda = 1.0$, and $\epsilon = 0.1$.

constant for all mountain heights and stratification. For all of the remaining figures, the vertical shear, $\lambda = 1.0$.

Figure 4.7 (a) is a plot of contours of growth rate for the fastest growing mode and (b) is contours of frequency as the stratification and U_0 are varied. U_0 varies on the abscissa. The mountain height and Rossby number are fixed at 0.1. Figure 4.7 (a) shows the growth rate of the most unstable modes is nearly constant for $U_0 > -0.1$. As U_0 approaches -0.5, the growth rate becomes extremely large. Figure 4.7 (b) shows the frequency increases as U_0 increases but decreases as the stratification increases. As U_0 approaches -0.5, the frequency of the mode becomes zero. This happens since the phase speed of propagation is equal and opposite to U_0 . Although this mode is growing but has no frequency, it should not be considered a form of topographic instability since the form drag mechanism was not considered. Surface easterly flows of such magnitude are not observed in the atmosphere or the annulus so this flow is probably not physically realizable. As the mountain height was increased, plots similar to Figure 4.6 showed nearly the same growth rates for positive U_0 but growth rate becomes enormous for all negative values of U_0 .

We wanted to investigate the effect of the mountain height on the basic state and perturbation. We fixed $S = 0.25$ and $\epsilon = 0.1$. Figure 4.8 shows x-y and x- σ cross sections of the basic state and perturbation stream function. Figure 4.8 (a) and (b) show that for very small mountain heights, the basic state flow at the bottom and top is nearly zonal. When the x-dependent part is added to the zonal flow, only a linear vertical shear is apparent in Figure 4.8 (c). Figure 4.8 (d) is the x- σ cross section of the x-dependent part of the basic state shows a high over the topography at 0 and π rad. Figure 4.8 (e) and (f) show the perturbation streamfunction at the bottom and top for the same small mountain. The perturbations line up zonally much as is observed in an Eady model which is periodic

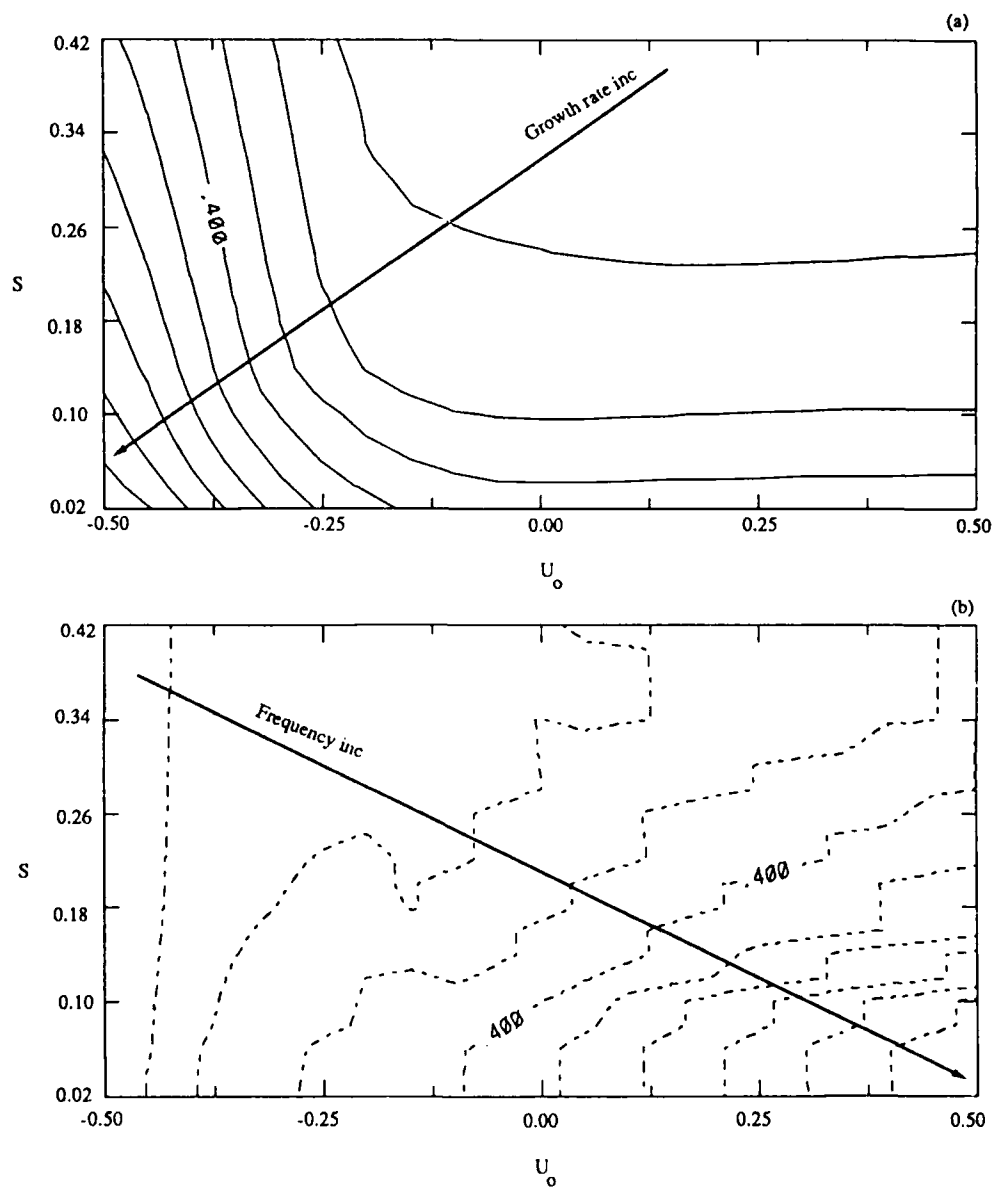


Figure 4.7 Contours of (a) growth rate and (b) frequency for the most unstable mode as a function of S and U_0 . Arrow indicates the direction of increasing values. $\delta = 0.1$, $\lambda = 1.0$, and $\epsilon = 0.1$.

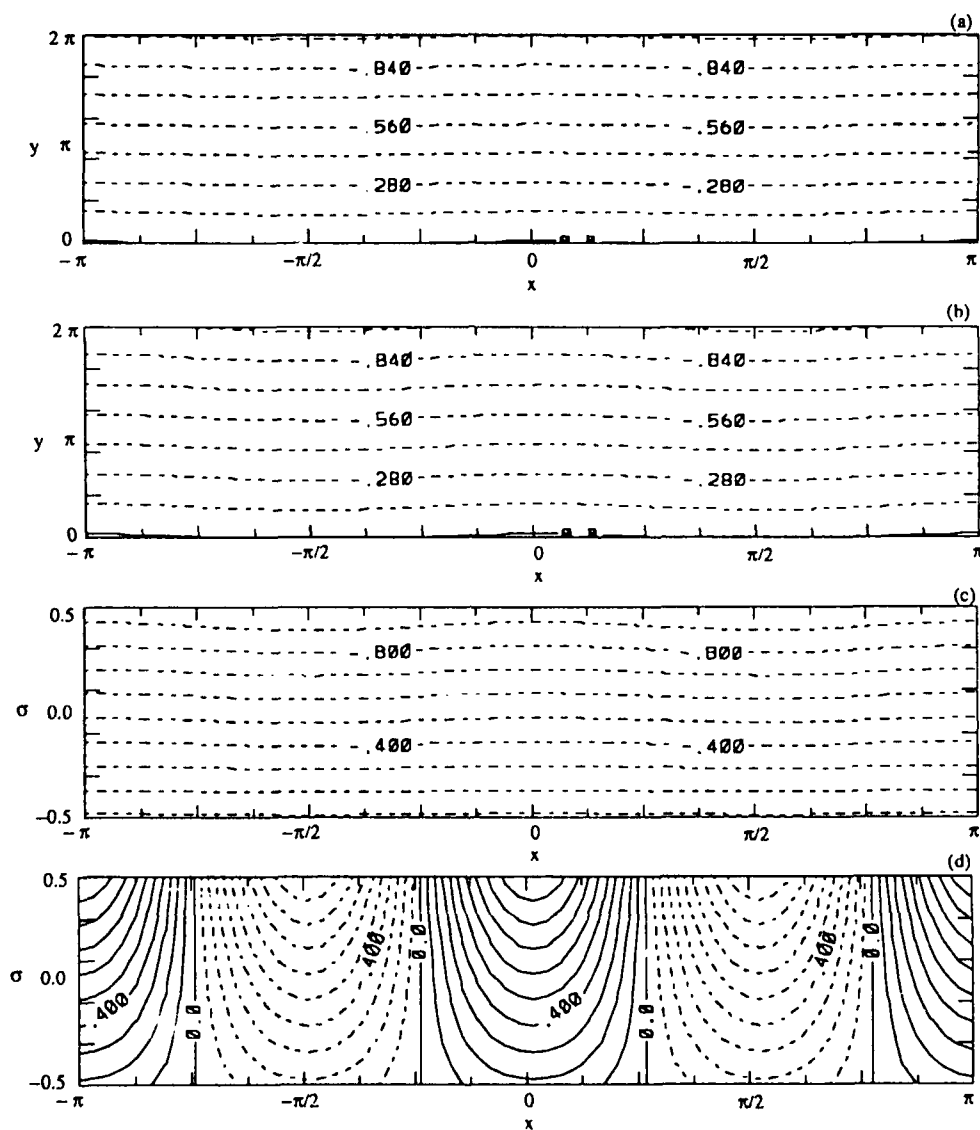


Figure 4.8 Basic state and perturbation streamfunction for very small mountain height, $h = 0.01$. (a) x-y cross section of basic state streamfunction at top and (b) bottom. (c) x- σ cross section of basic state streamfunction at mid-radius and (d) wavy part of basic state streamfunction. (e) x-y cross section of perturbation streamfunction at top and (b) bottom. (g) x- σ cross section perturbation at mid-radius. Topographic ridge at 0.0 and π rad. $U_0 = 0.1$, $\lambda = 1.0$, and $\varepsilon = 0.1$.

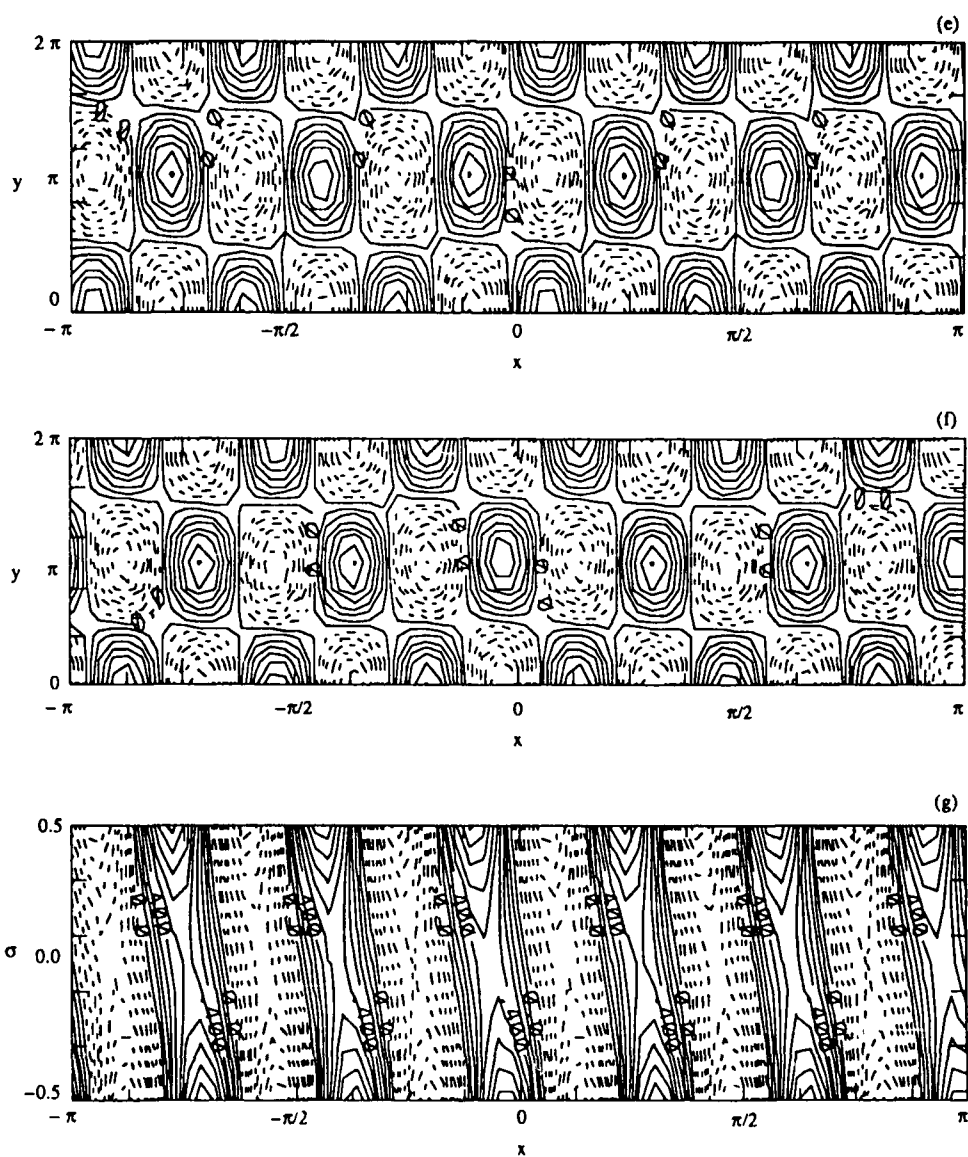


Figure 4.8 (continued)

in y . Figure 4.8 (g) is an x - σ cross section of the perturbation and is nearly the same as the perturbation for the Eady model shown in Figure 4.5 (b).

Next, we increased the mountain height to 0.1. Figure 3.3 (a) and (b) shows the basic state streamfunction is very wavy at the bottom and top. Figure 3.3 (c) show the x - σ cross section is also wavy with a high pressure ridge over the mountain ridge at 0 and π rad. Figure 4.9 (a) and (b) shows the x - y cross section of the perturbation streamfunction at the top and bottom. The perturbations follow the wavenumber two basic state. Thus, the basic state streamfunction acts as a guide or 'storm track' for the perturbation. Figure 4.9 (c) shows an x - σ cross section of the perturbation streamfunction. As predicted from the analytical model, there is one dominant wave number but the width of the highs and lows shows there is a superposition of several waves. Just downstream from the mountain ridge, the upper and lower modes are closer together and 'feel' each others presence and they have large amplitude at the top and bottom. Thus, we expect enhanced cyclogenesis in this region. Figure 2.5 (b) shows that downstream of the Rocky Mountains, enhanced cyclogenesis occurs.

Figure 4.10 shows the amplitudes of the spectral coefficients of (4.3.2) for the most unstable mode for the same parameters values considered in figure 4.9 as well as in Figure 4.4 for the analytical solution. Wavenumbers four, six, and eight have magnitudes about an order of magnitude larger than the other wavenumbers for this mode. These are also the most important wavenumbers from the analytical model. As in Figure 4.4, 4.10 shows the magnitudes of the coefficients at the lower boundary have the largest amplitudes.

We also investigated the effect that U_0 had on the basic state and perturbations. When U_0 is negative, the basic state is out of phase with the mountain. This is not observed in the atmosphere or the annulus and probably is not physically realizable. When U_0 is positive, the basic state is in phase with the mountain and shown Figure 3.3 (a) - (d).

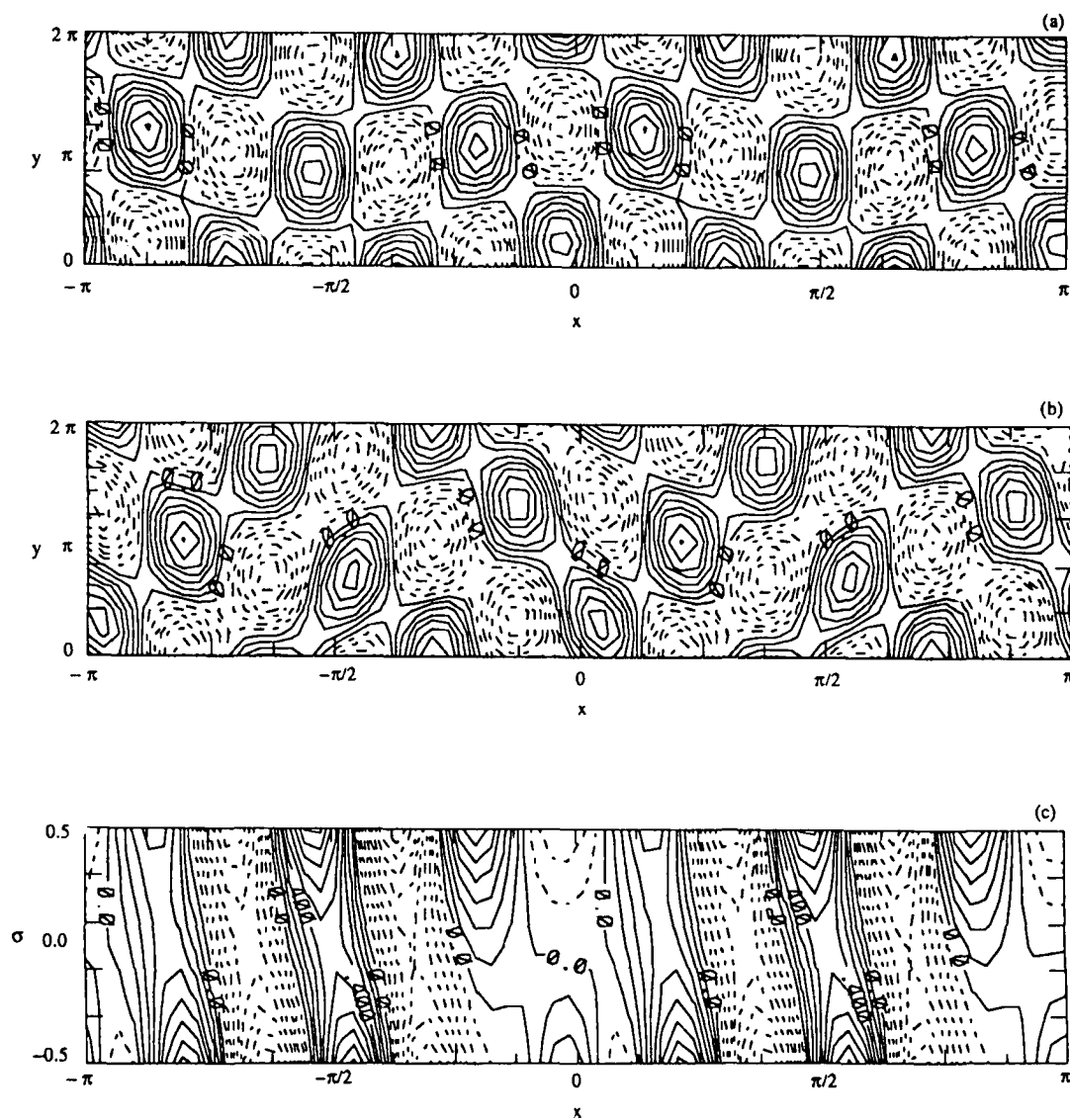


Figure 4.9 Perturbation streamfunction for a mountain height, $h = 0.1$. (a) x-y cross section at top and (b) bottom. (c) x- σ cross section at mid-radius. Topographic ridge at 0.0 and π rad. $S = 0.25$, $U_0 = 0.1$, $\epsilon = 0.1$, and $\lambda = 1.0$.

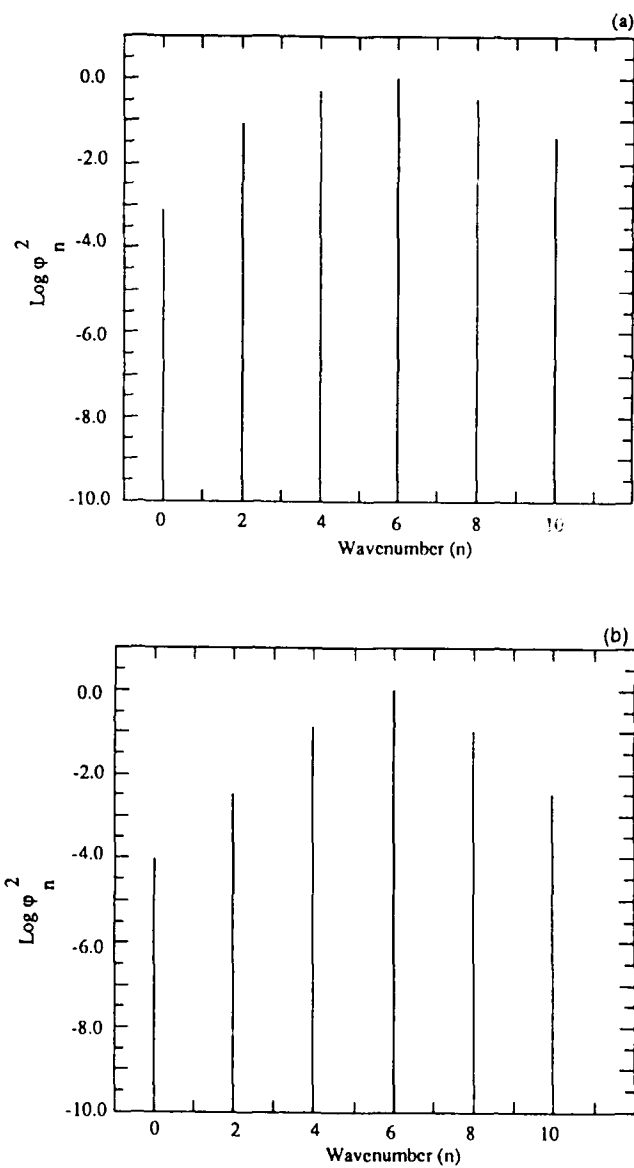


Figure 4.10 Magnitude of the coefficients of (4.3.2) as a function of wavenumber for (a) the lower and (b) the upper boundary. Here, $S = 0.25$, $U_0 = 0.1$, $\delta = 0.1$, $\varepsilon = 0.1$, and $\lambda = 1.0$.

When $U_0 = 0.0$, there is no x -dependence in the basic state but the perturbation can still interact with the mountain. Figure 4.11 (a) and (b) shows x - y cross sections at the top and bottom. As the perturbation flows over the mountain it moves to the north. This can be understood from the thermodynamic boundary condition, (4.2.11). As the zonal flow rises over the mountain slope, it cools adiabatically. The response in the fluid is an increased meridional flow which advects warmer fluid and the perturbations north. Figure 4.11 (c) shows the vertical structure of the perturbation. Buzzi (1987) showed the same type of phenomena occurs in their two-layer quasi-geostrophic model. Buzzi (1989) showed that as observed perturbations flow over the mountain, they move north and rotate anticyclonically as shown in Figure 2.6.

To investigate the time dependence in the continuous model, we plotted the x - z and x - y perturbation contours as a function of time. The plots shown in Figure 4.12 (a) - (d) are x - σ cross sections and (e) - (f) are x - y cross sections for non-dimensional times of approximately 0.5 days. $U_0 = 0.0$ so there is no wavy basic state. At each time step we normalized by the exponential growth rate. In Figure 4.12 (a) - (d), the x - σ cross sections show that as the perturbation rises up the mountain slope, its amplitude is decreased at the surface. As the perturbation flows down the mountain slope, the amplitude at the surface is enhanced. Just downstream from the mountain, instabilities at the top and bottom extend toward each other suggesting the possibility for enhanced growth. Figure 2.5 taken from observations shows this is a region of enhanced growth. Figure 4.12 (e) - (g) shows the x - y cross section as a function of time. As anticipated, the perturbation moves north as it flows over the mountain.

In Section 4.2, the analytical model showed that to leading order, the problem is the Eady model with a correction due to the mountain. Therefore, we should expect in this numerical model, that the fastest growing mode will be that predicted by the Eady model

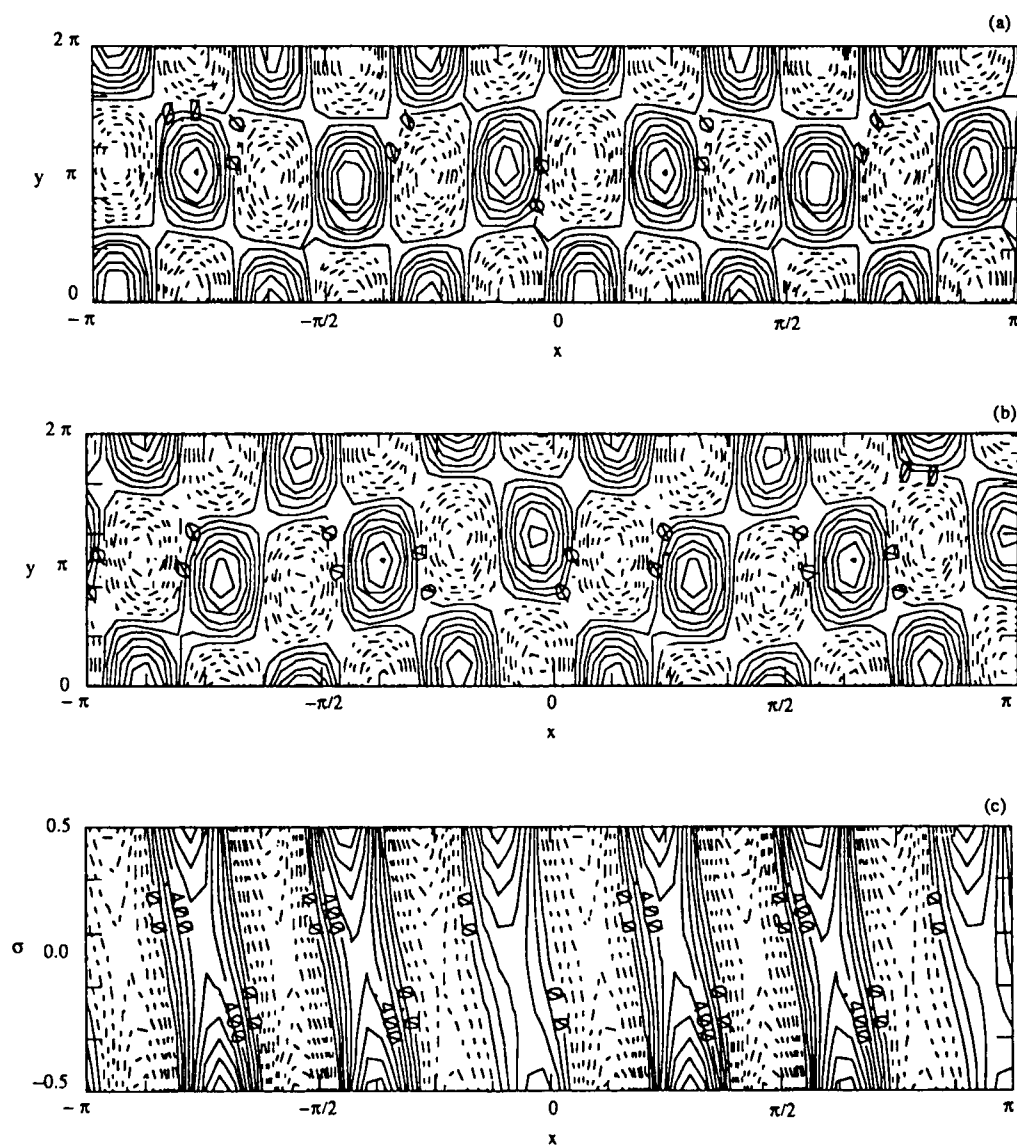


Figure 4.11 Perturbation streamfunction when the basic flow is zero so that there is no wavy basic state but the mountain height is $h = 0.1$. (a) x-y cross section at top and (b) bottom. (c) x- σ cross section at mid-radius. Topographic ridge at 0.0 and π rad. $S = 0.25$, $U_0 = 0.0$, $\epsilon = 0.1$, and $\lambda = 1.0$.

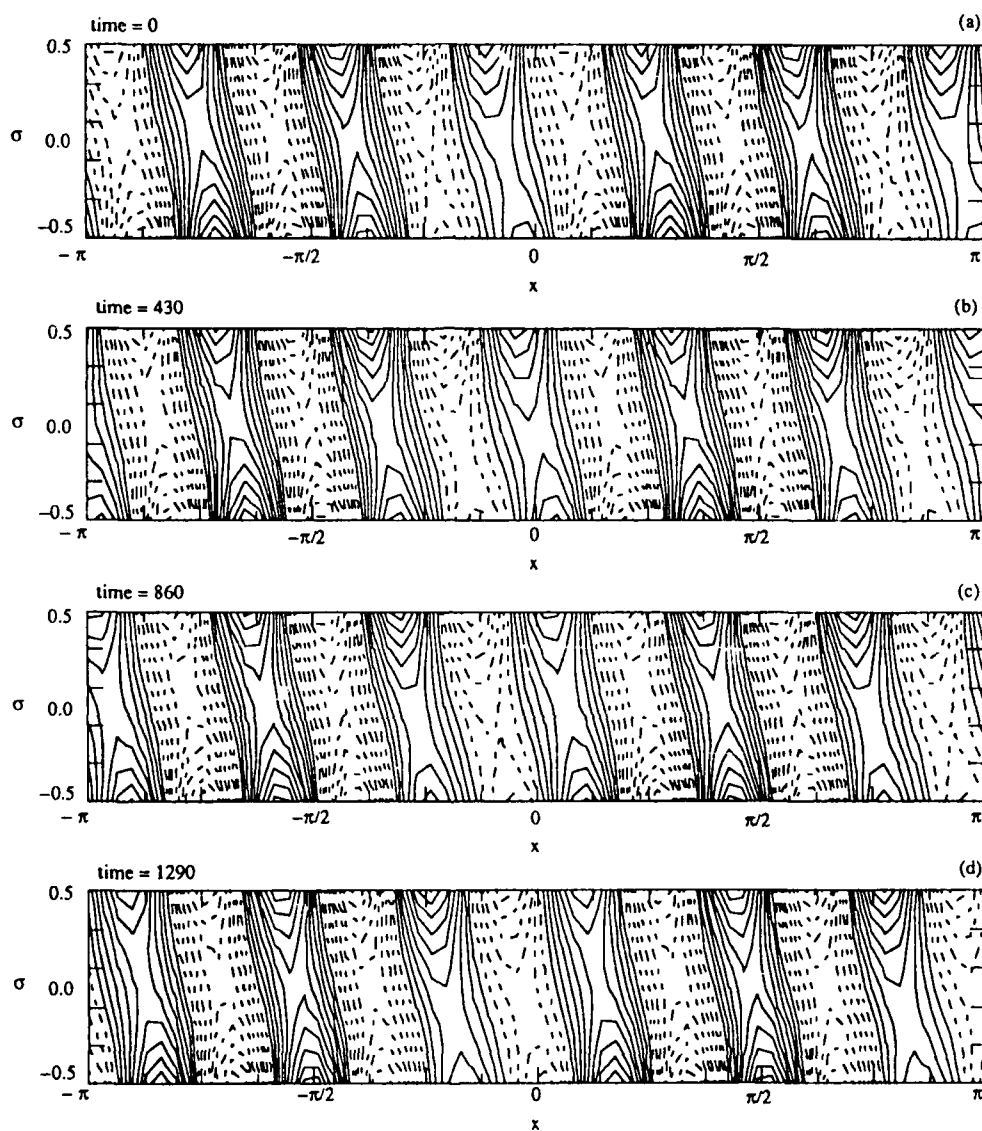


Figure 4.12 Perturbation streamfunction as a function of non-dimensional time with no wavy basic state. (a) - (d) x - σ cross sections and (e) - (f) x - y cross sections. Topographic ridge at 0.0 and π rad. $S = 0.25$, $U_0 = 0.0$, $\epsilon = 0.1$, and $\lambda = 1.0$.

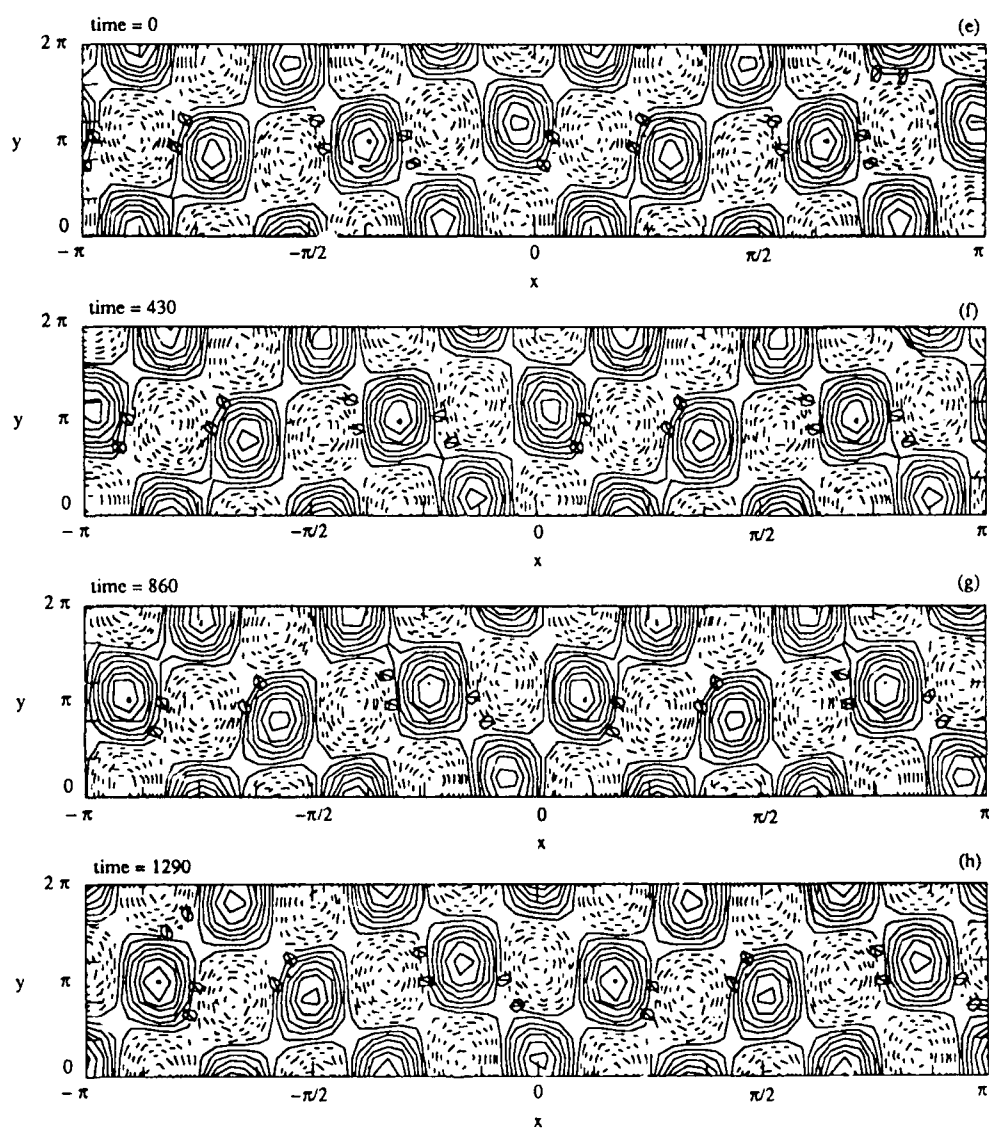


Figure 4.12 (continued)

and if $S = 0.25$, the wavenumber is six. The mode with the second largest growth could be found using Figure 4.1. and this mode matches the mode found in the numerical model. The frequency for every mode found in the numerical model matches that found with the Eady model. Therefore, the analytical model provides a way to understand the numerical results.

4.4 Topographic Instability

When we write the full set of equations in spectral form, we find that the zonal acceleration of the mean flow enters the equations when the meridional wavenumber is zero. When the meridional structure is zero, we derive a different set of spectral equations

$$\frac{\partial}{\partial t} \left(\frac{\partial \phi^+}{\partial \sigma} \right) + (U_0 + \lambda)(i2K) \frac{\partial \phi^+}{\partial \sigma} - (\lambda i2K) \phi^+ + i\nu K \Psi^+ u' \delta_{q,2} = 0, \quad (4.4.1)$$

and

$$\frac{\partial}{\partial t} \left(\frac{\partial \phi^-}{\partial \sigma} \right) + U_0(i2K) \frac{\partial \phi^-}{\partial \sigma} - (\lambda i2K) \phi^- + i\nu K(\Psi^- + 1) u' \delta_{q,2} = 0. \quad (4.4.2)$$

In (4.4.1) and (4.4.2), the last term represents the advection of the volumetrically averaged $u'(t)$ by the basic state and over the mountain slope at the lower boundary and δ represents the Kronecker delta. This term appears only when the perturbation has the same wavenumber as the basic state or mountain. Therefore, *these equations apply for zonal wavenumber two only*. For other perturbation wavenumbers, the last term is zero and the problem reduces to the Eady problem. By introducing a new variable $u'(t)$ into these equations, we will need one additional equation, the form-drag equation, to solve the problem. If we substitute the wavy basic state (4.3.1) and perturbation (4.3.2) into the form-drag equation, (3.7.4), after some algebra we obtain an expression

$$u'(t) = \frac{2K(\delta)}{\omega \varepsilon} \left[A_{20}^I \left(\cosh(\mu_{20}) - \frac{\sinh(\mu_{20})}{\mu_{20}} \right) - B_{20}^I \sinh(\mu_{20}) \right]. \quad (4.4.3)$$

A_{20}^I and B_{20}^I are the imaginary parts of complex coefficients. For the problem with no y-structure we have three complex equations and three unknowns.

Buzzi *et al.* (1984, hereafter BTS) also solved this problem with no y-structure using a continuous Eady model and wavy and zonal basic states. However in their model as they varied the wavenumber, the wavenumber of the basic state, mountain, and perturbation all changed. We cannot make a direct comparison of our work with the work of BTS since our basic state and mountain are always wavenumber two but we can compare when the perturbations is wavenumber two. Also, our model does not include friction.

To solve (4.4.1) and (4.4.2) we follow the same procedure outlined in Section 4.2. Here we only consider wavenumber two, the wavenumber of the topography and the basic state. When the form-drag is included, the system of equations is

$$\dot{B} + a_1 A + b_1 B + u_1 u' = 0 \quad (4.4.4)$$

$$\dot{A} + a_2 A + b_2 B + u_2 u' = 0 \quad (4.4.5)$$

$$\dot{u}' + a_3 A + b_3 B = 0 \quad (4.4.6)$$

The coefficients marked with italics are listed in Appendix B.

Figure 4.13 (a) shows contours of growth rate and (b) frequency as a function of stratification and U_0 . We find topographic instability for small values of stratification and for positive U_0 . Figure 4.14 (a) shows contours of growth rate and (b) frequency as a function of stratification and mountain height. Figure 4.14 (b) shows that as the mountain height increases, the region of topographic instability occurs for larger values of stratification.

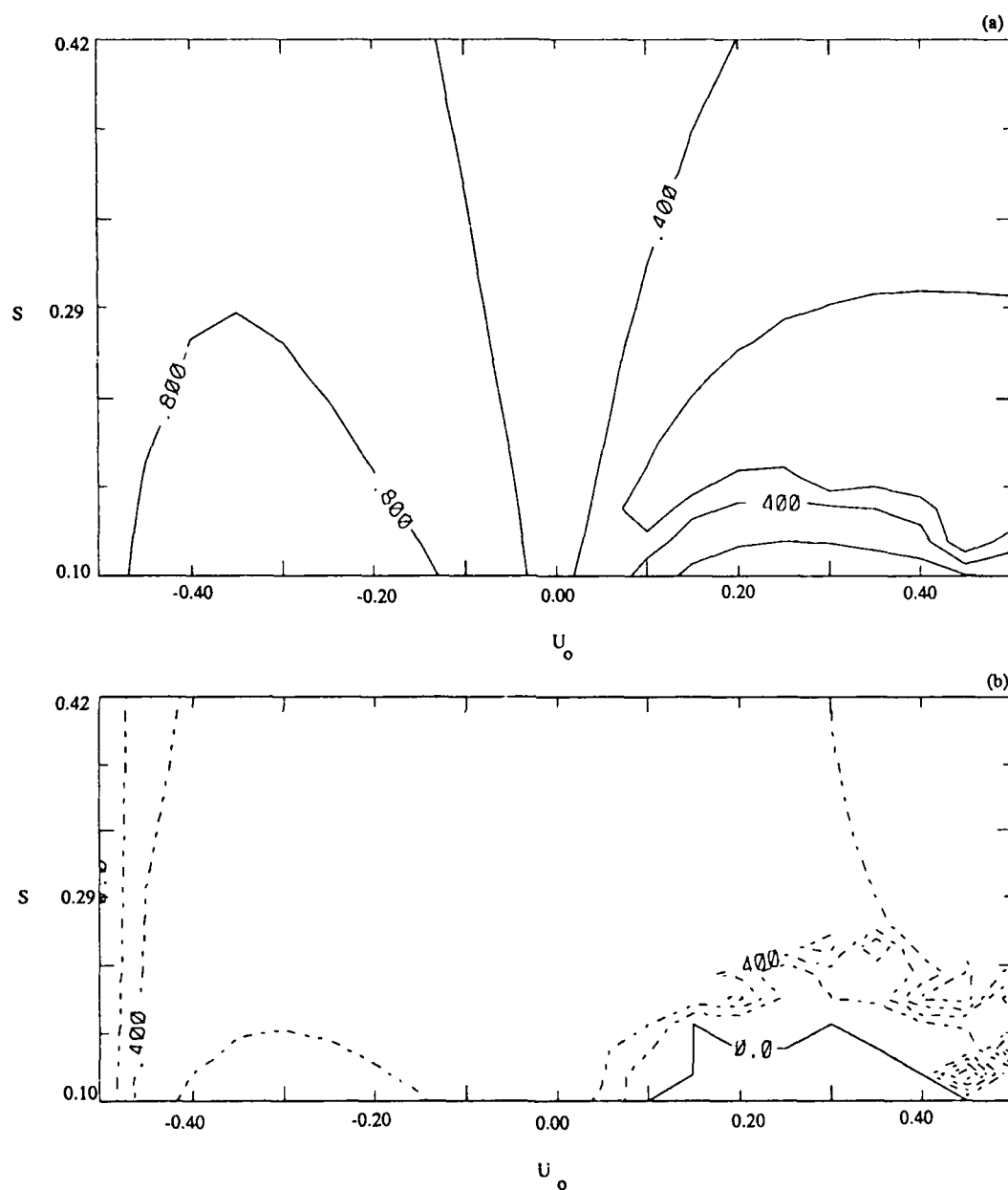


Figure 4.13 Contours of (a) growth rate and (b) frequency for the topographic instability problem as a function of S and U_0 . Region of zero frequency is in the lower right hand corner. $h = 0.1$, $\lambda = 1.0$ and $\epsilon = 0.1$.

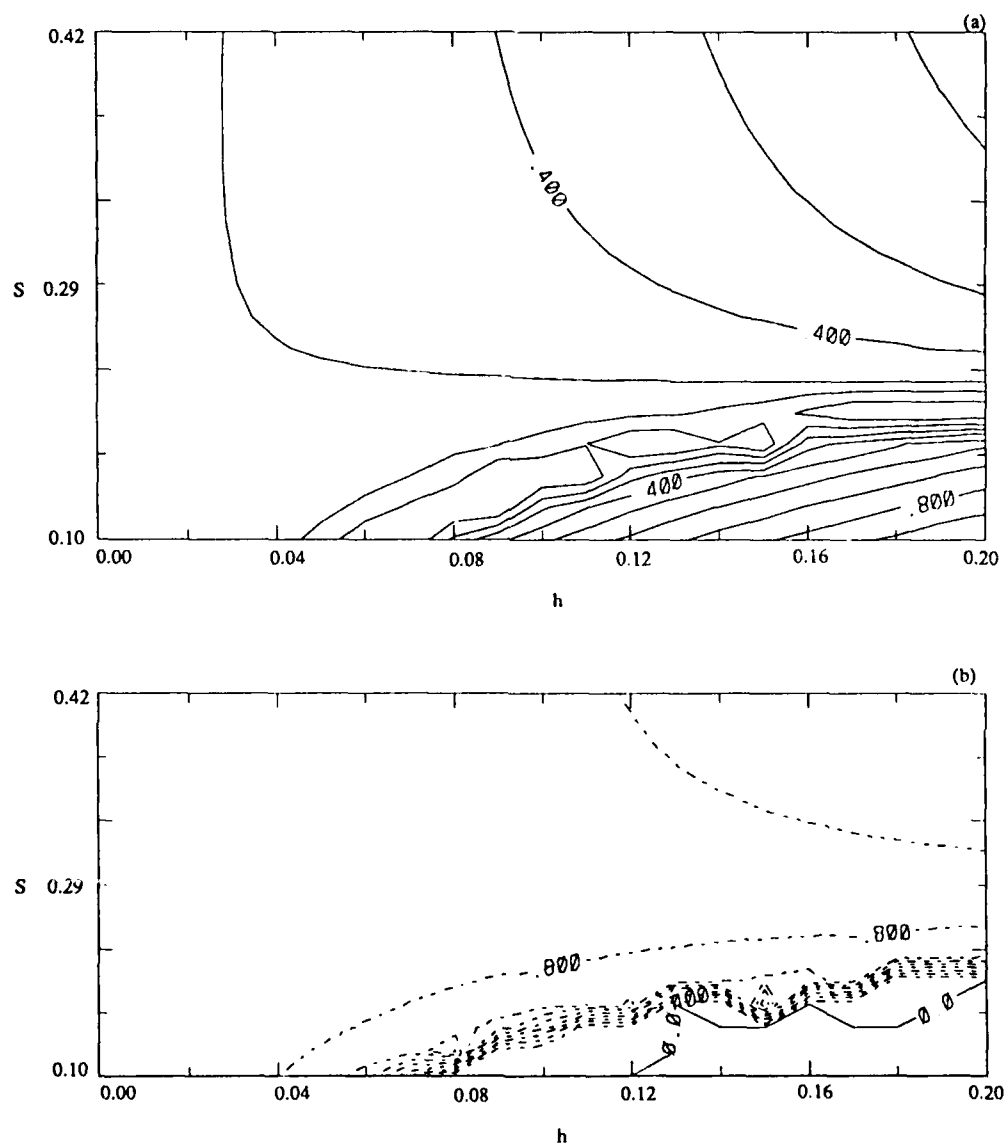


Figure 4.14 Contours of (a) growth rate and (b) frequency for the topographic instability problem as a function of S and h . Region of zero frequency is for low values of S . $U_0 = 0.1$, $\lambda = 1.0$ and $\epsilon = 0.1$.

CHAPTER 5

DISCUSSION AND CONCLUSIONS

In this thesis, we developed a mathematical model to describe baroclinic flow over topography on a wavy basic state. We chose a wavy basic state based on the observed, nearly stationary pattern in the atmosphere. We were more interested in understanding how baroclinic waves were modified by topography rather than topographic instability which at present appears not to be important in the primitive equation model of Revell and Hoskins (1984).

We transformed the five governing equations to sigma coordinates so that the lower boundary coincided with the lowest sigma level in the model. Based on scaling arguments, we derived the quasi-geostrophic potential vorticity equation and thermodynamic equations for the upper and lower boundaries in sigma coordinates. In sigma coordinates, the effect of topography appears in the thermodynamic equation at the lower boundary. The topography term is proportional to $v = S\delta/\epsilon$, or the mountain height, stratification and Rossby. We purposely chose a simple model with only the essential features required to describe the interaction of the flow with the mountain.

To solve the quasi-geostrophic potential vorticity equation and the thermodynamic equations on the boundaries, we linearized about a steady, wavy basic state with linear vertical shear which is an *exact* solution to the non-linear problem. The x-dependent part of the basic state was forced by topography and simulates the observed wavenumber two standing pattern in the atmosphere and the annulus. We have made the simplification that

both the basic state and the perturbation have zero potential vorticity in the interior of the fluid, in the spirit of the Eady model. Nevertheless, baroclinic instability is possible due to the potential vorticity sheets found on the horizontal boundaries.

We solved the linear instability problem using an analytical and a numerical technique. The analytical solution capitalized on the fact that all the terms in the equation involving the mountain or the wavy basic state are proportional to the parameter $\nu = (S\delta/\epsilon)$ which was taken to be small. We wrote the problem using an asymptotic expansion in that small parameter ν and found that to leading order, we recover the Eady model. This was no surprise since to $O(\nu^0)$, the basic state is rectilinear and identical to the Eady basic state. At the $O(\nu^1)$, we brought in the correction due to topography and wavy basic state. A very important result from the asymptotic analysis is the $O(\nu^1)$ problem provides us with a correction to the eigenfunction structure while the frequency correction is only found at $O(\nu^2)$, an order not yet considered. We selected the fastest growing mode with wavenumber n to correspond to the leading mode n of the Eady model. The correction to the leading order problem involved modes $n \pm 2$ due to the x -dependence introduced in the lower and upper boundary conditions by the topography and basic state which are wavenumber two. All of the modes $n, n \pm 2$ have the same frequency, ω_0 .

In the numerical technique, the quasi-geostrophic potential vorticity equation and thermodynamic boundary equations were transformed to spectral space. Since we chose the potential vorticity on the interior of the fluid equal to zero, the solution in the vertical involved hyperbolic functions. We chose the model to be periodic in x and y so that trigonometric functions were solutions in the horizontal. The transformation resulted in spectral equations that were coupled in the zonal direction with wavenumber two due to topography and wavy basic state. The equations were decoupled in the meridional direction. We separated the equations into a dynamical system of equations for the time

dependent spectral coefficients. Since the model is linear, we assumed an exponential time dependence and solved the system using an eigenanalysis. The analysis returns growth rates and frequencies for the various modes in the problem as well as the eigenvector to reconstruct the streamfunction for a given mode.

We compared the frequencies of this model with those of the analytical, Eady model. We showed the growth rate and frequency for the most unstable mode found in the numerical model as a function of stratification and mountain height. If the mountain height is zero, the frequencies are those of the Eady model. For small mountain heights and stratification, $v = S\delta/\epsilon$, is small and the analytical model and the numerical results are in good agreement. However, as the mountain height and stratification increase, the frequency predicted by the analytical model departs from the frequency found in the numerical calculation. One reason for the divergence is the analytical model was based on $v \ll O(1)$ and another is there were many more modes included in the numerical solution.

The growth rate was found to be sensitive to U_0 which is a parameterization of the momentum flux convergence into the midlatitudes. For $U_0 > -0.1$, the growth rate is nearly constant as U_0 increases and the frequency appears to increase linearly. As $U_0 \rightarrow -0.5$, the frequency becomes zero and the growth rates become enormous. We can understand the frequency going to zero from the Eady dispersion relation, (4.1.10). Since $\lambda/2 = 0.5$, the frequency approaches zero as U_0 approaches -0.5 . In Section 3.6, we show that the denominator of the basic state coefficients approaches zero as U_0 approaches -0.5 which causes the growth rates to become very large.

We also compared what happened in the instability problem when there was and was not a wavy basic state. When $U_0 = 0$, the wavy part of the basic state is zero and there is only linear vertical shear left in the basic state. We found that the perturbations tend to follow the basic state. Thus, the basic state acts as a 'storm track' for the disturbances.

The amplitude of the basic state depends on U_0 . If U_0 is very small or equal to zero then the basic state is nearly zonal. But the perturbations still move north over the mountain. However, if U_0 is strong, the basic state has large north-south excursions and the perturbations are carried farther north than they would have been without a wavy basic state. When U_0 is large, more of the basic flow is being forced to rise over the mountain. As it rises, it cools adiabatically and this results in an imbalance in the thermodynamic equation. To compensate for the imbalance, a southerly, meridional flow is established which advects warm air and the perturbations from the south. Observations from the atmosphere show that the baroclinic eddies propagate north as they flow over the mountain. Also, observations from the atmosphere show the storm tracks are strong on either side of the mountain but are at a minimum over the mountain. Part of the reason for this may be the amplitude of the basic current is highly dependent on U_0 .

Topographic instability occurs in this model when there is no y-structure and when the perturbation is wavenumber two, the wavenumber of the basic state and the mountain. It occurs due to the form-drag which couples the acceleration of the mean zonal flow with the topography. Revell and Hoskins (1984) questioned whether topographic instability exists in a purely baroclinic model. Källen (1982) and Buzzi *et al.* (1984) showed that a baroclinic model with constant zonal flow does have the mechanism for topographic instability to occur. In this baroclinic model, the constant flow U_0 is present and Figures 4.9 and 4.10 show the region in parameter space where it occurs. The instability occurs for physically unrealistic values of stratification. For values of stratification this small, the whole atmosphere would be unstable.

We chose to work with a continuous model in the vertical but could have worked with a two layer model as many modelers have done. The continuous model is better since it provides for better vertical resolution. Also, the conditions for instability may be different

in a continuous baroclinic than a two-layer baroclinic model.

The most serious weakness of this model is the use of the f -plane rather than the β -plane. The f -plane is physically unrealistic for the planetary scale waves we considered for the basic state. A significant improvement could be made if we solved the Charney (1947) problem rather than the Eady problem. The Charney model would allow us still to use a continuous model in the vertical but on a β -plane; analytical solutions of this problem probably would involve prohibitive amounts of algebra since the wavy basic state will now possess potential vorticity.

If the β effect and friction were included in the basic state calculation, the phase of the basic state could be adjusted with respect to the mountain ridge rather than the high pressure being coincident with the mountain ridge. If the β effect and friction were included in the perturbation problem, there could be a long wave cutoff due to the β effect and a region of stability added due to friction.

A still more realistic basic state would have horizontal as well as vertical shear but this would make an analytical solution more difficult. The horizontal shear would act as a guide for the instabilities much as the basic state does in this model. However, the horizontal shear eliminates the need for periodicity in y . Side wall boundary conditions would confine the north-south amplitude of the wave and channel the flow instabilities. This would give something more like observed in the annulus but may not represent the atmosphere since there are no sidewalls in the atmosphere to act as wave guides.

The linear model we used allows for zonal perturbation wave interactions of plus or minus two due to the topography and the basic state. Also, the linear model shows there is an acceleration of the zonal mean flow due to the form-drag mechanism. However, if we included non-linear interactions we could consider wave-zonal mean flow interactions for all wavenumbers. Non-linear interactions could help to account for the actual observed

patterns in the atmosphere that cannot be explained by linear theory.

APPENDIX A

SCALING OF CURVATURE TERMS AND THE BETA EFFECT

A.1 Curvature Terms

In this appendix, we want to show the relative magnitude of the curvature terms and the beta-effect to other terms in the momentum equations. Pedlosky (1987) gives the non-dimensional form of the x-component of the momentum equation in spherical coordinates as

$$\varepsilon \left\{ \frac{du}{dt} + \frac{L}{r_*} [\delta u w - u v \tan(\theta)] \right\} - v \frac{\sin(\theta)}{\sin(\theta_0)} + \delta w \frac{\cos(\theta)}{\cos(\theta_0)} = - \frac{\cos(\theta_0)}{\cos(\theta)} \frac{r_0}{r_*} \frac{\partial p}{\partial x} \left(\frac{1}{1 + \varepsilon \rho F} \right) \quad (A.1)$$

where

$$\frac{d}{dt} = \frac{\partial}{\partial t} + u \frac{\cos(\theta_0)}{\cos(\theta)} \frac{r_0}{r_*} \frac{\partial}{\partial x} + v \frac{r_0}{r_*} \frac{\partial}{\partial y} + w \frac{\partial}{\partial z},$$

$$\delta = \frac{D}{L},$$

$$F = \frac{(f_0 L)^2}{gD},$$

$$\theta = \text{latitude},$$

$$\theta_0 = \text{mid-latitude reference},$$

and

$$r_0 = \text{earth's radius}.$$

There are no approximations to the momentum equation. The equations are scaled so that the relative magnitude of each term may be measured by the term multiplying it. The first two terms on the left hand side of (A.1) are the advection and curvature terms. Each of these terms is scaled by the Rossby number. If we decide to keep terms of the $O(\epsilon)$, we must decide on the relative magnitude of the advection compared to curvature. This is measured by L/r_* .

The circumference of the Earth at a given latitude is $(2\pi r_* \tan(\theta))$. If we choose mid-latitude to be 45°N , the length of the Earth is $2\pi r_*$. We are considering wavenumber two. Therefore, the length of one wave is πr_* . The length scale for this wave is $r_*/2$. Therefore, a measure of the magnitude of curvature compared to advection is

$$\frac{L}{r_*} = .5$$

Thus, the curvature term is half the magnitude of the advective term. As a first approximation, we can neglect this term.

For the annulus, Bird, Stewart, and Lightfoot (1960) give the x-component of the horizontal momentum equation in cylindrical coordinates and non-dimensional form as

$$\epsilon \left(\frac{du}{dt} + \frac{L}{R} uv \right) + v + \frac{1}{\rho} \frac{\partial p}{\partial x} = 0 \quad (\text{A.2})$$

where R is the radius of the annulus. Again, if we are to include terms on the $O(\epsilon)$, then we need to compare the magnitude of the advective terms to the curvature terms. In Section 4.3 we find the circumference of the annulus at mid-radius is $\pi(a + b)$. The length of one mountain is half the length of the channel. Thus, $L = (a + b)/4 = 5.55 \text{ cm}$ and the radius of the channel is $(b + a)/2$. Thus the measure of the magnitude of curvature compared to advective terms is

$$\frac{L}{R} = \frac{(a + b)}{4(a + b)/2} = .5$$

Therefore, to a first approximation we can neglect the curvature term over the advection term.

A.2 Beta Effect

In the atmosphere, the depth of the fluid is small compared to the horizontal length scale so that the normal component of the Earth's vorticity is dynamically significant. Also, the north-south scale of the motion will be considered small so the Earth can be considered flat. The variation of the coriolis parameter with latitude can be linearized about a mean latitude so that f may be written as

$$f = f_0 + \beta_0 y . \quad (\text{A.3})$$

This is the beta - plane approximation. In our model we chose to use an f - plane which fixes the rotational effect of the Earth as constant. A check of the relative magnitudes of the terms in (A.3) gives

$$\frac{\beta_0 y}{f_0} = \frac{\frac{2\Omega \cos(\theta_0) L}{r_0}}{2\Omega \sin(\theta_0)} = \frac{L}{r_0} \tan(\theta_0) . \quad (\text{A.4})$$

If $\theta_0 = 45^\circ \text{N}$, $L/r_0 = .5$ for the atmosphere. In our model, we included terms on the $O(\epsilon)$.

For planetary waves, an estimate of the Rossby number is given by

$$\frac{2U}{r*f} = \frac{2 * 10}{(6.3 \times 10^6) * 10^{-4}} = 0.03.$$

In the annulus experiments we want to simulate, the bottom is not radially dependent so there is no beta-effect. However, there is a simulated beta-effect since the upper surface of the fluid slopes. The beta-effect can be estimated by making a balance of forces on a fluid

parcel on the sloping upper surface where

$$\beta = \frac{f}{D} \frac{\partial h}{\partial R} = \frac{2\Omega^2 R}{gD} . \quad (\text{A.5})$$

The magnitude of this term is less than $O(\epsilon)$ and is neglected.

APPENDIX B

COEFFICIENTS FOR THE NUMERICAL SOLUTION AND

TOPOGRAPHIC INSTABILITY PROBLEM

B.1 Numerical Solution

Coefficients for (4.3.9) are as follows:

$$as1 = \{ \mu_{q-2,r} A_B \cosh(\mu_{20}) - [\mu_{20} A_B \sinh(\mu_{20}) - .5] \coth(\mu_{q-2,r}) \} \frac{\sinh(\mu_{q-2,r})}{\sinh(\mu_{q,r})} \frac{K/r}{\mu_{q,r}},$$

$$as2 = \{ - \mu_{q+2,r} A_B \cosh(\mu_{20}) + [\mu_{20} A_B \sinh(\mu_{20}) - .5] \coth(\mu_{q+2,r}) \} \frac{\sinh(\mu_{q+2,r})}{\sinh(\mu_{q,r})} \frac{K/r}{\mu_{q,r}},$$

$$bs1 = \{ \mu_{q-2,r} B_B \sinh(\mu_{20}) \coth(\mu_{q-2,r}) - [\mu_{20} B_B \cosh(\mu_{20}) + .5] \} \frac{\sinh(\mu_{q-2,r})}{\sinh(\mu_{q,r})} \frac{K/r}{\mu_{q,r}},$$

$$bs2 = \{ - \mu_{q+2,r} B_B \sinh(\mu_{20}) \coth(\mu_{q+2,r}) + [\mu_{20} B_B \cosh(\mu_{20}) + .5] \} \frac{\sinh(\mu_{q+2,r})}{\sinh(\mu_{q,r})} \frac{K/r}{\mu_{q,r}},$$

$$as3 = \{ \mu_{q-2,r} B_B \sinh(\mu_{20}) \tanh(\mu_{q-2,r}) - [\mu_{20} B_B \cosh(\mu_{20}) + .5] \} \frac{\cosh(\mu_{q-2,r})}{\cosh(\mu_{q,r})} \frac{K/r}{\mu_{q,r}},$$

$$as4 = \{ - \mu_{q+2,r} B_B \sinh(\mu_{20}) \tanh(\mu_{q+2,r}) + [\mu_{20} B_B \cosh(\mu_{20}) + .5] \} \frac{\cosh(\mu_{q+2,r})}{\cosh(\mu_{q,r})} \frac{K/r}{\mu_{q,r}},$$

$$bs3 = \{ \mu_{q-2,r} A_B \cosh(\mu_{20}) - [\mu_{20} A_B \sinh(\mu_{20}) - .5] \tanh(\mu_{q-2,r}) \} \frac{\cosh(\mu_{q-2,r})}{\cosh(\mu_{q,r})} \frac{K/r}{\mu_{q,r}},$$

$$bs4 = \{ - \mu_{q+2,r} A_B \cosh(\mu_{20}) + [\mu_{20} A_B \sinh(\mu_{20}) - .5] \tanh(\mu_{q+2,r}) \} \frac{\cosh(\mu_{q+2,r})}{\cosh(\mu_{q,r})} \frac{K/r}{\mu_{q,r}},$$

$$ac1 = -as1,$$

$$ac2 = -as2,$$

$$bc1 = -bs1,$$

$$bc2 = -bs2,$$

$$ac3 = -as3,$$

$$ac4 = -as4,$$

$$bc3 = -bs3,$$

$$bc4 = -bs4,$$

$$as6 = ac6 = \frac{\lambda K q}{2} \left(\tanh(\mu_{qr}) - \frac{1}{\mu_{qr}} \right),$$

$$bs5 = bc5 = \frac{\lambda K q}{2} \left(\coth(\mu_{qr}) - \frac{1}{\mu_{qr}} \right),$$

and

$$as5 = ac5 = bs6 = bc6 = Kq \left(U_0 + \frac{\lambda}{2} \right).$$

B.2 Coefficients For Topographic Instability

Coefficients for (4.4.4) - (4.4.6) are as follows:

$$a1 = \lambda K \left(\tanh(\mu_{20}) - \frac{1}{\mu_{20}} \right),$$

$$b2 = \lambda K \left(\coth(\mu_{20}) - \frac{1}{\mu_{20}} \right),$$

$$b1 = a2 = 2K \left(U_0 + \frac{\lambda}{2} \right),$$

$$u1 = K \left(\frac{v}{4\mu_{20}} \cosh(\mu_{20}) + \frac{AB}{2\mu_{20}} \right),$$

$$u_2 = K \left(-\frac{v}{4\mu_{20}} \sinh(\mu_{20}) + \frac{B_B}{2\mu_{20}} \right),$$

$$a_3 = -2K \frac{\delta}{\epsilon} \left(\cosh(\mu_{20}) - \frac{\sinh(\mu_{20})}{\mu_{20}} \right),$$

$$b_3 = 2K \frac{\delta}{\epsilon} \sinh(\mu_{20}),$$

and

$$u_3 = 0.$$

REFERENCES

- Bird, R. B., W. E. Stewart, and E. N. Lightfoot, 1960: *Transport Phenomena*. John Wiley & Sons, 780 pp.
- Blackmon, M. L., J. M. Wallace, N-C. Lau, and S. L. Mullen, 1977: An observational study of the northern hemisphere wintertime circulation. *J. Atmos. Sci.*, **34**, 1040-1053.
- Blackmon, M. L., 1976: A climatological spectral study of the 500 mb geopotential height of the northern hemisphere. *J. Atmos. Sci.*, **33**, 1607-1623.
- Blackmon, M. L., Y.-H. Lee, J. M. Wallace, 1984: Horizontal structure of the 500 mb height fluctuations with long, intermediate, and short time scales, *J. Atmos. Sci.*, **41**, 961-979.
- Bretherton, F. P., 1966: Critical layer instability in baroclinic flow. *Quart. J. Roy. Meteor. Soc.*, **92**, 325-334.
- Buzzi, A., and A. Speranza, 1986: A theory of deep cyclogenesis in the lee of the alps. Part II: Effects of finite topographic slope and height. *J. Atmos. Sci.*, **43**, 2826-2837.
- Buzzi, A., A. Speranza, S. Tibaldi, and E. Tosi, 1987: A unified theory of orographic influences upon cyclogenesis. *Meteor. Atmos. Phys.*, **36**, 2826-2837.
- Buzzi, A., and E. Tosi, 1989: Statistical behavior of transient eddies near mountains and implications for theories of lee cyclogenesis. *J. Atmos. Sci.*, **46**, 1233-1249.
- Buzzi, A. A. Trevisan, and A. Speranza, 1984: Instabilities of a baroclinic flow related to topographic forcing. *J. Atmos. Sci.*, **41**, 637-650.
- Cessi, P., and A. Speranza, 1985: Orographic instability of nonsymmetric baroclinic flows and nonpropagating planetary waves. *J. Atmos. Sci.*, **42**, 2585-2596.
- Charney, J. G., 1947: The dynamics of long waves in a baroclinic westerly current. *J. Meteor.*, **4**, 1040-1053.
- Charney, J. G., 1948: On the scale of atmospheric motions. *Geof. Publ.*, **17**, 3-17.
- Charney, J. G., and J. G. DeVore, 1979: Multiple flow equilibria in the atmosphere and blocking. *J. Atmos. Sci.*, **36**, 1205-1216.

- Charney, J. G., and D. M. Straus, 1980: Form-drag, multiple equilibria and propagating planetary waves in baroclinic, orographically forced, planetary wave systems. *J. Atmos. Sci.*, **37**, 1157-1176.
- Charney, J. G., and M. Stern, 1962: On the stability of internal baroclinic jets in a rotating atmosphere. *J. Atmos. Sci.*, **19**, 159-172.
- Derome, J., 1984: On quasi-geostrophic, finite-amplitude disturbances forced by topography and diabatic heating. *Tellus*, **36**, 313-319.
- De Szoeke, R. A., 1983: Baroclinic instability over wavy topography. *J. Fluid Mech.*, **130**, 279-298.
- Dutton, J. A., 1976: *The Ceaseless Wind: Introduction to the theory of atmospheric motion*. McGraw Hill, 579 pp.
- Eady, E. T., 1949: Long waves and cyclone waves. *Tellus*, **1**, 33-52.
- Grose, W. L., and B. J. Hoskins, 1979: On the influence of orography on large-scale atmospheric flow. *J. Atmos. Sci.*, **36**, 223-234.
- Grotjahn, R., 1984: Baroclinic instability in a long wave environment. Part I: Review, *Quart. J. Roy. Meteor. Soc.*, **110**, 663-668.
- Held, I. M., 1983: Stationary and quasi-stationary eddies in the extratropical troposphere: Theory. *Large Scale Dynamical Processes in the Atmosphere*, B. J. Hoskins and R. P. Pearce, Eds., Academic Press, 397 pp.
- Held, I. M., and M. Ting, 1990: Orographic versus thermal forcing of stationary waves: The importance of the mean low-level wind. *J. Atmos. Sci.*, **47**, 495-500.
- Hsu, H.-H., 1987: Propagation of low-level circulation features in the vicinity of mountain ranges. *Mon. wea. Rev.*, **115**, 1864-1892.
- Källén, E., 1983: A note on orographically induced instabilities in two-layer models. *J. Atmos. Sci.*, **40**, 500-505.
- Lau N.-C., 1979: The structure and energetics of transient disturbances in the Northern Hemisphere wintertime circulation. *J. Atmos. Sci.*, **36**, 982-995.
- Lau N.-C., 1979: The observed structure of tropospheric waves and the local balances of vorticity and heat, *J. Atmos. Sci.*, **36**, 996-1016.
- Li, G., R. Kung, and R. L. Pfeffer, 1986: An experimental study of baroclinic flows with and without two-wave bottom topography. *J. Atmos. Sci.*, **43**, 2585-2599.
- Malguzzi, P., A. Trevisan, and S. Speranza, 1987: Effects of finite height topography on nongeostrophic baroclinic instability: Implications to theories of lee cyclogenesis. *J. Atmos. Sci.*, **44**, 1475-1482.

- Niehaus, M., 1980: Instability of non-zonal baroclinic flows. *J. Atmos. Sci.*, **37**, 1447-1463.
- Pedlosky, J., 1981: Resonant topographic waves in barotropic and baroclinic flows. *J. Atmos. Sci.*, **38**, 2626-2641.
- Pedlosky, J., 1987: *Geophysical Fluid Dynamics*. Springer-Verlag, 710 pp.
- Pfeffer, R. L., R. Kung, and G. Li, 1989: Topographically forced waves in a thermally driven rotating annulus of fluid - experiment and linear theory. *J. Atmos. Sci.*, **46**, 2331-2342.
- Phillips, N. A., 1963: Geostrophic motion. *Rev. Geo.*, **1**, 123-176
- Pielke, R. A., 1984: *Mesoscale Meteorological Modeling*. Academic Press, 612 pp.
- Reinhold, B., 1990: Orographic modulation of baroclinic instability. *J. Atmos. Sci.*, **47**, 1697-1713.
- Revell, M., and B. J. Hoskins, 1984: Orographically induced Rossby wave instabilities. *J. Atmos. Sci.*, **41**, 51-67.
- Speranza, A., A. Buzzi, A. Trevisan, and P. Malguzzi, 1985: A theory of deep cyclogenesis in the lee of the Alps. Part I: Modifications of baroclinic instability by localized topography. *J. Atmos. Sci.*, **42**, 1521-1535.
- Tibaldi, S., A. Buzzi, and P. Malguzzi, 1980: Orographically induced cyclogenesis: Analysis of numerical experiments. *Mon. Wea. Rev.*, **108**, 1302-1314.
- Tosi, E., M. Fantini, and A. Trevisan, 1983: Numerical experiments on orographic cyclogenesis: Relationship between the development of the lee cyclone and the basic flow characteristics. *Mon. Wea. Rev.*, **111**, 799-814.
- Wallace, J. M., and M. L. Blackmon, 1983: Observations of low-frequency atmospheric variability. *Large-Scale Dynamical Processes in the Atmosphere*, B. J. Hoskins and R. P. Pearce, Eds., Academic Press, 397 pp.
- Wallace, J. M., 1983: The climatological mean stationary waves: observational evidence. *Large-Scale Dynamical Processes in the Atmosphere*, B. J. Hoskins and R. P. Pearce, Eds., Academic Press, 397 pp.
- Yoden, S., and H. Mukougawa, 1983: Instabilities of a baroclinic zonal flow in the presence of surface topography. *J. Met. Soc. Jap.*, **61**, 789-804.

BIOGRAPHICAL SKETCH

Thomas F. Simeone was born in [REDACTED] graduated from Franklin High School, Franklin Massachusetts, in June 1979. He received his undergraduate degree in June 1984 from the University of Massachusetts at Amherst where he majored in Chemical Engineering and minored in Chemistry.

In 1985, he entered the United States Air Force and was commissioned as a Second Lieutenant. His first assignment was to Texas A & M University for one year of meteorological training. Then, he was assigned as the Wing Weather Officer at Bitburg AB, W. Germany from January 1987 to December 1988. In January 1989, he was assigned to the Florida State University to earn his Master's degree in meteorology.